Doctoral Dissertation

博士論文

Detection and Quantification of Pre-P Gravity Signals from the 2011 Tohoku-Oki Earthquake
–Proposal of Pre-P Gravity Seismology through Observation and Theoretical Modeling–

（2011年東北沖地震からのP波前重力信号の検出と定量化
–観測および理論モデリング研究を通したP波前重力地震学の提案–）

A Dissertation Submitted for the Degree of Doctor of Philosophy
December 2020

令和2年12月博士（理学）申請

Department of Earth and Planetary Science, Graduate School of Science, The University of Tokyo

東京大学大学院理学系研究科地球惑星科学専攻

Masaya Kimura

木村　将也

Abstract

Dynamic earthquake rupture causes a mass redistribution around the fault, and the emitted propagating seismic waves are accompanied by bulk density perturbations. Both processes are thought to cause a transient gravity change prior to the arrival of P-waves. The first theoretical model showed an expression of this pre-P gravity signal, providing the first target for signal detection. Then, the pre-P signal from the 2011 Tohoku-Oki earthquake was reported, but the statistical significance of the signal was not enough to be considered as a discovery of a new physical phenomenon. The second detection was reported as an agreement between observed waveforms and synthetics calculated using an improved model. However, the signal significance was not discussed, and the employed signal processing method included an acausal process, which may cause artifacts in the original records. In this thesis, we first aimed to identify the pre-P gravity signal with a sufficient statistical significance. Using an artifact-free signal processing method, we detected the signal from the 2011 event with a 7σ significance. We then examined the previous acausal signal processing method and showed that the resultant artifacts were sufficiently small not to deny the second detection report. These two studies of ours confirmed the existence of pre-P gravity signals and established a basis for the quantitative comparison between observation and theoretical modeling. In the third study, we proceeded to the use of the pre-P gravity signal to estimate the source parameters of the 2011 event. We conducted a waveform inversion analysis for the identified three-component pre-P signal from the event, combined with synthetics calculated using the simulation approach which solves the fully coupled elasto-gravity

equations for a realistic Earth structure. The pre-P gravity signal gave a constraint on the dip angle of the source, which is not well determined from long-period seismic waves. Through our studies, the research field that deals with pre-P gravity signals has progressed from the phase of discussing the signal existence to the next stage where quantitative comparison between observation and theoretical modeling provides a new seismological implication. Finally, we proposed that the usage of the three-component pre-P gravity signal waveforms was essential for providing the new constraint on the source parameters beyond the limitation of the seismic wave observations.

Contents

1. General introduction 6

1.1 Theoretical modeling for pre-P gravity signal 6

1.1.1 Model 1 considering gravity change $\delta \boldsymbol{g}$ induced by density perturbation $\delta\rho$ 6

1.1.2 Model 2 considering acceleration $\ddot{\boldsymbol{u}}^{\delta g}$ induced by $\delta \boldsymbol{g}$ 11

1.1.3 Model 3 considering fully coupled elasto-gravity equations in a spherical Earth 13

1.2 Search for pre-P gravity signals from the 2011 Mw 9.1 Tohoku-Oki earthquake 17

1.3 Applicability for early warnings and scientific significance of the pre-P gravity signal 18

1.4 Purpose of this study 19

2. Pre-P gravity signal identified in dense array data in Japan 22

2.1 Introduction 22

2.2 Data 22

2.3 Methods 27

2.3.1 Detection criterion 27

2.3.2 Waveform simulation for stacking 27

2.4 Results 27

2.4.1 Superconducting gravimeters 27

2.4.2 F-net broadband seismometers 30

2.4.3 Hi-net tiltmeters 36

2.5 Discussion 36

2.5.1 Difference from previous SG study 36

2.5.2 Significance of our stacked trace on theoretical modeling 37

2.5.3 Possible reasons for no finding with tiltmeters 37

2.5.4 Toward future detection of pre-P gravity signals using a gravity-gradient sensor 38

2.6 Conclusions 41

3. Evaluation of artifacts caused by acausal signal processing employed by Vallée et al. (2017) 42

3.1 Summary 42

3.2 Introduction 43

3.3 Verification of the signal processing procedure employed by Vallée et al. (2017) 45

3.4 Discussion 61

3.4.1 Waveform distortion due to filtering 61

3.4.2 Possible artifacts due to extremely-large-amplitude seismic waves 62

3.5 Conclusions 65

4. Determination of source parameters of the 2011 Tohoku-Oki earthquake from three-component pre-P gravity signals recorded by dense arrays in Japan 66

4.1 Summary 66

4.2 Introduction 66

4.3 Data 67

4.4 Methods 71

4.4.1 Waveform simulation 71

4.4.2 Point source correction 72

4.4.3 Waveform stacking 74

4.4.4 Inversion method 74

4.5 Results 76

4.5.1 Detection of the horizontal component of the pre-P gravity signal 76

4.5.2 Waveform inversion 79

4.6 Discussion 82

4.6.1 Detection of the horizontal component of the pre-P gravity signal 82

4.6.2 Waveform inversion 83

4.7 Conclusions 86

5. General conclusions 87

Appendix A 88

Appendix B 90

Appendix C 91

Appendix D 92

Acknowledgements 95

Data availability 96

References 97

Supplement 104

1. General introduction

Earthquake faulting causes a mass redistribution in the vicinity of the fault, which causes a post-earthquake static gravity change. This gravity change has been observed for several earthquakes and compared with model predictions (Imanishi et al. 2004; Matsuo and Heki 2011; Wang et al. 2012a, b). During the dynamic rupture, bulk density perturbations are temporarily caused by the propagating compressional waves. Both processes produce a transient gravity change, which starts before the P-wave arrival (Harms et al. 2015). A search for such pre-P gravity change in superconducting gravimeter records has started two decades ago (Mansinha and Hayes 2001; Hayes et al. 2004). However, there was not a model prediction for the pre-P gravity change, and they could not separate the real signal from the artifacts of their spline curve fitting.

1.1 Theoretical modeling for pre-P gravity signal

1.1.1 Model 1 considering gravity change δg induced by density perturbation $\delta\rho$

Harms et al. (2015) developed a first quantitative model for the pre-P gravity change and set the observation targets. They considered a double couple (DC) moment tensor point source at the coordinate origin, with the following equivalent body force

$$f^{\mathrm{DC}}(\boldsymbol{r},t) = -M_0(t)\left(\frac{\partial}{\partial z}e_x + \frac{\partial}{\partial x}e_z\right)\delta(\boldsymbol{r}), \tag{1.1}$$

where e_x and e_z are the unit vectors along the coordinate axes, $\delta(\boldsymbol{r})$ is the Dirac delta function, $M_0(t)$ is a seismic moment time function for which t is measured from the event onset. The point source causes a seismic displacement field $\boldsymbol{u}^{\mathrm{EQ}}(\boldsymbol{r},t)$ following the elasto-dynamic equation of motion

$$\rho_0 \ddot{\boldsymbol{u}}^{\mathrm{EQ}} = \boldsymbol{\nabla}\cdot\sigma + \boldsymbol{f}^{\mathrm{DC}}, \tag{1.2}$$

where ρ_0 is the undisturbed density and σ is the incremental stress tensor. The resulting density perturbation field $\delta\rho(\boldsymbol{r},t)$ is given by

$$\delta\rho = -\boldsymbol{\nabla}\cdot(\rho_0 \boldsymbol{u}^{\mathrm{EQ}}), \tag{1.3}$$

which is from the expanding P-waves and the deformation in the vicinity of the source. The density perturbation field is, then, related to the gravity potential change $\delta\psi(\boldsymbol{r},t)$ via the gravitation equation (i.e., Poisson's equation)

$$\nabla^2\delta\psi = -4\pi G\delta\rho, \tag{1.4}$$

where G is the gravitational constant, and the long-range square-root Newton's gravity interaction is considered, i.e., the propagation speed of gravity is approximated to be infinite, and thus, the potential starts to change over the whole space immediately after the event onset. Using the analytic solution of $\boldsymbol{u}^{\mathrm{EQ}}$ and $\delta\rho$ for an infinite homogeneous isotropic elastic medium (Aki and Richards 2002), Harms et al. (2015) derived the following closed-form expression for the pre-P gravity potential change

$$\delta\psi(\boldsymbol{r},t) = -R_{\mathrm{P}}\frac{3G}{r^3}I_2[M_0](t) \qquad \left(0 < t < \frac{r}{\alpha}\right) \tag{1.5}$$

and the pre-P gravity change $\delta\boldsymbol{g}$ as its spatial gradient. Here, R_{P} is the P-wave radiation pattern, $r = |\boldsymbol{r}|$, $I_2[M_0](t)$ is the second integral of $M_0(t)$ with respect to time, and α is the P-wave speed. We will refer to this model as Model 1.

The r^3-decay of the potential change is related to the spatial distribution of $\delta\rho$ (Harms et al 2015). Its radiation pattern has the shape of four lobes of alternating signs, i.e., quadrupole. As a monopole generates r-decay potential and a dipole generates r^2-decay one, The gravity potential generated by a quadrupole decays with r^3. On the other hand, the physical interpretation for the time dependency $I_2[M_0](t)$ has not been clearly provided. However, we may also be able to relate it to the radiation pattern of $\delta\rho$. Using the mass change $dm = \delta\rho\, dV$ in an infinitesimal volume dV, the mass quadrupole moment $Q(t)$ is expressed as

$$Q(t) = \int_V 3xz\, dm(\boldsymbol{r}, t) \tag{1.6}$$

(Harms et al. 2015), which is proportional to r^2 if ignoring the directional dependency. If the rupture process is instantaneous with duration Δt (so that $M_0(t)$ is a step function), the mass change carried by the P-wave exists only in the region $r = \alpha(t - \Delta t) \sim \alpha t$. Because the total mass carried by the P-wave is time invariant and proportional to $M_0(\infty)$, the quadrupole moment $Q(t)$ is proportional to $M_0(\infty)(\alpha t)^2$, which is the second integral of $M_0(t)$.

As a representative example, the waveform of the pre-P gravity change from the 2011 Mw 9.1 Tohoku-Oki earthquake is shown (Figure 1.1a). The moment time function obtained from seismic inversion analysis was employed (Wei et al. 2012). The waveform has a particularly smooth onset rich in low-frequency components and monotonically increases its amplitude owing to the second time integral. The amplitude reaches its maximum at the P-wave arrival time due to the density perturbation carried by the passing P-wave. The negative change indicates that the $\delta\boldsymbol{g}$ vector is pointing downward. This is the direction in which the gravity value changes from -9.8 to -9.9 m/s^2.

Figure 1.1b is the maximum signal-level distribution map. It shows that the peaks of the maximum amplitudes are approximately 800 km away from the epicenter, which is quite different from the seismic ground motion. This can be related to the finite rupture duration: in the vicinity of the source, only a small moment is released before the P-wave arrivals, resulting small $\delta\boldsymbol{g}$. On the other hand, at very distant stations, the strong distance decay of r^4 (recall that $\delta\psi$ has the r^3 decay) also makes $\delta\boldsymbol{g}$ small. The distance of 800 km approximately corresponds to the half-duration (100 s) of the employed moment function with the assumed P-wave speed α (= 7 km/s). The radiation pattern indicates that the $\delta\boldsymbol{g}$ vector is pointing downward in most of Japan's land area, i.e., the direction in which the gravity value changes from -9.8 to -9.9 m/s^2, and the vector is pointing upward in the region east to the hypocenter.

The predicted amplitude just before the P-wave arrival reaches the order of 10 nm/s^2. It is 10^{-9} times smaller than the gravitational acceleration g_0 (= 9.8 m/s^2) on the surface of the Earth. Therefore, the critical issue is whether such a small signal is detectable or not by using existing instruments such as superconducting gravimeters. Model 1 was referred to in the first detection report of the pre-P gravity signal in the data (Montagner et al. 2016), and we will also use it in Chapter 2. This model was extended to a homogeneous half-space with a free surface (Model 1'), where the flat surface reflects the incident seismic waves (Harms 2016). Model 1' was used to simulate the pre-P gravity-gradient signals in the feasibility analysis of earthquake detection using ultra-sensitive strainmeters (Juhel et al. 2018; Shimoda et al. 2020).

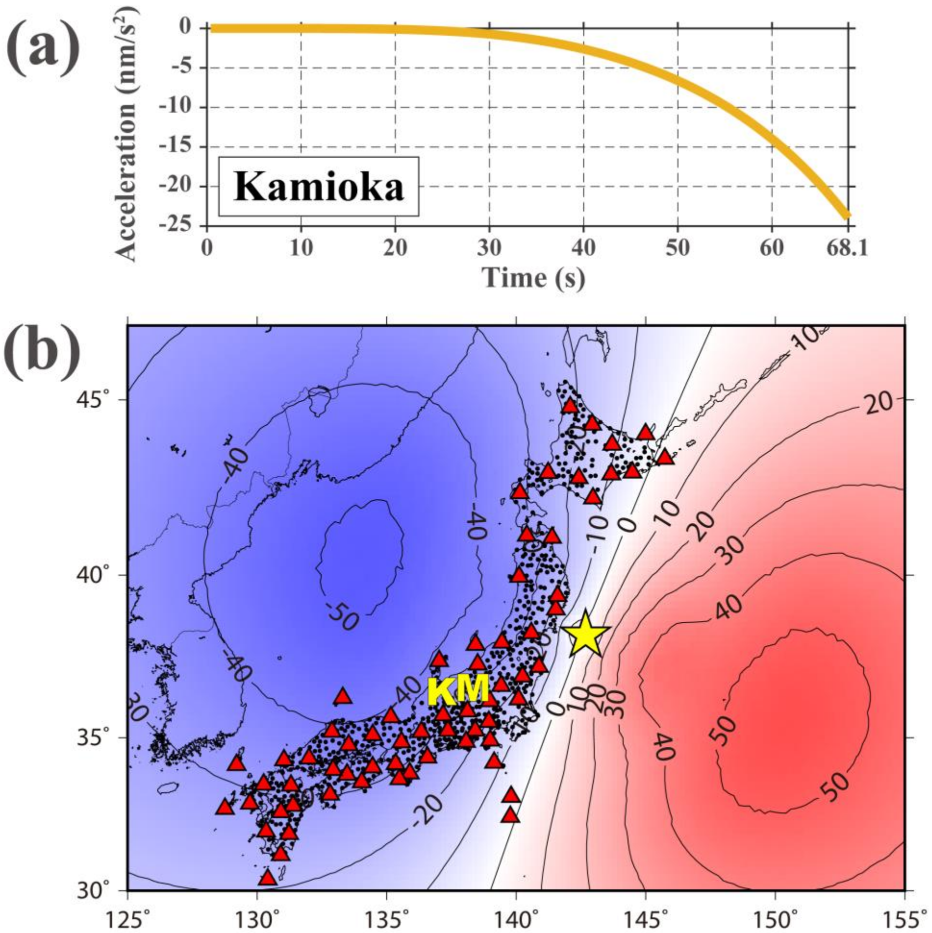
(a)
Acceleration (nm/s²)
0
-5
-10
-15
-20
-25
Kamioka
0
10
20
30
40
50
60
68.1
Time (s)
(b)
45°
40°
35°
30°
125°
130°
135°
140°
145°
150°
155°
KM
-50
-40
-30
-20
-10
0
10
20
30
40
50

Figure 1.1 (a) Model prediction of the pre-P gravity perturbation $(\delta \boldsymbol{g})_z$ (vertical component with upward positive) of the 2011 Tohoku-Oki earthquake for Kamioka Observatory. We used the infinite homogeneous Earth model of Harms et al. (2015), and no filter was applied. Time 0 was set to the event origin time t_{eq}. The P wave arrival time on the gravimetric record is 05:47:32.4 UTC (68.1 s after t_{eq}). (b) Distribution of the pre-P gravity perturbation $(\delta \boldsymbol{g})_z$ immediately before P-wave arrival at each location. The contour lines are drawn every 10 nm/s^2. The star, the letters K and M, the red triangle, and the small dots indicate the epicenter, Kamioka Observatory, Matsushiro Observatory, the 71 F-net stations, and the 706 tiltmeter stations, respectively.

1.1.2 Model 2 considering acceleration $\ddot{\boldsymbol{u}}^{\delta g}$ induced by $\delta\boldsymbol{g}$

A critical objection for the modeling of pre-P gravity signal was raised by Heaton (2017): Model 1 only focused on $\delta\boldsymbol{g}$ and did not consider the acceleration motion of the observation site. In the measurement of pre-P gravity perturbation $\delta\boldsymbol{g}$, it acts as a body force and induces the acceleration motion of the observation site $\ddot{\boldsymbol{u}}^{\delta g}(\boldsymbol{r},t)$ *before* the arrival of P-waves. This pre-P ground acceleration affects the gravimeter's output $(\boldsymbol{a})_z$ as

$$(\boldsymbol{a})_z = (\delta\boldsymbol{g})_z - \left(\ddot{\boldsymbol{u}}^{\delta g}\right)_z, \tag{1.7}$$

where $(\cdot)_z$ indicates the vertical component of the vector with an upward positive. He exemplified in a simple spherical Earth model that the Earth's motion due to the pre-P gravity perturbation mostly decreases the gravimeter's sensitivity, showing the importance of considering $\ddot{\boldsymbol{u}}^{\delta g}$.

As a direct answer to this objection, Model 2 was proposed by Vallée et al. (2017) and Kimura (2018): here, the displacement perturbation $\ddot{\boldsymbol{u}}^{\delta g}(\boldsymbol{r},t)$ induced by the distributed body force $\rho_0\delta\boldsymbol{g}$ is calculated, i.e., the effect of self-gravitation is taken into consideration. The elasto-dynamic equation of motion again describes the induced motion

$$\rho_0\ddot{\boldsymbol{u}}^{\delta g} = \boldsymbol{\nabla}\cdot\sigma + \rho_0\delta\boldsymbol{g}, \tag{1.8}$$

with the external body force $\rho_0\delta\boldsymbol{g}$. The closed-form solution can be derived in an infinite homogeneous isotropic elastic medium

$$\ddot{\boldsymbol{u}}^{\delta g}(\boldsymbol{r},t) = \delta\boldsymbol{g} \quad (0 < t < r/\alpha) \tag{1.9}$$

(Vallée et al. 2017, Kimura 2018). Interestingly, before the P-wave arrival, the gravity-induced acceleration motion at any place becomes the same as the pre-P gravity perturbation $\delta\boldsymbol{g}$ acting there. The self-gravity induced motion is essentially 'local free fall' at each point, for which gravimetry should be entirely cancelled out. This free fall motion is simultaneously noted as 'net-inner-force-free deformation' because equation (1.9) immediately means that $\boldsymbol{\nabla} \cdot \sigma = \boldsymbol{0}$ in equation (1.8) (Kame and Kimura 2019). This means that any part of the medium does not have elastic interaction with the surrounding part even under the non-uniform deformation. The characteristics of both incompressive ($\boldsymbol{\nabla} \cdot \boldsymbol{u}^{\delta g} = 0$) and irrotational ($\boldsymbol{\nabla} \times \boldsymbol{u}^{\delta g} = \boldsymbol{0}$) deformation are found to be inherent to the long-range interaction that obeys the inverse-square law, having no length scale. It is, so to speak, 'dark deformation', since we cannot sense the motion by gravimeters nor hear its sound by seismometers in the absence of compressive P-waves.

Although Model 2 predicts the zero signal output before the P-wave arrival, the real Earth has a free surface, and the deformation acceleration should deviate from equation (1.9). Vallée et al. (2017) numerically calculated $\delta\boldsymbol{g}$ and $\boldsymbol{u}^{\delta g}$ for a vertically stratified half space with a free surface and synthesized the pre-P gravity signal $(\delta\boldsymbol{g})_z - \left(\ddot{\boldsymbol{u}}^{\delta g}\right)_z$ as follows: first, the elasto-dynamic equation of motion (equation 1.2) is numerically solved, and the resulting density perturbation $\delta\rho$ is calculated at each grid point (equation 1.3). Then, the gravity change $\delta\boldsymbol{g}$ at each grid point is calculated through the three-dimensional volume integral corresponding to the Poisson's equation (equation 1.4), and the equation of motion (equation 1.8) is again numerically solved for the distributed body force $\rho_0 \delta \boldsymbol{g}$ to obtain $\ddot{\boldsymbol{u}}^{\delta \boldsymbol{g}}$ at the observation station. Here, the correction for the sphericity of the Earth was conducted with Earth flattening transform (Müller 1977; Müller 1985). Their model (Model 2’) was referred to in the second detection report of the pre-P gravity signal (Vallée et al. 2017).

Figure 3 in Vallée et al. (2017) shows the simulation results for the 2011 Tohoku-Oki event at the 11 stations they selected. In all waveforms, the amplitude is almost zero in the first half of the pre-P time window and increases in about the last third. This can be understood by the feature inferred from Model 1 (equation 1.5) that the time dependency is independent of the station location and monotonically increasing. In addition, the cancellation between $\ddot{\boldsymbol{u}}^{\delta \boldsymbol{g}}$ and $\delta \boldsymbol{g}$ and the 20-s characteristic phase delay of the applied band-pass filter (discussed in Chapter 3) would have decreased the amplitude in the first several tens of seconds. The negative change of the seismometer output indicates that the $\delta \boldsymbol{g}$ vector is pointing upward, if the induced ground acceleration $\ddot{\boldsymbol{u}}^{\delta \boldsymbol{g}}$ is not considered. This is the direction in which the gravity value changes from -9.8 to -9.7 m/s^2.

Juhel et al. (2019) extended this calculation scheme to a spherically symmetric Earth structure (Model 2’’). Using the normal modes of the Earth, they numerically solved the spherical version of the elasto-dynamic equation of motion (equation 1.2) and calculated $\delta \psi$ at each grid through a one-dimensional integral corresponding to the Poisson’s equation (equation 1.4). Then, similar to Model 2’, they again numerically solved the elasto-dynamic equation of motion (equation 1.8) for the distributed body force $\rho_0 \delta \boldsymbol{g}$ and obtained $\ddot{\boldsymbol{u}}^{\delta \boldsymbol{g}}$ at the observation station.

1.1.3 Model 3 considering fully coupled elasto-gravity equations in a spherical Earth

In the previous models, the interaction between the elastic deformation of the Earth and gravity change has been solved sequentially. The calculation results obtained in this way are considered to give an approximate solution for the fully coupled elasto-gravity equations, where the Earth's elastic deformation $\boldsymbol{u}$ and gravity change $\delta\psi$ evolve in time simultaneously. In a spherically symmetric Earth, the equations are expressed as follows:

$$\begin{gathered}\rho_0 \frac{\partial^2}{\partial t^2}\boldsymbol{u} = \boldsymbol{\nabla}\cdot\sigma + \rho_0\boldsymbol{\nabla}(\psi - g u_r) + \rho_0 g(\boldsymbol{\nabla}\cdot\boldsymbol{u})\boldsymbol{e}_r + \boldsymbol{f}^{\mathrm{DC}}, \\ \nabla^2\delta\psi = 4\pi G\boldsymbol{\nabla}\cdot(\rho_0\boldsymbol{u})\end{gathered} \tag{1.10}$$

where $\rho_0 = \rho_0(r)$ is the unperturbed density, $\sigma = \sigma(r,\theta,\phi,t)$ is the incremental stress tensor in the Lagrangian description, $\delta\psi = \delta\psi(r,\theta,\phi,t)$ is the incremental gravity potential in the Eulerian description, $g = g(r)$ is the undisturbed static Earth gravity (downward positive), r,θ,ϕ are the radial distance, polar angle, and azimuthal angle with the origin at the center of the spherically symmetric Earth, respectively, and $\boldsymbol{e}_r$ is the radial unit vector, respectively.

The solutions $(\boldsymbol{u},\delta\psi)$ for the fully coupled elasto-gravity equations (equation 1.10) in the time domain are composed of infinite sums of frequency-domain solutions, which are practically evaluated by their truncated sums. In the synthesis of pre-P gravity signals, however, it remains challenging to precisely evaluate the ground acceleration before the arrival of P-waves. This is because the direct P-waves with much larger amplitudes mask them through the leakage artifact originating from the truncation error (Juhel et al. 2019).

Zhang et al. (2020) developed a numerical method called leakage artifact reduction, where a theoretical synthesis for a different gravity coupling intensity in equation (1.10) is used to subtract the commonly contained leakage artifacts from the original synthesis. Through this technique, they succeeded in stably synthesizing the pre-P gravity change and ground acceleration as a superposition of forced oscillation solutions for equation (1.10).

The difference between the simulation results of this model (Model 3) and Model 2’’ is negligible for epicentral distances larger than 1000 km (Zhang et al. 2020). For closer stations, it becomes significant up to 40% although both fall within the uncertainty of single-channel data (figure S6 in Zhang et al. 2020). In Chapter 4, we will use Model 3 to synthesize the theoretical waveforms.

In Table 1.1, we summarized the progress of theoretical modeling for the pre-P gravity signal.

Table 1.1 Progress of theoretical modeling for pre-P gravity signal.

	Earth structure model	Computation of displacement $\boldsymbol{u}^{\mathrm{EQ}}$ by an earthquake double-couple	Computation of gravity change $\delta\boldsymbol{g}$ due to $\boldsymbol{u}^{\mathrm{EQ}}$	Computation of Additional displacement $\boldsymbol{u}^{\delta\boldsymbol{g}}$ induced by $\delta\boldsymbol{g}$	Synthesized pre-P signal
Model 1 Harms et al. 2015	Homogeneous full space	Elastic equation of motion (EEQM)	Poisson's equation (PE)	—	$\delta\boldsymbol{g}$
Model 1' Harms 2016	Homogeneous half space	EEQM	PE	—	$\delta\boldsymbol{g}$
Model 2 Vallee et al. 2017; Kimura 2018	Homogeneous full space	EEQM	PE	EEQM	$\delta\boldsymbol{g} - \ddot{\boldsymbol{u}}$ $(= \boldsymbol{0})$
Model 2' Vallee et al. 2017	Stratified half space with curvature	EEQM	PE	EEQM (distributed gravity source near station)	$\delta\boldsymbol{g} - \ddot{\boldsymbol{u}}$
Model 2" Juhel et al. 2019	Spherically symmetric Earth (PREM)	EEQM (See its Appendix A)	PE	EEQM (distributed gravity source near station)	$\delta\boldsymbol{g} - \ddot{\boldsymbol{u}}$
Model 3 Zhang et al. 2020	Spherically symmetric Earth (Modified AK135)	Fully coupled elasto-gravity equations			$\delta\boldsymbol{g} - \ddot{\boldsymbol{u}}$

1.2 Search for pre-P gravity signals from the 2011 Mw 9.1 Tohoku-Oki earthquake

A study by Montagner et al. (2016) was the first to report the existence of the pre-P gravity signal in observed data. They searched for the signal from the 2011 Mw 9.1 Tohoku-Oki earthquake in the records of a superconducting gravimeter (SG) at Kamioka (approximately 510 km from the epicenter) and five nearby broadband seismometers of the Full Range Seismograph Network of Japan (F-net). Though they failed to identify a signal with an amplitude that was obviously above the background noise level, they found that the 30-s-average value immediately before the P-wave arrival was more prominent than the noise level with a statistical significance greater than 99% (corresponding to approximately 2.6σ if the background noise has a normal distribution, where σ is the standard deviation of the noise). In addition, the detected signal was consistent with the prediction of Model 1 in terms of the sign and order of magnitude. Based on this finding, they claimed the presence of a pre-P gravity signal from the event.

The second detection report by Vallée et al. (2017) was conducted based on data analysis and theoretical modeling. From the records of regional broadband seismic stations in the Japanese islands and the Asian continent, they selected 11 waveforms based on the study’s criteria. Nine waveforms among them showed a consistent visible downward trend starting from the origin time up to the respective P-wave arrival times (Figure 1 of Vallée et al. 2017). They then numerically simulated the signals for the 11 stations using Model 2’. The 11 pairs of observed and synthetic waveforms showed similarities to one another (Figure 3 in Vallée et al. 2017).

However, to confirm the existence of the pre-P gravity signal, stronger evidence was needed. The statistical significance of 99% presented by Montagner et al. (2016) was too low to claim an anomaly. For example, in the field of elementary particle research, the statistical significance of 3σ (approximately 99.7%) is regarded as a ‘sign’ of a new phenomenon, and 5σ (approximately 99.9999%) is required for ‘discovery’. In the report of Vallée et al. (2017), such a significance of the observed trends was not presented, and there was another problem concerning the signal processing method: artifacts originating from the acausal process applied to remove the instrumental response may have contaminated the original records. The amplitudes of such artifacts remained unevaluated.

1.3 Applicability for early warnings and scientific significance of the pre-P gravity signal

So far, the value of the pre-P gravity signal has been focused on its contribution to future earthquake and tsunami early warnings. Harms et al. (2015) estimated the magnitude of the pre-P gravity gradient and proposed that it can be detected by the next generation ultra-sensitive gravity gradiometers such as atom-interferometer, torsion-bar antennas, or superconducting gravity strainmeter, within approximately 10 seconds after the earthquake occurrence. Vallée et al. (2017) suggested that the amplitude of the pre-P gravity signal could reveal the magnitude of the earthquake to be at the M9 level in a few minutes, which would be useful for tsunami warning, although the observation in acceleration was suffered from the ground vibration noise and the cancellation by the gravity-induced acceleration (Model 2’) so that the fast detection of the earthquake was difficult. Currently, feasibility analyses of the observations of pre-P gravity gradient using the above future generation gravity gradiometers have been conducted (Juhel et al. 2018; Shimoda et al. 2020), and the development of the devices to obtain the necessary accuracy is awaited.

On the other hand, little attention has been paid to the scientific significance of this signal, and it remains unclear what and how a new geophysical constraint or implication can be obtained through the observation of this signal. Zhang et al. (2020) performed an inversion analysis using the simulation method that they developed (Model 3). The estimated source parameters of the 2011 Tohoku-Oki earthquake from the vertical broadband seismometer data were generally consistent with seismologically estimated values like the CMT solution, but a new constraint on the source was not shown. In addition, the similar difficulty as seen in the analysis of long-period seismic data remained, i.e., the trade-off between the moment magnitude and dip angle (Kanamori and Given 1981).

1.4 Purpose of this study

The purpose of this study is to show that pre-P gravity signals can provide a new scientific finding about earthquakes that cannot be obtained from seismology and to give this research field a complementary role to seismology. For this purpose, we aimed to confirm the existence of the pre-P gravity signal, establish a basis for the quantitative comparison between observation and theoretical modeling, and then use the signal for source inversion to obtain a new constraint on the source parameters.

In Chapter 2, we aimed to confirm the existence of the pre-P gravity signal with the evaluation of the signal amplitude in order to construct a quantitative anchor point from observation. We analyzed superconducting gravimeter data and broadband seismometer and tiltmeter array data in Japan. As a result of a causal and artifact-free signal processing, we detected a signal from the 2011 event with the statistical significance of 7σ in the stacked seismometer records. The lower limit of the signal amplitude was constrained to 0.25 nm/s^2 (2-30 mHz) at an average distance of approximately 1000 km from the hypocenter.

In Chapter 3, we aimed to establish a basis for the quantitative comparison between observation and theoretical modeling by assessing the influence of the acausal signal processing method of Vallée et al. (2017) on the detected signal amplitudes. First, we applied this process to acceleration waveforms having a signal-like shape and showed that the artifacts were negligible compared to the signal amplitude. Then, we evaluated the maximum amplitude of the artifact when the process was applied to a noise waveform. Again, the artifact was sufficiently small compared to the detected signals. These results assured that the trends before the P-wave arrival presented by Vallée et al. (2017) were not artifacts and enabled us to compare the synthetic waveforms with the observed ones after deconvolving the instrumental response. We applied this method in Chapter 4.

In Chapter 4, we proceeded to the quantitative use of the pre-P gravity signal and aimed to obtain a new constraint on the source parameters. First, we re-analyzed the tiltmeter array data by using the synthetic waveforms calculated by Model 3, resulting in a clear detection of the horizontal components of the signal from the 2011 event. Next, we performed a waveform inversion analysis to estimate the source parameters. The tiltmeter data, combined with the vertical component of the broadband seismometer array data, yielded a constraint on the dip angle and magnitude of the earthquake in the range of 11.5°–15.3° and 8.75–8.92, respectively. Our results indicate that the analysis of the three components of the pre-P gravity signal avoids the intrinsic trade-off problem between the dip angle and seismic moment in determining the source mechanism of shallow earthquakes from long-period seismic data.

In Chapter 5, we summarized our conclusions.

2. Pre-P gravity signal identified in dense array data in Japan

This chapter is modified from Kimura et al. (2019a), which was published in Earth, Planets and Space.

2.1 Introduction

As reviewed in Chapter 1, Montagner et al. (2016) and Vallée et al. (2017) reported the detection of the pre-P gravity signal from the 2011 Tohoku-Oki earthquake, but further evidence that strongly indicates the existence of the signal was needed. In this study, we searched for pre-P gravity signals from the 2011 event using an objective approach, i.e., with a sufficient statistical significance for the discovery of a new phenomenon and with a causal and artifact-free signal processing method. We first analyzed SG data at two stations (subsection 2.4.1), but signal detection was unsuccessful. Next, we analyzed records of the dense arrays of F-net (subsection 2.4.2) and High Sensitivity Seismograph Network Japan (Hi-net) (subsection 2.4.3). Although most single-channel records did not show any signal beyond the noise level, we optimized the multi-channel data through waveform-stacking, which successfully reduced the noise level and allowed identification of a prominent signal in the F-net vertical data.

2.2 Data

We analyzed three different types of data: gravity data from two SGs, vertical ground velocity data from the F-net seismographic array, and ground tilt data from the Hi-net tiltmeter array. The station locations are indicated in Figure 1.1. These instruments are listed in Table 2.1. The instrumental responses of SG, STS-1, and STS-2 to the acceleration input are shown in Figure 2.1.

The SG data were recorded at a 40-Hz sampling rate (GWR5 channel) (Imanishi 2001). Because the instrument response was flat under 0.03 Hz (Figure 2.1), we did not remove the response from the records. Figure 2.2 shows the noise power spectrum. In contrast to the 1-Hz sampling data (GGP1 channel) with a 0.061-Hz anti-aliasing filter used in the analysis of Montagner et al. (2016), our 40-Hz sampling data contain the signal power in the frequency range higher than 0.061 Hz. After removing the trend component before t_{eq} and multiplying a cosine taper in the first and last 10% sections of the time series, we applied a band-pass filter (five-pole 0.001-Hz high-pass and five-pole 0.03-Hz low-pass causal Butterworth filters) to the 1-h data (05:00–06:00 UTC) to reduce the relatively large noise power higher than 0.05 Hz. The lower corner frequency of 0.001 Hz was set to remove the long period tidal variation.

All 71 F-net stations are equipped with STS-1 or STS-2 broadband seismometers. The frequency responses of the F-net STS-1 seismometers to velocity are flat between 0.003 and 10 Hz (Figure 2.1). Consequently, we did not deconvolve the sensor frequency responses from the recorded waveforms, and the vertical velocity data were converted to acceleration data taking the finite difference in the time domain. This is the crucial difference from the signal processing procedure employed by Vallée et al. (2017), where the instrument response was removed through the frequency-domain calculation. The details of the signal processing procedure employed by Vallée et al. (2017) and the procedure of ours are described in Appendix A and B. The typical value of the noise level was 1000 nm/s^2 (340 nm/s^2 was the lowest value) dominated by the microseism. To reduce the microseismic noise, we applied the same filters (0.002-Hz two-pole high-pass and 0.03-Hz six-pole low-pass causal Butterworth filters) employed in Vallée et al. (2017) for all available data from 70 of the 71 stations (omitting one because of the poor recording quality).

A two-component borehole tiltmeter is installed at 706 Hi-net stations and work as horizontal accelerometers. For our analysis, the tilt data in rad were converted into horizontal acceleration in m/s^2 by multiplying with the gravity acceleration (-9.8 m/s^2). Because the sensor response is not known in the seismic frequency band, we could not deconvolve it from the data; however, tiltmeter records have been used as seismic records by comparing them to nearby broadband seismic records (e.g., within a bandwidth of 0.02–0.16 Hz) (Tonegawa et al. 2006). Because tiltmeters are designed to respond to static changes, recordings are also reliable below 0.02 Hz. When compared to the F-net data, the Hi-net tiltmeter data were generally noisy. The typical noise level was 2000 nm/s^2. After removing the trend component before t_{eq}, we applied the same band-pass filter as employed in Vallée et al. (2017).

Table 2.1 Observation instruments.

Instrument	Channels used	Sampling rate	Distance from the hypocenter	Output used
Superconducting gravimeter	2 (Kamioka and Matsushiro)	40 Hz	515 km (Kamioka), 436 km (Matsushiro)	Vertical gravity acceleration [m/s^2]
Broadband seismometer	27 out of 71 (F-net)	20 Hz	From 505 km to 1421 km	Vertical ground velocity [m/s] converted to acceleration [m/s^2]
Tiltmeter	553 out of 1412 (Hi-net)	20 Hz	From 264 km to 1349 km	Ground tilt [rad] converted to horizontal acceleration [m/s^2]

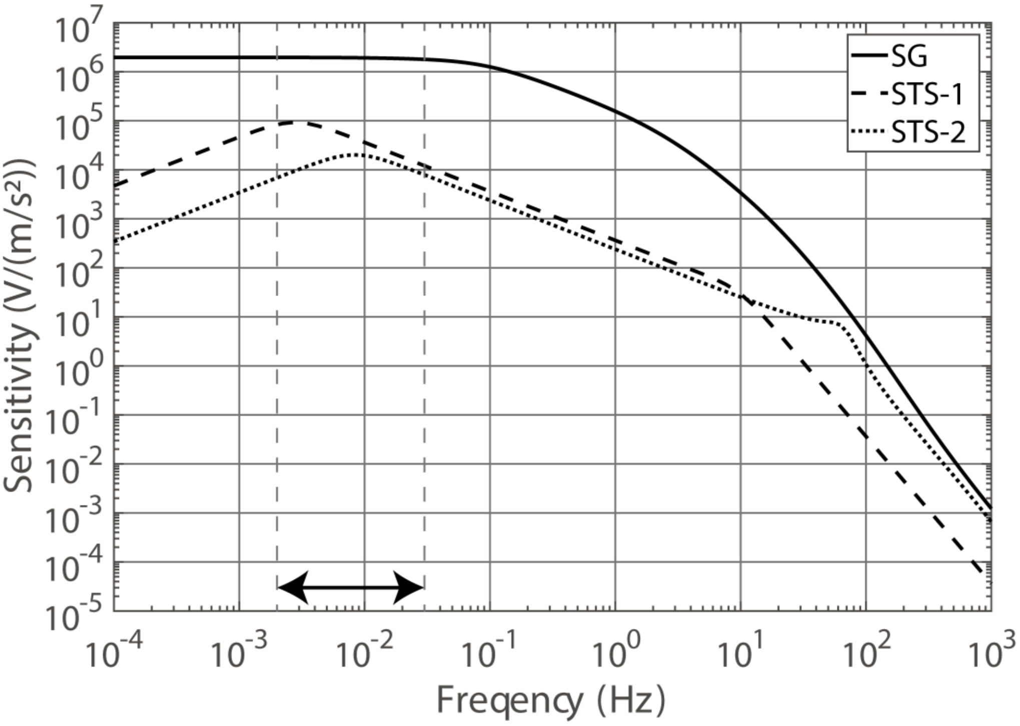

Figure 2.1 Diagram of the instrumental responses of SG, STS-1, and STS-2 to acceleration input. The frequency range of our band-pass filtering between 0.002 – 0.03 Hz is indicated by arrows on the horizontal axis.

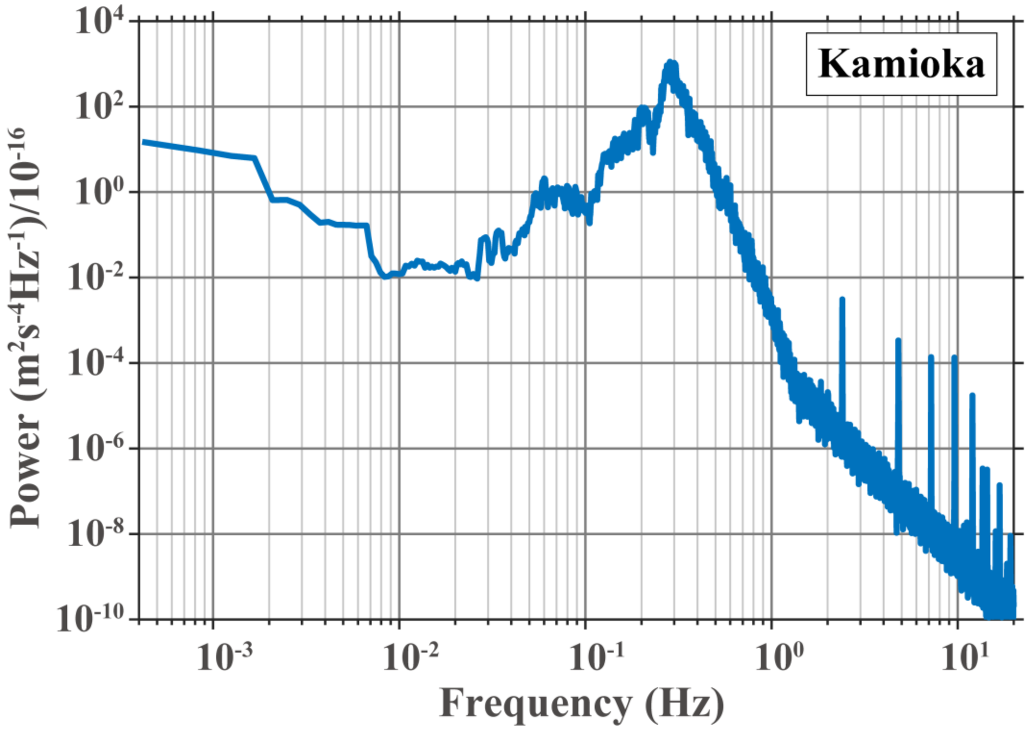

Figure 2.2 Noise power spectrum of the Kamioka SG data. The time window is 40 min between 05:00 and 05:40 UTC before the 2011 Tohoku-Oki event. The instrument response is included.

2.3 Methods

2.3.1 Detection criterion

To confirm the existence of the pre-P gravity signal, we set the detection criterion as 5σ, which is a sufficient statistical significance for the discovery of a new phenomenon. Here, σ is the standard deviation of the background noise defined as

$$\sigma = \sqrt{\frac{1}{t_2 - t_1}\int_{t_1}^{t_2} [x(t) - \mu]^2 dt},$$

where $x(t)$ is time-series data and $\mu = \frac{1}{t_2 - t_1}\int_{t_1}^{t_2} x(t)dt$.

2.3.2 Waveform simulation for stacking

In the analyses of the broadband seismometer and tiltmeter array data, we conducted waveform stacking in order to enhance the signal relative to the background noise. To select the favorable stations and make polarity reversal correction for the purpose, we used the model prediction of Harms et al. (2015), i.e., Model 1, as the reference. The detail of the selection criterion is described in Appendix C.

2.4 Results

2.4.1 Superconducting gravimeters

Figure 2.3a shows the filtered Kamioka SG data (515 km from the hypocenter and $t_{\mathrm{P}} = t_{\mathrm{eq}} + 68.1$ s). During the time period $t_{\mathrm{eq}} < t < t_{\mathrm{P}}$, we do not see any signal with amplitudes far beyond the noise level of the record prior to the event origin time. For the data, $\sigma = 0.4$ nm/s^2 ($t_1 = 05{:}40$ UTC and $t_2 = t_{\mathrm{eq}}$). Figure 2.3b shows the data for Matsushiro (436 km from the hypocenter and $t_{\mathrm{P}} = t_{\mathrm{eq}} + 57.3$ s) after the same filtering process. Although σ decreased to 0.7 nm/s^2 after the filtering, we did not recognize a clear signal before t_{P}. Note that the oscillation with the period of approximately 90 s is a parasitic mode of the instrument (Imanishi 2005; 2009).

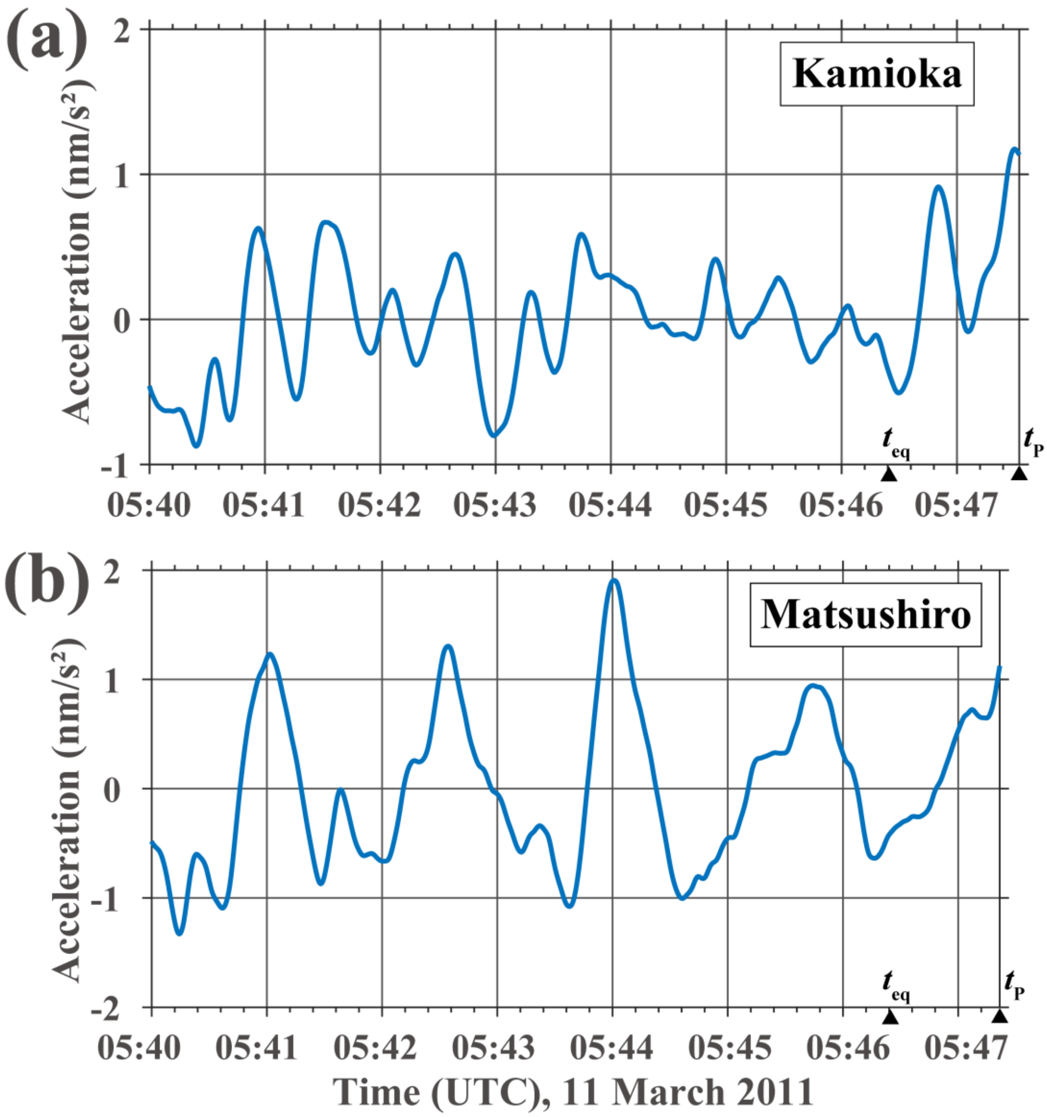

Figure 2.3 0.001–0.03-Hz band-pass-filtered SG data at (a) Kamioka and (b) Matsushiro. The instrument response is included.

2.4.2 F-net broadband seismometers

Figure 2.4 shows the filtered F-net broadband seismometer vertical data. The microseism noise was successfully reduced to as low as 0.2 nm/s^2. However, we did not recognize clear signals. Only at two stations, FUK and SBR, could we find a downward trend before P-wave arrival.

Next, a multi-station signal-stacking method was applied to further enhance the signals of interest. After the band-pass filtering, we selected 27 traces out of the 70 traces and stacked them aligned with t_P at each station because we expected the maximum signal amplitude immediately before t_P (Figure 1.1a).

Figure 2.5a shows the stacked trace. The noise of the stacked trace significantly decreased, and the trace successfully showed a significant signal with an amplitude of 0.25 nm/s^2. The stacked 27 stations are listed in Table 2.2. The hypocentral distances of the 27 stations are between 505 and 1421 km (the average is 987 km), and the minimum and maximum t_P are 63 and 176 s after t_eq, respectively.

The negative change of the stacked trace indicates that the polarity of the detected pre-P signal is opposite to the prediction of the reference model, i.e., Model 1. As seen in Figure 1.1, Model 1 predicts that the pre-P gravity change $\delta \boldsymbol{g}$ is in the direction where the gravity value changes from -9.8 to -9.9 m/s^2 in most of Japan’s land area. The detected signal is, therefore, in the direction where the gravity value changes from -9.8 to -9.7 m/s^2 if the induced ground acceleration $\ddot{\boldsymbol{u}}^{\delta g}$ is not considered.

To quantify the signal detection in terms of statistical significance, we investigated the distributions of the background noise and enhanced pre-P gravity signal. Figure 2.6 shows the histograms of the noise section (between −30 and −3 min before the aligned t_P) and the signal section in the stacked trace. Here, we defined the latter half of the time period -1 min (≒ minimum $t_\mathrm{P} - t_\mathrm{eq}) < t < 0$, i.e. −30 s $< t < 0$ as the signal section because all 27 waveforms were expected to contain a signal with increasing amplitude toward the end of this time period, as shown in Figure 1.1a. The noise histogram was approximated by a normal distribution with a standard deviation σ (0.035 nm/s^2). On the other hand, before the aligned t_P, the amplitude of the stacked trace generally increased with time and the signal level exceeded 3σ at $t = -20$ s and 5σ at $t = -6$ s before finally reaching 7σ at $t = 0$ (Figure 2.5a), i.e., the signal detection was verified with a statistical significance of 7σ.

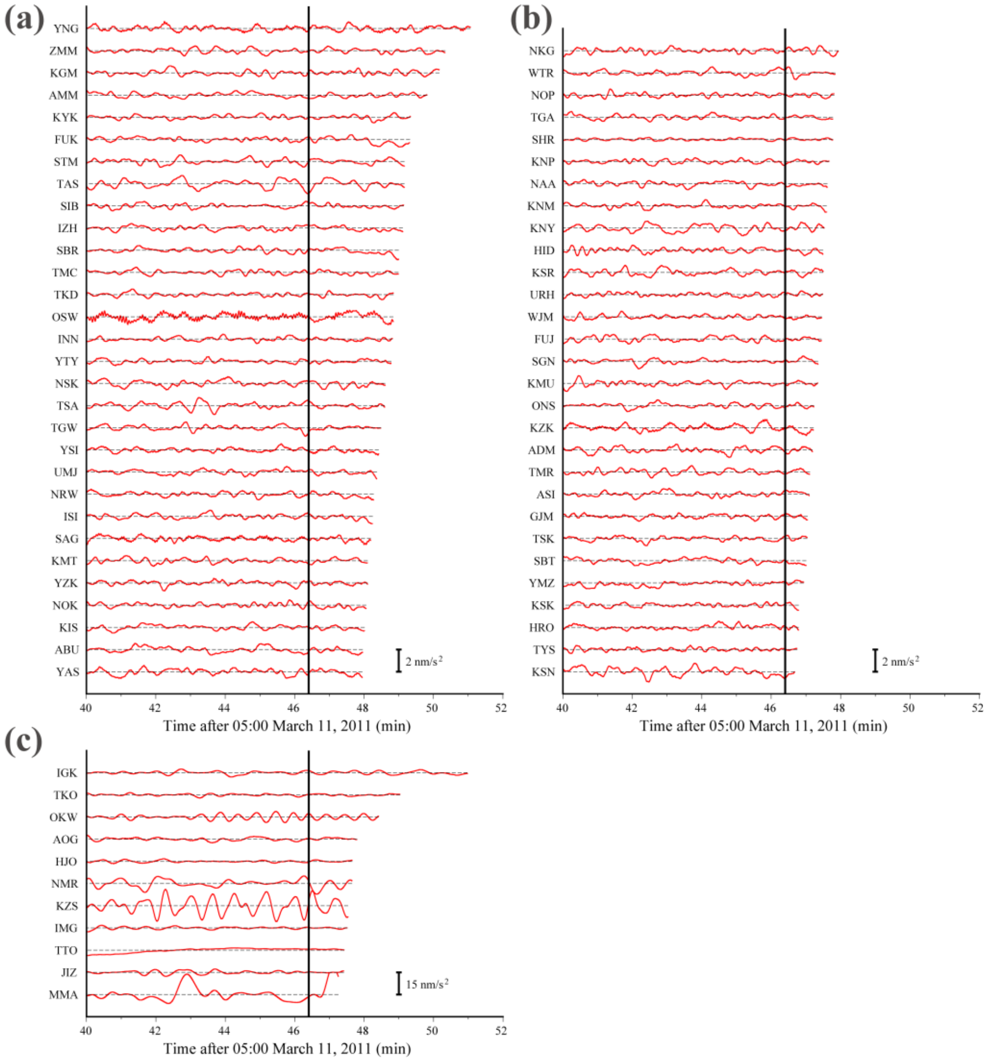

Figure 2.4 Acceleration waveforms at 70 observation stations in the F-net before the P-wave arrival from the 2011 Tohoku-Oki earthquake. The black vertical line indicates the event origin time. They were processed with Proc. K, which is a causal process (see Appendix B). (a) Waveforms at 30 stations where the P-wave arrival times are more than 93 seconds after the event origin time. Their background noises were less than 1 nm/s^2. (b) Waveforms at 29 stations where the P-wave arrival times are less than 93 seconds after the event origin time. Their background noises were less than 1 nm/s^2. (c) Waveforms at 11 stations with their background noises more than 1 nm/s^2.

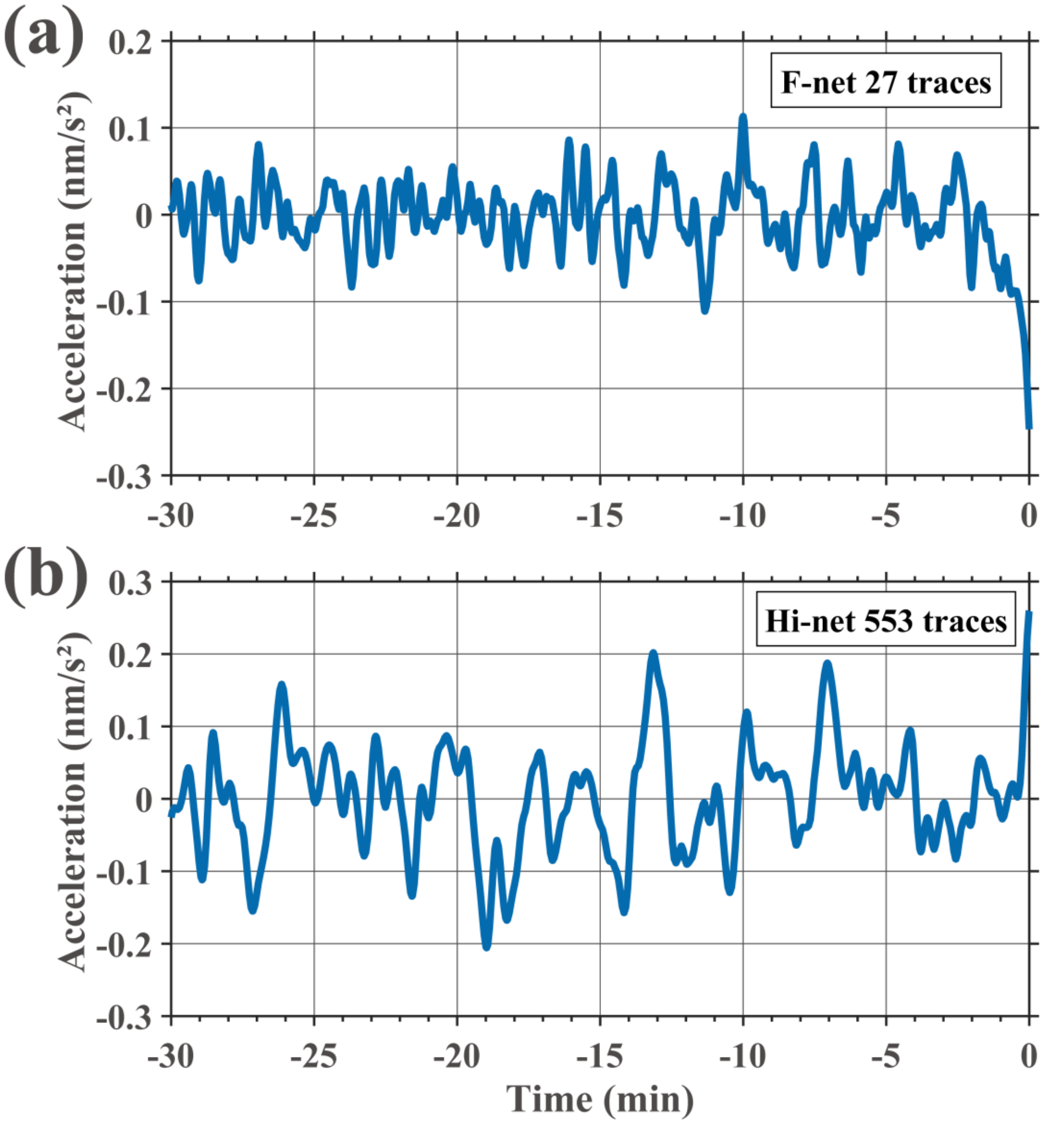

Figure 2.5 Stacked waveforms of the filtered data for 30 min before the P-wave arrivals. Time 0 was set to the stacking reference time t_P. (a) Plot for F-net broadband seismometer vertical data. (b) Plot for Hi-net horizontal tiltmeter data.

Table 2.2 27 F-net stations used for the stacking. Polarity of P-wave and Polarity of δg^{H} (see Appendix C) are vertically upward positive.

Station Name	Distance from Hypocenter [km]	Polarity of P-wave	Polarity of δg^{H}
KYK	1421	+	-
FUK	1398	+	-
SIB	1317	+	-
STM	1311	+	-
IZH	1289	+	-
SBR	1234	+	-
TMC	1233	+	-
TKD	1183	+	-
INN	1151	+	-
YTY	1130	+	-
TSA	1050	+	-
NSK	1048	+	-
TGW	993	+	-
YSI	934	+	-
UMJ	932	+	-
NRW	902	+	-
ISI	869	+	-
SAG	857	+	-
KMT	819	+	-
YZK	810	+	-
NOK	796	+	-
KIS	777	+	-
ABU	735	+	-
YAS	725	+	-
TGA	657	+	-
KNM	561	+	-
WJM	505	+	-

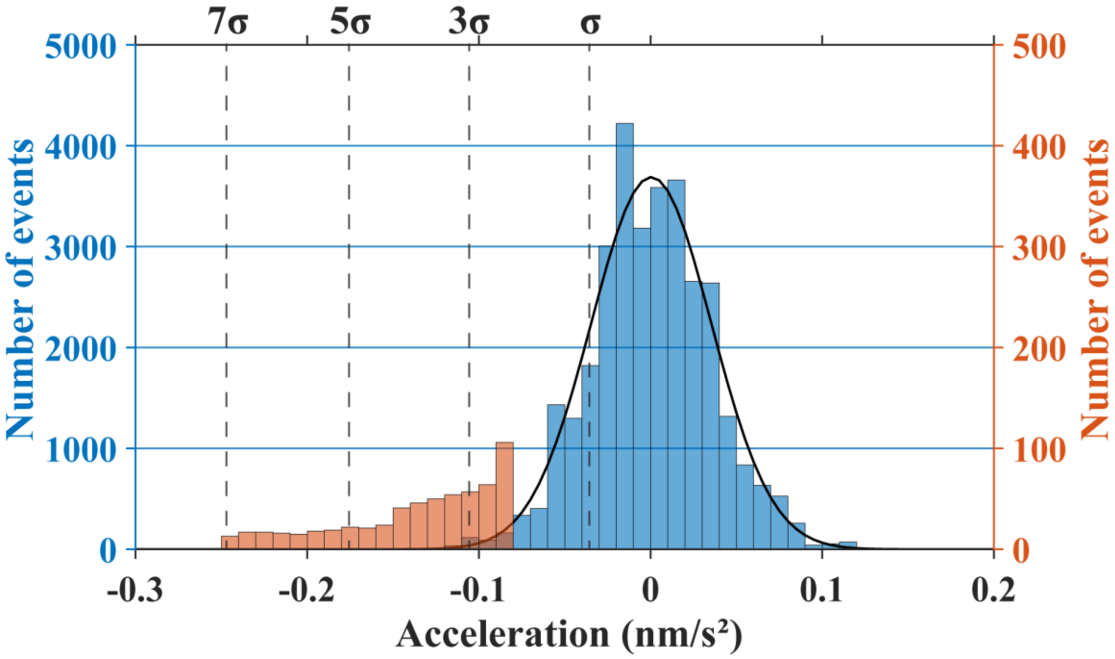

Figure 2.6 Amplitude histograms of the background noise (blue) and the pre-P gravity signal (red). The noise histogram was fitted by a normal distribution with a standard deviation $\sigma = 0.035$ nm/s^2 (black curve).

2.4.3 Hi-net tiltmeters

After the band-pass filtering, we again failed to identify a significant signal in each channel. We then aligned 553 traces out of 1412 traces (two horizontal components from each station) with respect to the P-wave arrival times for stacking. The hypocentral distances of the 553 traces are between 264 and 1349 km (the average is 830 km). Figure 2.5b shows the stacked trace. In contrast to the F-net results, the pre-P signal was not identified. The noise level σ was 0.08 nm/s^2.

The predicted signal amplitude of the stacked trace based on the infinite homogeneous Earth model of Harms et al. (2015) was 2 nm/s^2 (Kimura 2018), where the theoretical time series were synthesized at each station and then filtered and stacked in alignment with the P-wave arrival time in the same manner as the observed data. In our analysis, such a large signal was confirmed not to exist in the data.

2.5 Discussion

2.5.1 Difference from previous observation studies

Our failure of detecting pre-P gravity signals in the SG data is consistent with the result of Montagner et al. (2016), who also analyzed the Kamioka SG and five nearby F-net stations and could not visually detect a clear signal in the time domain. On the other hand, at the Global Seismographic Network (GSN) station Matsushiro (MAJO), a signal detection was reported by Vallée et al. (2017). GSN MAJO and the Matsushiro SG are installed in the same tunnel, and the Kamioka SG and the five nearby F-net stations in Montagner et al. (2016) are located at nearly the same epicentral distance. The results of Montagner et al. (2016) and Vallée et al. (2017) seems inconsistent with one another. The signal at GSN MAJO shown in Vallée et al. (2017) may have been a mere noise or affected by a local site response. Notably, the polarity of our stacked trace shows a negative trend toward the P-wave arrival, consistent with the observation and simulation of Vallée et al. (2017) but inconsistent with the results of Montagner et al. (2016).

2.5.2 Significance of our stacked trace on theoretical modeling

The F-net stacked trace (Figure 2.5a) showed a great improvement of the statistical significance of the signal detection. It provides a constraint of pre-P gravity signals by observation and can work as a reference to validate future theoretical models. Once a model is developed that explains the sensor output in gravimetry and the reliable value of $\delta\boldsymbol{g}$ is constrained, related physical quantities such as gravity gradient and spatial strain are constrained as well.

Vallée et al. (2017) numerically investigated $\delta\boldsymbol{g}$ and the induced site motion $\ddot{\boldsymbol{u}}$ when exposed to the effects of a free surface in a layered non-self-gravitating half-space and evaluated the sensor output $-(\delta\boldsymbol{g})_z + (\ddot{\boldsymbol{u}})_z$. Their simulated waveforms at the 11 stations showed the same downward monotonic trend and similar amplitude of approximately 1 nm/s^2 within the wide range of 427–3044 km from the hypocenter. This simulated signal amplitude of 1 nm/s^2 is significantly larger than our identified amplitude of 0.25 nm/s^2 in the F-net stacked trace. This discrepancy may be attributed to the difference of applied signal processing (i.e., Proc. V and K, see Appendix A and B) or the overestimation of the simulation of Vallée et al. (2017).

2.5.3 Possible reasons for no finding with tiltmeters

The lack of signal identification in the stacked Hi-net trace (Figure 2.5b) can be attributed to the reference model used for the waveform stacking analysis. We performed the data selection and polarity reversal based on the synthetic amplitudes expected from Model 1 (Harms et al. 2015), which simulated only the gravity perturbation $\delta \boldsymbol{g}$ in an infinite homogeneous medium. It is thought that the effect of the free surface and induced $\ddot{\boldsymbol{u}}$ significantly change the amplitude distribution of the horizontal components of the pre-P gravity signal, making the stacking based on Model 1 less effective. In Chapter 4, we again analyze the tiltmeter array data by using Model 3, i.e., the model which numerically solves the fully coupled elasto-gravity equations for a spherically symmetric Earth and synthetize $\ddot{\boldsymbol{u}} - \delta \boldsymbol{g}$.

2.5.4 Toward future detection of pre-P gravity signals using a gravity-gradient sensor

We have shown that the identified pre-P gravity signals were very small (approximately 0.25 nm/s^2 for the average distance of 987 km); this can be attributed to the cancelation of gravity measurements by the acceleration motion of the ground and suggests that gravimetry is not the best approach for detecting pre-P gravity signals. A gravity-gradient measurement provides an alternative method to detect the signals (Harms et al. 2015; Juhel et al. 2018). A spatially inhomogeneous gravity field induces tidal deformation of an object or spatial strain, which is observable even if the observer moves with the same acceleration as the pre-P gravity perturbation.

Detecting very small perturbations in the gravity gradient has been a challenge in identifying gravitational waves from space. Abbott et al. (2016) observed gravitational waves using laser interferometers in a high frequency range from tens to hundreds of Hz. New state-of-the-art instruments, such as torsion bar antennas (TOBA) (Ando et al. 2010; Shoda et al. 2014), are being developed. Such instruments are intended to observe spatial strain through the tidal deformation of two crossing bars.

The existing prototype TOBA attained a 10^{-8} s^{-2} sensitivity within a low-frequency range of 0.01–1 Hz (Shoda et al. 2014). The theoretical gravito-gradiograms and the pre-P-signal intensity map are shown for the 2011 Tohoku-Oki earthquake (Figure 2.7). The expected signal level was 10^{-13} s^{-2}. Though this value is 10^{-5} times smaller than the attained sensitivity, the next-generation TOBA will attain sufficient sensitivity to detect the signals. Prompt earthquake detection will significantly benefit from such ultra-sensitive sensors.

In Appendix D, we present an explicit expression of theoretical gravito-gradiograms, the waveforms of gravity gradients. We extended the expression of Harms et al. (2015), who used a seismic dislocation source, to a general source described as a moment tensor. Our extension will contribute to the interpretation of future observational records of various event mechanisms.

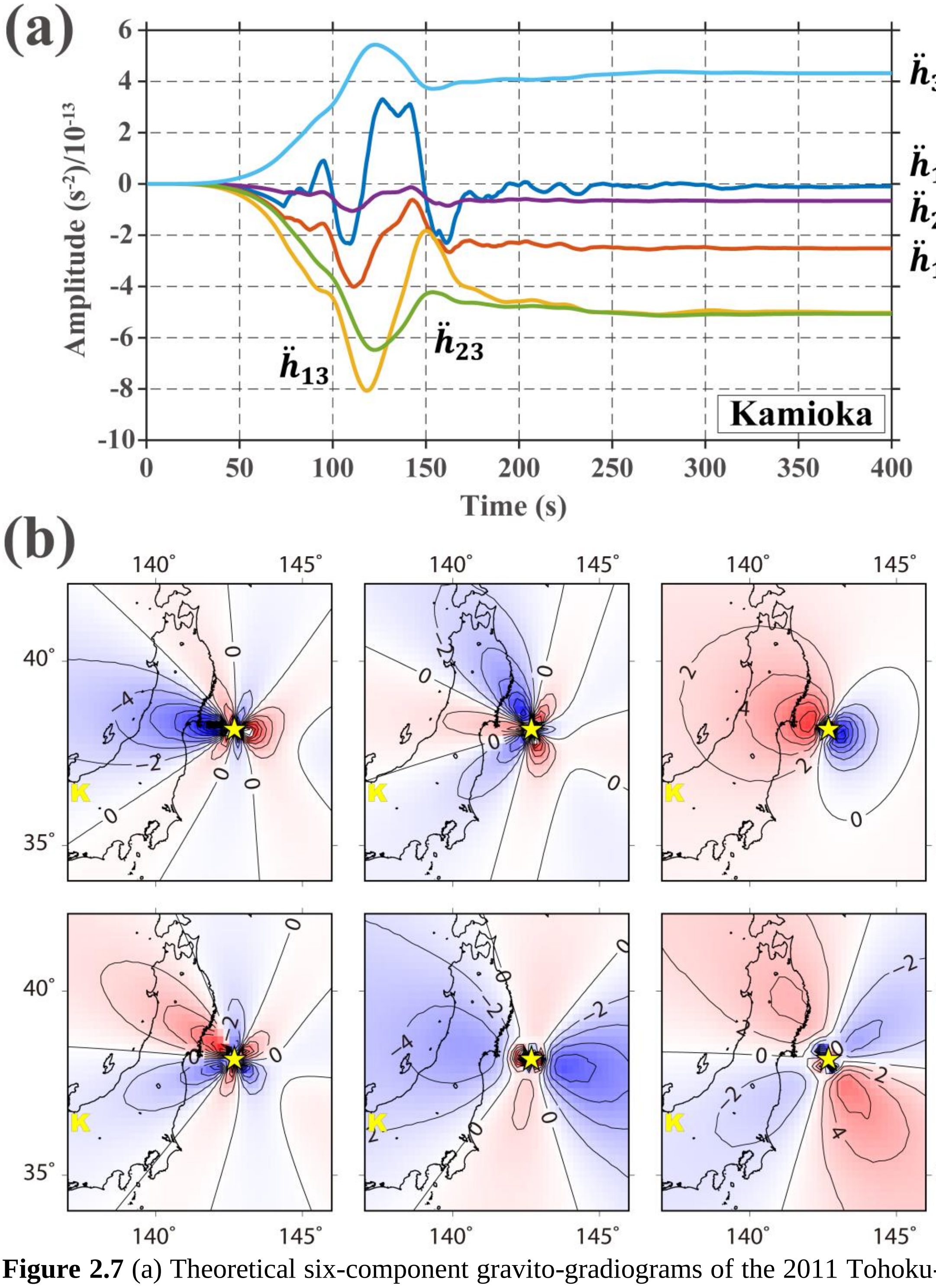

Figure 2.7 (a) Theoretical six-component gravito-gradiograms of the 2011 Tohoku-Oki earthquake synthesized for Kamioka Observatory. Time 0 was set to the event origin time t_{eq}. (b) Distribution of pre-P gravity-gradient changes immediately before P-wave arrival at each location (upper left: $\ddot{h}_{11}$ component, upper center: $\ddot{h}_{22}$ component, upper

right: $\ddot{h}_{33}$ component, lower left: $\ddot{h}_{12}$ component, lower center: $\ddot{h}_{13}$ component, and lower right: $\ddot{h}_{23}$ component), where $\ddot{h}_{ij}$ denotes the *ij*-th component of the gravity gradient tensor (see Appendix D). In these figures, the x_1-, x_2-, and x_3-axes correspond to the directions of east, north, and upward, respectively. The star and the letter K are the epicenter and Kamioka Observatory, respectively. The contour lines are drawn every $2 \times 10^{-13}\ \mathrm{s}^{-2}$.

2.6 Conclusions

We searched for pre-P gravity signals from the 2011 Mw 9.1 Tohoku-Oki earthquake in seismic network data. Though nearly all the single-channel waveforms did not show any signals beyond the noise level except for several outliers, the stacked trace of F-net broadband records showed a clear signal in the vertical component. The identified signal level was 0.25 $\mathrm{nm/s^2}$ for the average distance of 987 km; this detection was verified at a statistical significance of 7σ to the background noise. The stacked F-net trace is the first constraint of pre-P gravity signals by observation and will be used as a reference to validate theoretical models. Measurement of gravity gradients is a more promising method in the prompt detection of future earthquakes. State-of-the-art instruments, such as torsion bar antennas, are being developed to detect strain acceleration smaller than $10^{-13}\ \mathrm{s}^{-2}$.

3. Evaluation of artifacts caused by acausal signal processing employed by Vallée et al. (2017)

This chapter is modified from Kimura et al. (2019b), which was published in Earth, Planets and Space.

3.1 Summary

Vallée et al. (2017) reported the detection of pre-P gravity signals in broadband seismograms during the 2011 Tohoku-Oki earthquake. In Chapter 2, we considered that their detection involved some uncertain points, including a concern regarding their signal processing procedure. Specifically, to remove the instrumental response, Vallée et al. (2017) applied acausal deconvolution to the seismograms truncated at the P-wave arrivals (Appendix A). Generally, acausal deconvolution produces artifacts at the edge of the time window. However, they did not present quantitative assessment whether the detected signals were artifacts due to the signal processing. To avoid this concern, we employed another procedure that eliminated acausal processes, resulting in the detection of a pre-P signal with a statistical significance of 7σ in stacked broadband seismograms (Chapter 2). Here, we assessed the validity of the procedure employed by Vallée et al. (2017) by quantitatively evaluating the magnitude of the acausal artifacts. First, we investigated how the input acceleration waveform, having an ideal signal-like shape, was distorted by their procedure. Their acausal deconvolution indeed generated a large-amplitude terminal artifact; however, it was removed by the causal band-pass filtering performed after the deconvolution and consequently became negligible. Next, we constrained the maximum amplitude of the artifact due to the noise in a seismogram and showed that it was sufficiently small compared to the reported signal amplitudes. These results suggest that the signal waveforms seen after their procedure were not artifacts but were representing the input acceleration with sufficient accuracy. Namely, their procedure well functions as a detection method for pre-P gravity signals.

3.2 Introduction

As reviewed in Chapter 1, Vallée et al. (2017) (hereafter referred to as V17) reported the detection of the pre-P gravity signals in the records of broadband seismometers during the 2011 Mw 9.1 Tohoku-Oki earthquake (Figure 1 in V17), and the signals were well simulated by a combination of the pre-P gravity change and ground motion induced by the gravity change in a stratified half-space model, i.e., Model 2' (Figure 2, 3 in V17). However, there was a possibility that the reported signals were not real signals from the earthquake but artifacts of their signal processing. The signal processing procedure in V17 (Proc. V) was as follows (same as mentioned in Appendix A): (i) the seismograms were truncated at the P-wave arrival time, t_{P}; (ii) the mean value was subtracted; (iii) the sensor response was deconvolved by using the "transfer" command of the Seismic Analysis Code (SAC, Goldstein and Snoke 2005); and (iv) a 0.002–0.03-Hz band-pass filter was applied. Step (iii) was acausal because it was calculated in the frequency domain, which generally introduces a ringing artifact at the end of the time series, i.e., prior to t_{P} (e.g. Havskov and Alguacil 2016; Press et al. 1992; Stein and Wysession 2003). Preceding the usage of Proc. V, it should have been confirmed that the acausal effect was negligible and that Proc. V could restore the input acceleration waveform with sufficient accuracy; however, such a confirmation was not fully accomplished in V17. Therefore, it is still unclear whether the reported signals were real or only artifacts. Additionally, the comparison with the synthetic waveforms was also unconvincing because the restoration of the input acceleration waveforms was not guaranteed. Note that step (iv) was causal; V17 used 0.002-Hz two-pole high-pass and 0.03-Hz six-pole low-pass causal Butterworth filters.

In Chapter 2, we resolved this problem and showed a statistically significant signal preceding the P-waves originating from the 2011 Tohoku-Oki event as follows (same as mentioned in Appendix B): while Proc. V suffered from the acausal problem in the deconvolution process, we avoided this and replaced the process with the division of the output of the seismometer by the sensor sensitivity coefficient. This coefficient was defined as the velocity-to-count factor within the frequency band where the instrument response was flat. This process was causal. Moreover, we used the same causal band-pass filter as in Proc. V. Consequently, the entire process of the signal processing procedure of ours (Proc. K) was causal, which enabled us to discuss the presence of the pre-P signals without any influence of the post-P-wave information after time t_{P}.

Here, we solve the question about the signal processing: “does the waveform obtained by applying Proc. V represent the pre-P gravity signal?” (section 3.3). Initially, we show that Proc. V can well restore the ideal acceleration waveform for the case of a transient acceleration input simulating a pre-P gravity signal. The acausal deconvolution process generated a large-amplitude terminal artifact; however, it was effectively removed by the phase delay introduced by applying the causal band-pass filter. Therefore, the waveform obtained by applying Proc. V was nearly equal to the band-pass-filtered input waveform with a small relative error. Furthermore, we evaluate the upper limit of the terminal artifact in the presence of background noise and show that it is smaller than or comparable to the reported signal amplitudes. These results indicate that the acausal effect is practically negligible and Proc. V can reasonably well restore the signal waveforms. Thus, we can regard Proc. V as an acceptable method to explore pre-P gravity signals.

3.3 Verification of the signal processing procedure employed by Vallée et al. (2017)

First, we consider the case where the input acceleration is an ideal signal waveform and see the results of each process of Proc. V. Figure 3.1a is an example of the simulated waveform of a pre-P gravity signal. It increases proportionally to t^5 within certain time limits (here between $t = 0$ and 150 s) assuming that the initial increase of the moment rate is proportional to t^2 (See Section 1.1), and no noise is contained. For this acceleration input, the expected output of a broadband seismometer is displayed in Figure 3.1b. Then, we manually truncated the output at a certain time (here $t = 100$ s when the input acceleration reaches its amplitude of 1 nm/s^2) and deconvolved the sensor response as in step (i) and (ii) of Proc. V (Figure 3.1c). The deconvolved output had a ringing artifact immediately before the end limit, and the amplitude of the artifact was 30 times larger than that of the original input amplitude. Next, we applied the same causal band-pass filter as in step (iii) of Proc. V to both the deconvolved output and original input (Figure 3.1d). The ringing artifact observed in the deconvolved output disappeared following the filtering, and the deconvolved and filtered output well agreed with the filtered input. Their difference was less than 0.1% compared to their amplitudes (Figure 3.1e). This result exhibits that in this ideal case, the waveform obtained by applying Proc. V, i.e., deconvolved and filtered output, well represents the input acceleration in the frequency band. We conducted similar tests using simulation waveforms that increase in proportion to $t^1, t^2, t^3,$ and t^4. As before, the deconvolved and filtered output agreed with the filtered input with an error less than 0.2% (Figure 3.2–3.5). Figure 3.6 and 3.7 show the results for the case of different signal durations. The input acceleration was also restored.

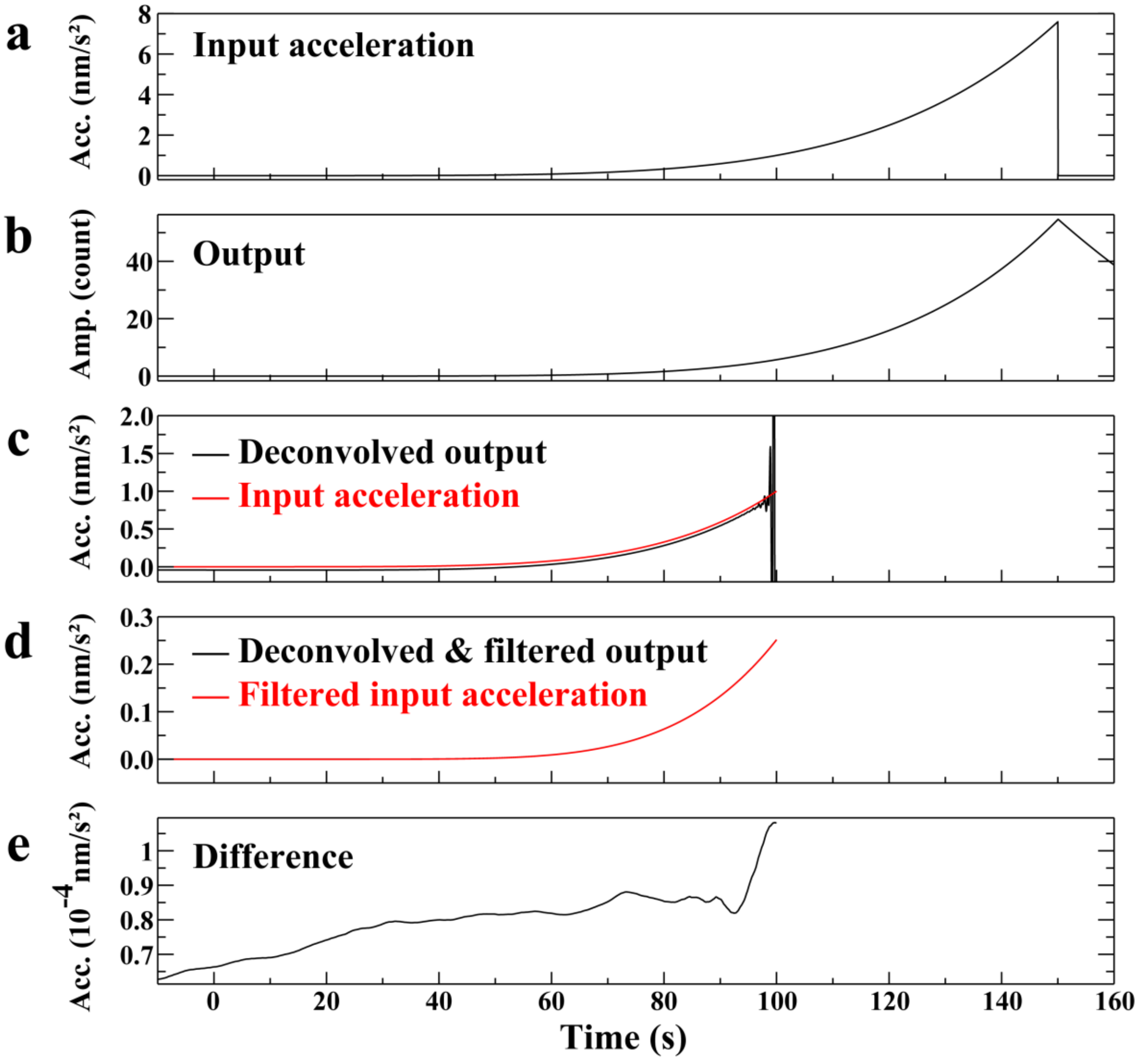

Figure 3.1 Step-by-step results of the signal processing procedure employed by Vallée et al. (2017). "Acc." and "Amp." are the abbreviations of "Acceleration" and "Amplitude", respectively. **a** Input acceleration waveform, which increases in proportion to t^5 for $t = 0–150$ s and is zero before and after the time range. The sampling rate, number of points, and time window are 20 Hz, 72000, and $t = -1800–1800$ s, respectively. **b** Expected output waveform from the broadband seismometer installed at FUK (Fukue). Here, the instrument response of the seismometer was convolved in the frequency domain using the "transfer" command of SAC. **c** Truncated at $t = 100$ s and deconvolved output waveform (black) as well as

truncated input acceleration waveform (red). Here, the deconvolution was performed using the “transfer” command, as before. The offset of the black curve is thought to be due to the zero response at zero frequency. **d** Truncated, deconvolved, and 0.002–0.03-Hz band-pass-filtered output waveform (black) as well as truncated and band-pass-filtered input acceleration waveform (red). **e** Difference between them, i.e., black curve minus red curve in Figure 3.1d.

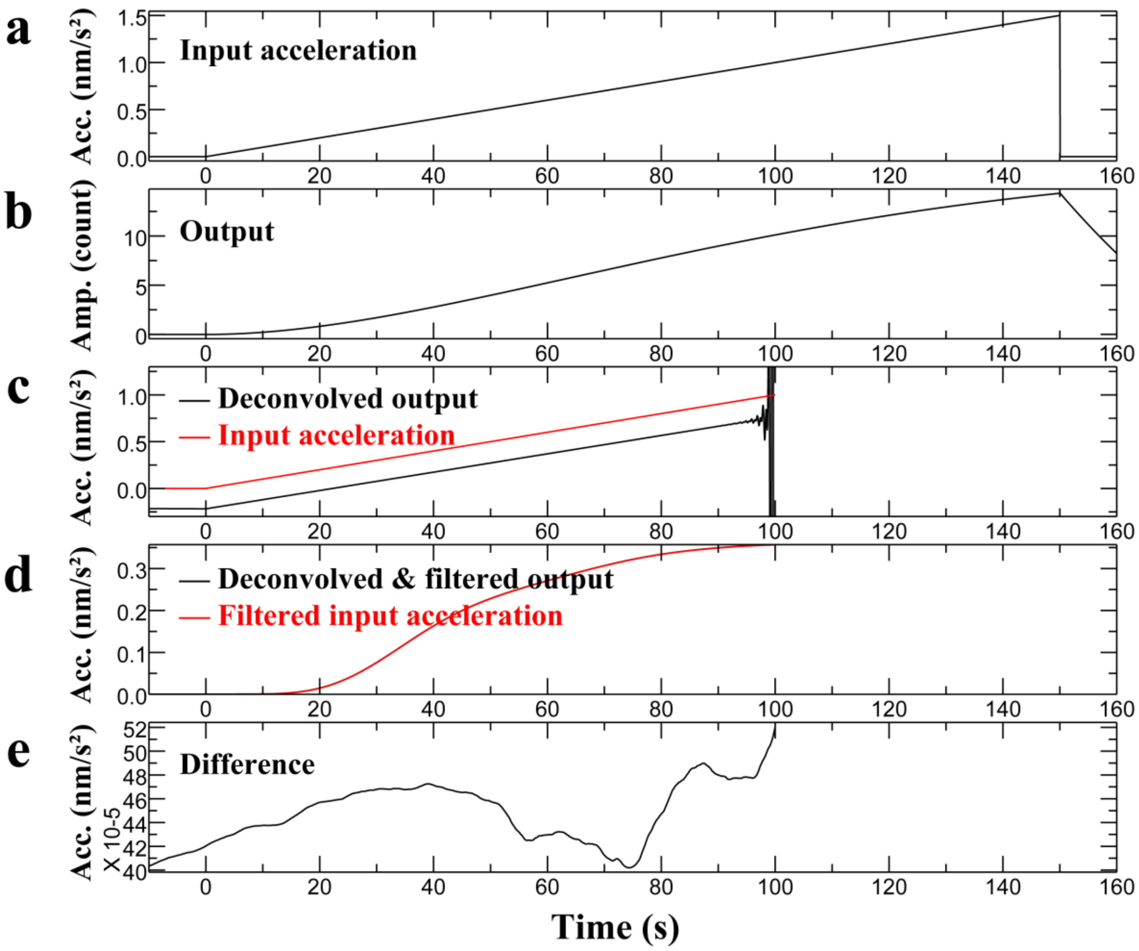

Figure 3.2 For the case of the input which increases in proportion to t^1.

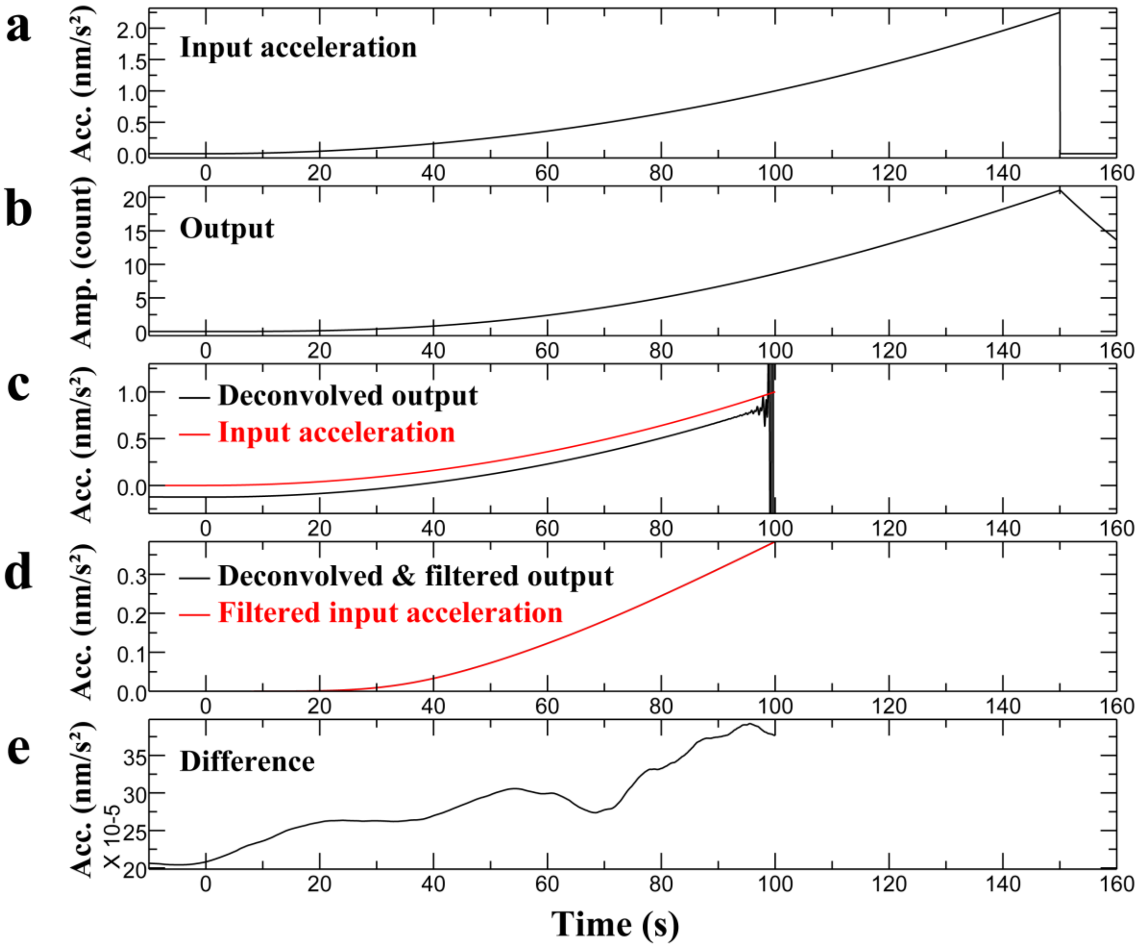

Figure 3.3 For the case of the input which increases in proportion to t^2.

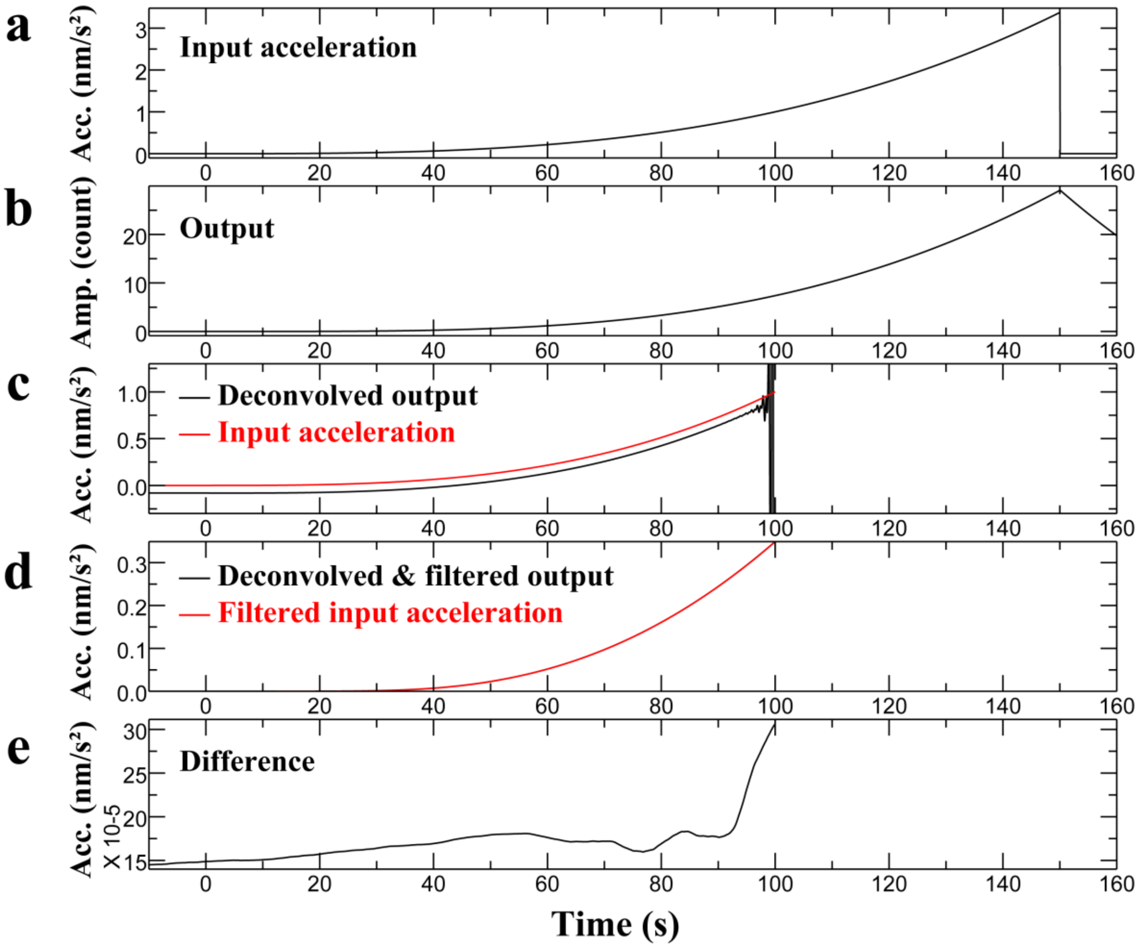

Figure 3.4 For the case of the input which increases in proportion to t^3.

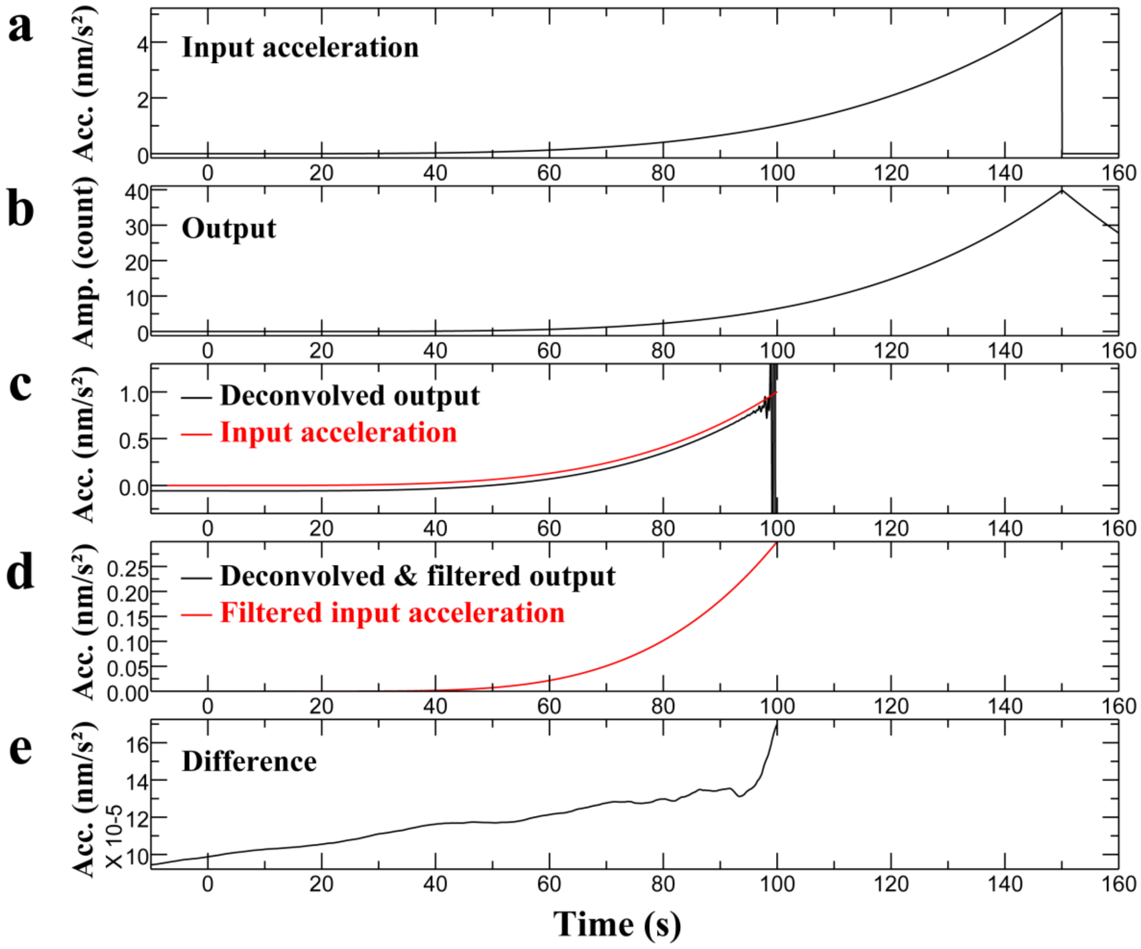

Figure 3.5 For the case of the input which increases in proportion to t^4.

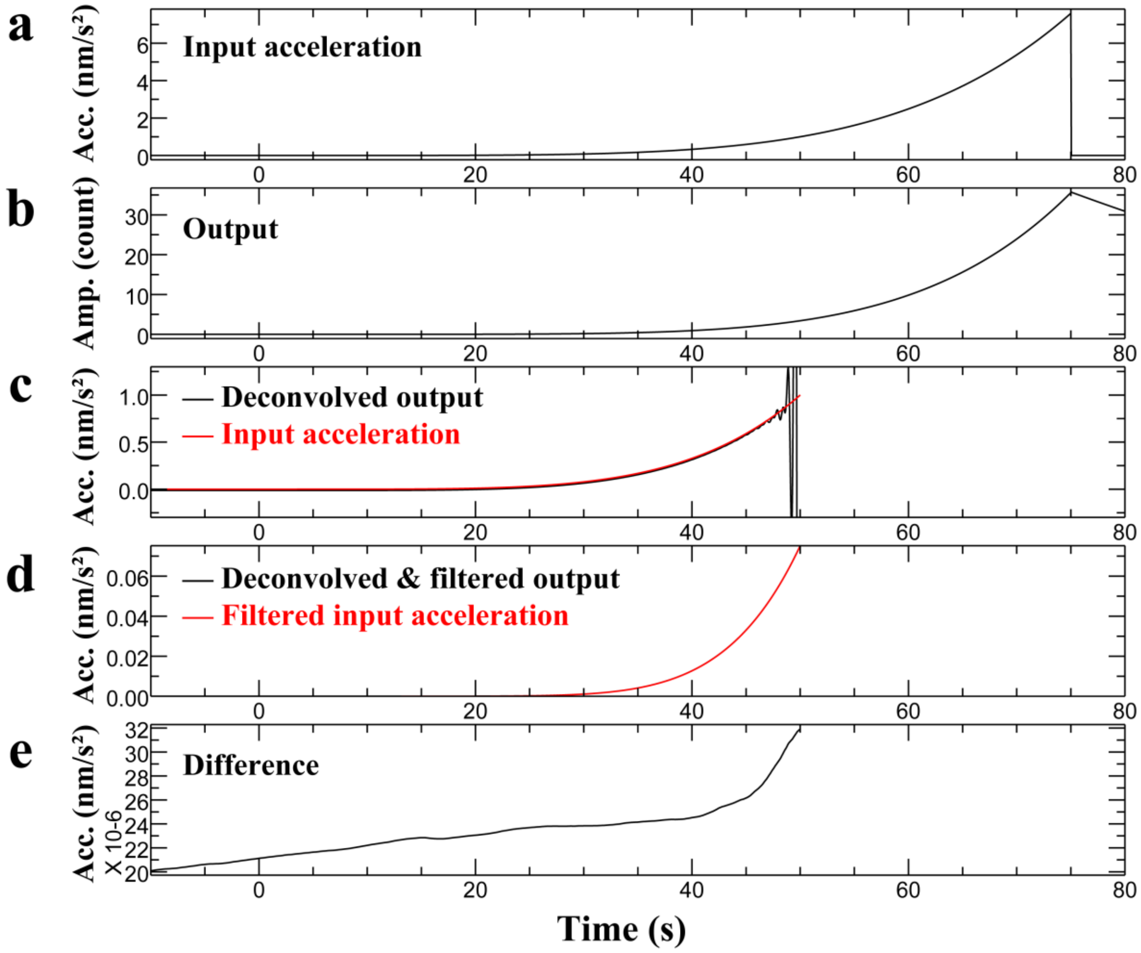

Figure 3.6 For the case of the input which increases in proportion to t^5 between $t = 0 \sim 75$ s. The truncation time is $t = 50$ s.

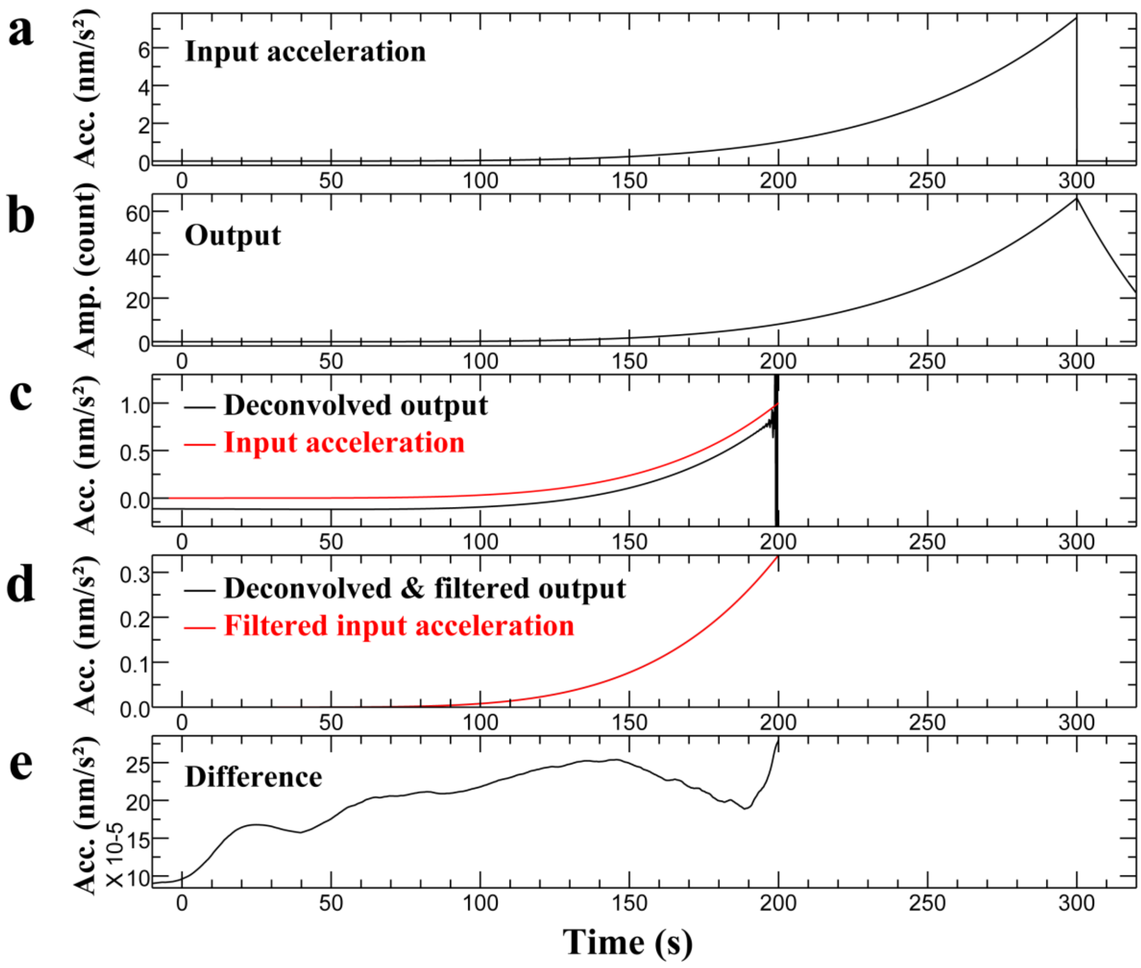

Figure 3.7 For the case of the input which increases in proportion to t^5 between $t = 0 \sim 300$ s. The truncation time is $t = 200$ s.

The disappearance of the ringing artifact following the band-pass filtering is attributed to the phase delay of the employed filters. The causal low-pass and high-pass Butterworth filters used in Proc. V are accompanied by frequency-dependent phase delays. The combined phase-delay time of the two filters is more than 20 s in their pass band of 0.002–0.03 Hz (Figure 3.8). However, the artifacts were limited within 3 s prior to the end of the time window (Figure 3.1c). We can interpret that this time delay pushed out the artifact from the time window, and thus, the artifact seemed to disappear.

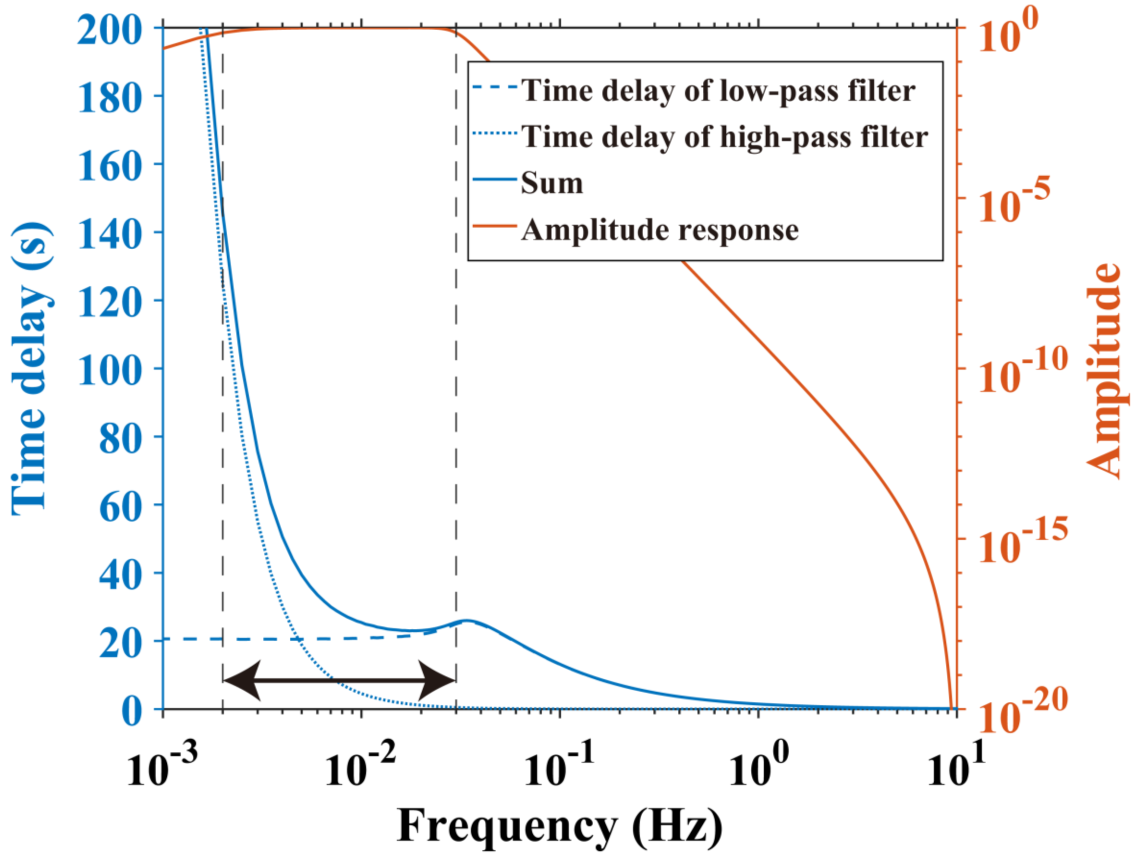

Figure 3.8 Time delay of the six-pole 0.03-Hz low-pass Butterworth filter (dashed blue line), time delay of the two-pole 0.002-Hz high-pass Butterworth filter (dotted blue line), sum of the above two time delays (solid blue line), and amplitude response of the two filters (solid red line). These Butterworth filters were used by V17 and us (Chapter 2). Vertical dashed lines and horizontal arrows indicate the pass band of 0.002–0.03 Hz.

Next, we consider the case where the seismograms contain noise and evaluate the upper limit of the terminal artifacts due to the noise. For this purpose, we first focus on the origin of the ringing artifact, as shown in Figure 3.1c. Because each process of Proc. V is linear, the deconvolution result can be written as a superposition of the results for the impulse time series as follows:

$$\begin{aligned} \boldsymbol{c} &= f(\boldsymbol{b}) \\ &= f\left(\sum_{j=1}^{N} b_j \boldsymbol{\delta}^j\right) \\ &= \sum_{j=1}^{N} b_j f\left(\boldsymbol{\delta}^j\right) \\ &= \sum_{j=1}^{N} b_j \boldsymbol{h}^j \,. \end{aligned}$$

Here, N is the data length, $\boldsymbol{b} = (b_i)_{i=1\sim N}$ denotes the extracted output of the seismometer, $\boldsymbol{c} = (c_i)_{i=1\sim N}$ is the deconvolved output, f is step (ii) and (iii) of Proc. V, i.e., subtracting the mean value and deconvolving the sensor response, $\boldsymbol{\delta}^j = \left(\delta_i^j\right)_{i=1\sim N}$ is a delta-like time series, i.e., $\delta_i^j = 1$ only when $i = j$ and otherwise 0, and $\boldsymbol{h}^j = \left(h_i^j\right)_{i=1\sim N}$ is the impulse response of f for $\boldsymbol{\delta}^j$. While $\boldsymbol{h}^j$ was rich in a short-period oscillation component as shown in Figure 3.9a, the deconvolved output became smooth except the terminal portion (Figure 3.1c). This is because the short-period component of $\boldsymbol{h}^j$ was cancelled by multiplying $\boldsymbol{h}^j$ by a smooth waveform like Figure 3.1b and taking the summation over j. Conversely, we can infer that the ringing artifact emerges at the location where the short-period component is not cancelled. Here, we note that the "transfer" command of SAC pads the data with zeroes to the next power of two ($2^k,\ k \in \mathbb{Z}^+$) to use the fast Fourier transform (Goldstein and Snoke 2005). Namely, extracting an N-long time series ($i = 1{\sim}N$) corresponds to extracting a 2^k-long time series ($i = 1{\sim}2^k$) and replacing the time series of $i = N + 1{\sim}2^k$ with zeroes. Therefore, the terminal ringing artifact as seen in Figure 3.1c is considered to be generated by the absence of the contribution of the following data points: $\sum_{j=N+1}^{2^k} b_j \boldsymbol{h}^j$, which will cancel the artifact if the output is extracted with a length of 2^k and not replaced with zeroes. The artifact owing to the truncation and deconvolution can be evaluated as $-\sum_{j=N+1}^{2^k} b_j \boldsymbol{h}^j$. In addition, the duration of the terminal artifact is expected to be equal to the duration of the impulse response $\boldsymbol{h}^j$ prior to the input impulse (Figure 3.1c, 3.9a).

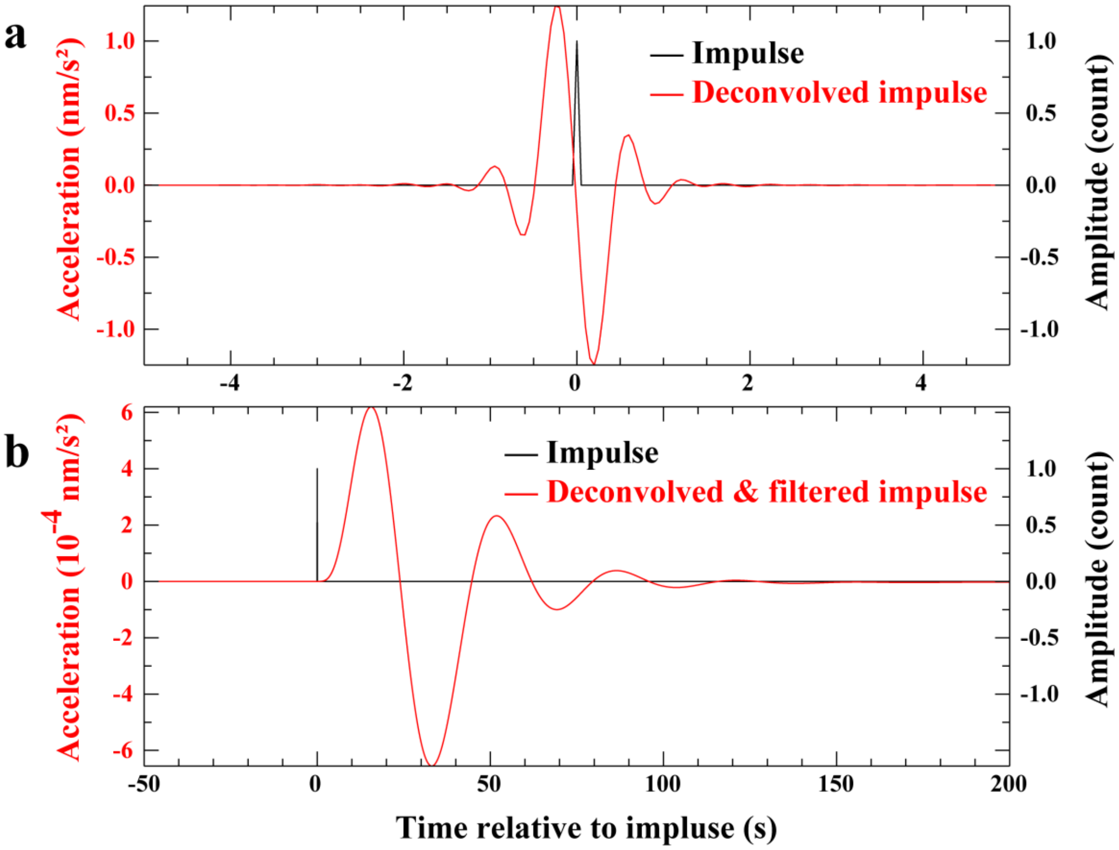

Figure 3.9 An example of the impulse response of Proc. V. **a** Impulsive time series $\boldsymbol{\delta}^j = \left(\delta_i^j\right)_{i=1\sim N}$ (black) and deconvolved impulse $\boldsymbol{h}^j = \left(h_i^j\right)_{i=1\sim N}$ (red). Here, the instrument response of the FUK broadband seismometer was deconvolved using the "transfer" command of SAC. **b** Impulsive time series $\boldsymbol{\delta}^j = \left(\delta_i^j\right)_{i=1\sim N}$ (black) and deconvolved and 0.002–0.03-Hz band-pass-filtered impulse $\boldsymbol{g}^j = \left(g_i^j\right)_{i=1\sim N}$ (red).

This formulation can be directly applicable to estimate the terminal artifact generated by applying entire Proc. V to a seismogram containing noise. In many cases, the dominant noise in the broadband seismograms is microseism noise, and interrupting such a noise waveform at the end limit of the time window can also become a source of an artifact. A possible artifact, $\boldsymbol{s} = (s_i)_{i=1\sim N}$, generated by the entire Proc. V is evaluated as $\boldsymbol{s} = -\sum_{j=N+1}^{2^k} b_j \boldsymbol{g}^j$, where $\boldsymbol{g}^j = \left(g_i^j\right)_{i=1\sim N}$ is the impulse response of f' for $\boldsymbol{\delta}^j$ and f' is step (ii), (iii), and (iv) of Proc. V, i.e., subtracting the mean value, deconvolving the sensor response, and applying the causal low-pass and high-pass filters. Figure 3.9b shows an example of $\boldsymbol{g}^j$. In the presence of noise with a maximum amplitude A, the maximum value of the amplitude of the artifact at the end of the obtained time series, $|s_N|$, is evaluated as follows:

$$\begin{aligned} |s_N| &= \left| -\sum_{j=N+1}^{2^k} b_j g_N^j \right| \\ &\leq \sum_{j=N+1}^{2^k} \left| b_j g_N^j \right| \\ &\leq A \sum_{j=N+1}^{2^k} \left| g_N^j \right|. \end{aligned}$$

For example, the noise level of the Fukue (FUK) STS-1 broadband seismometer data was approximately 2×10^2 counts at the time of the 2011 event occurrence, and $\sum_{j=N+1}^{2^k} \left| g_N^j \right| = 6 \times 10^{-4}$ nm/s^2 for a sufficiently long data length N (here we set $N = 108000$, i.e., 90-min data). Thus, $|s_N|$ was constrained as $|s_N| < 0.1$ nm/s^2. Because the signal amplitude that V17 reported at the station was 1 nm/s^2, which is larger than the calculated maximum $|s_N|$, so the reported signal is not considered as an artifact. The noise level of the Matsushiro (MAJO) STS-2 seismometer data was of the order of 10^4

counts, and $\sum_{j=N+1}^{2^k} \left| g_N^j \right| = 8 \times 10^{-5}$ nm/s^2, so that $|s_N|$ was constrained as $|s_N| < 0.8$ nm/s^2. The reported signal amplitude was approximately 0.7 nm/s^2, which is comparable to the upper limit, but is also sufficiently large not to be considered as an artifact. This is because the upper limit is obtained when the extracted seismogram $b_j = A\ \mathrm{sign}\left(g_N^j\right)$ for all j $(> N)$ and is highly overestimated for actual noise data.

The above results show that Proc. V is a practically valid procedure for detecting pre-P gravity signals. As we saw, the large-amplitude ringing artifacts due to the acausal deconvolution (Figure 3.1c) disappeared following the application of the causal band-pass filter (Figure 3.1d). The comparison of the waveform obtained by applying Proc. V and the filtered acceleration input (Figure 3.1e) showed that Proc. V can acceptably restore the input acceleration from the output of the seismometer for monotonically increasing signal inputs without noise, mimicking the pre-P gravity signals of the 2011 event. Because the obtained waveform closely reproduced the input acceleration, we can compare it to the theoretically predicted waveforms and discuss how well a model can simulate pre-P gravity signals. The causal band-pass filter played a crucial role in Proc. V: it removed the terminal artifacts to the outside of the time window through its phase delay and made Proc. V virtually causal as a whole. We constrained the upper limit of artifacts due to noise, and its amplitude was sufficiently small compared to the reported signal amplitudes. Therefore, the signals reported by V17 are not considered to be acausal artifacts from the truncation and deconvolution.

3.4 Discussion

3.4.1 Waveform distortion due to filtering

The band-pass filtering reduced the signal amplitude to approximately one quarter (Figure 3.1c, d). This reduction rate depends on the signal duration: it was 0.075 when the duration was 50 s and 0.34 for 200 s (Figure 3.6c, d, 3.7c, d). In the case of pre-P gravity signals, the signal duration is proportional to the hypocentral distance. Therefore, the filtered amplitudes vary with the distance even for the same input signal amplitudes. Conversely, the consistent amplitude of approximately 1 nm/s^2 of the signals reported in V17 over a wide region of East Asia does not imply that the input signal amplitudes were the same. It instead suggests that larger amplitudes were input for stations closer to the epicenter. This signal duration effect is attributed to the 20-s phase delay of the causal band-pass filter (Figure 8). For the near stations, the 20-s time shift accounts for a large portion of the signal duration, and therefore, the signal amplitude is considerably reduced, whereas for the far stations, the time shift has a limited role.

The phase delay of the filter helps select appropriate filters for less distorted signal waveforms. The phase delay has to be sufficiently short to ensure that the signals are not pushed out of the time window. Simultaneously, it must be sufficiently long to remove the terminal artifact.

3.4.2 Possible artifacts due to extremely-large-amplitude seismic waves

The validation of Proc. V showed that the band-pass filtering effectively removed the acausal artifacts and made Proc. V practically causal. Given this fact, it may be inferred that the seismograms do not need to be truncated at t_P before the deconvolution and can include the following large-amplitude seismic waves. Figure 3.10 shows the results of Proc. V applied to the seismograms truncated at t_P or containing the seismic waves from the 2011 event. In the latter cases (Figure 3.10b, c, e, f), large-amplitude trends emerged and contaminated the trend clearly seen in Figures 3.10a and d before t_{P}. Though we evaluated above that the artifact due to noise is negligible, it becomes apparent for a large-amplitude waveform (e.g. in the case of Figure 3.10, the amplitude of the seismic waves was more than a thousand times larger than the noise level before deconvolution and band-pass filtering). Therefore, we need to terminate the waveforms prior to the P-wave arrivals when using Proc. V.

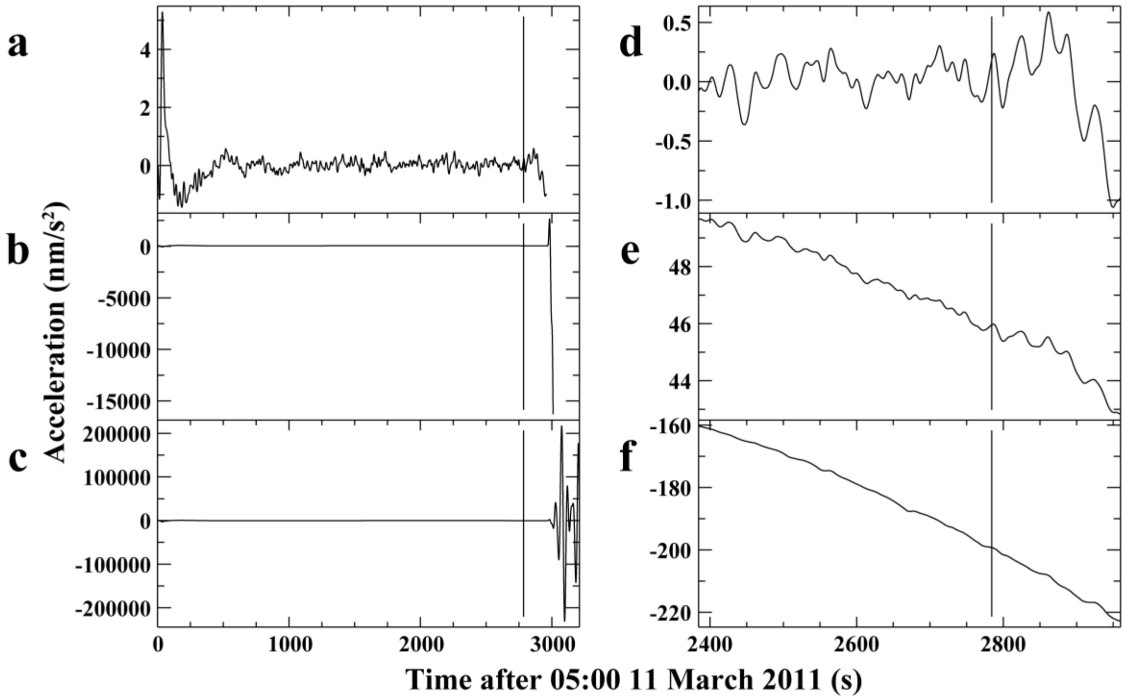

Figure 3.10 Observed acceleration waveforms at FUK at the time of the 2011 Tohoku-Oki event following Proc. V for the cases where **a** the output of the seismometer was truncated at the P-wave arrival time t_{P} prior to the deconvolution, **b** the output was truncated at $t_{\mathrm{P}} + 50$ s, and **c** the output was truncated at $t_{\mathrm{P}} + 250$ s. **d**, **e**, and **f** are the enlarged views between $t_{\mathrm{eq}} - 400$ s (here t_{eq} denotes the event origin time) and t_{P} of **a**, **b**, and **c**, respectively. The vertical lines indicate t_{eq}. The output of the seismometer was not clipped before $t_{\mathrm{P}} + 250$ s.

3.5 Conclusions

By confirming the restoration of the signal waveforms and evaluating the artifacts due to the truncated noise, we verified Proc. V as an appropriate method to search for pre-P gravity signals. We found that Proc. V was practically valid owing to the characteristic phase-delay time of the band-pass filter, which could eliminate the ringing artifacts due to the acausal deconvolution. In this study, we answered the unsolved fundamental problem about signal processing, which is critical for the detection and quantitative treatment of the signal. In the next chapter, we will use this signal processing method and proceed to the waveform inversion analysis.

4. Determination of source parameters of the 2011 Tohoku-Oki earthquake from three-component pre-P gravity signals recorded by dense arrays in Japan

This chapter has not been published in any peer-reviewed journals.

4.1 Summary

The detection of pre-P gravity signals has been limited to the vertical component because of the high noise level in the horizontal records. Here, we analyzed the dense tiltmeter array data in Japan to search for the horizontal components of the signal from the 2011 Mw 9.1 Tohoku-Oki earthquake. Based on synthetic waveforms computed for a realistic Earth model (Model 3), we stacked the horizontal records and identified a signal that clearly exceeded the noise level. We further performed a waveform inversion analysis to estimate the source parameters. The horizontal tiltmeter data, combined with the vertical component of the broadband seismometer array data, yielded a constraint on the dip angle and magnitude of the earthquake in the range of 11.5°–15.3° and 8.75–8.92, respectively. Our results indicate that the analysis of the three components of the pre-P gravity signal avoids the intrinsic trade-off problem between the dip angle and seismic moment in determining the source mechanism of large shallow earthquakes.

4.2 Introduction

To date, the detection of pre-P gravity signals has been reported in several large earthquakes, most notably the 2011 Mw 9.1 Tohoku-Oki earthquake (Montagner et al. 2016; Vallée et al. 2017; Kimura et al. 2019a; Vallée and Juhel 2019). However, the detection has been limited to the vertical component, even though the pre-P gravity signal should be a three-component vector. The horizontal records are generally noisier than the vertical ones due to their higher sensitivity to ground-tilt effects, so the detection of horizontal components of the signal is a current challenge. In Chapter 2, we analyzed the records of the Hi-net tiltmeters, which work as horizontal accelerometers, but failed to detect a signal. This failure may be attributed to the reference model used for the waveform stacking analysis (subsection 2.5.3). We performed the data selection and polarity reversal based on the synthetic amplitudes expected from the simple model of Harms et al. (2015), which simulates only the gravity change $\delta \boldsymbol{g}$ in an infinite homogeneous medium.

In this study, we analyzed the tiltmeter array data to detect the horizontal components of the pre-P gravity signal from the 2011 Tohoku-Oki event. We conducted the waveform stacking analysis based on the simulation results of Model 3. The tiltmeter array data and the vertical component of the F-net broadband seismometer array data were inverted for the point-source parameters. As a result, the dip angle and moment magnitude of the event were well constrained to fit the observed data in both the horizontal and vertical components.

4.3 Data

The March 11, 2011 Mw 9.1 Tohoku-Oki earthquake occurred off the coast of northern Honshu, Japan. We retrieved the two-component borehole tiltmeter records at 689 Hi-net stations and vertical broadband seismometer records at 70 F-net stations (Obara et al.

2005; Aoi et al. 2020). The station locations are indicated in Figure 4.1. The tilt data by National Research Institute for Earth Science and Disaster Resilience (NIED) were in radian and converted into horizontal acceleration in m/s^2 by multiplying with the gravity acceleration (-9.8 m/s^2). The installation orientation of the tiltmeters was corrected at each station according to Shiomi et al. (2003) and Shiomi (2012). Based on the slope in the 30 minutes before the event origin time, the linear trend was removed. The 0.002-Hz two-pole high-pass and 0.05-Hz six-pole low-pass causal Butterworth filters were applied to remove the tidal and microseismic noise. The noise spectrum is shown in Figure 4.2.

The broadband seismometer records were processed with Proc. V: the data were terminated at the visually picked P-wave arrival time $t_{\mathrm{P}}^{\mathrm{obs}}$, deconvolved from the instrumental acceleration response, and the 0.002-Hz two-pole high-pass and 0.03-Hz six-pole low-pass causal Butterworth filters were applied. As we verified in Chapter 3, the acausal artifact due to the frequency-domain deconvolution was removed by the characteristic phase-delay time of the causal filters. Now, Proc. V is widely accepted, and therefore, Proc. V is used here instead of Proc. K which we used in Chapter 2.

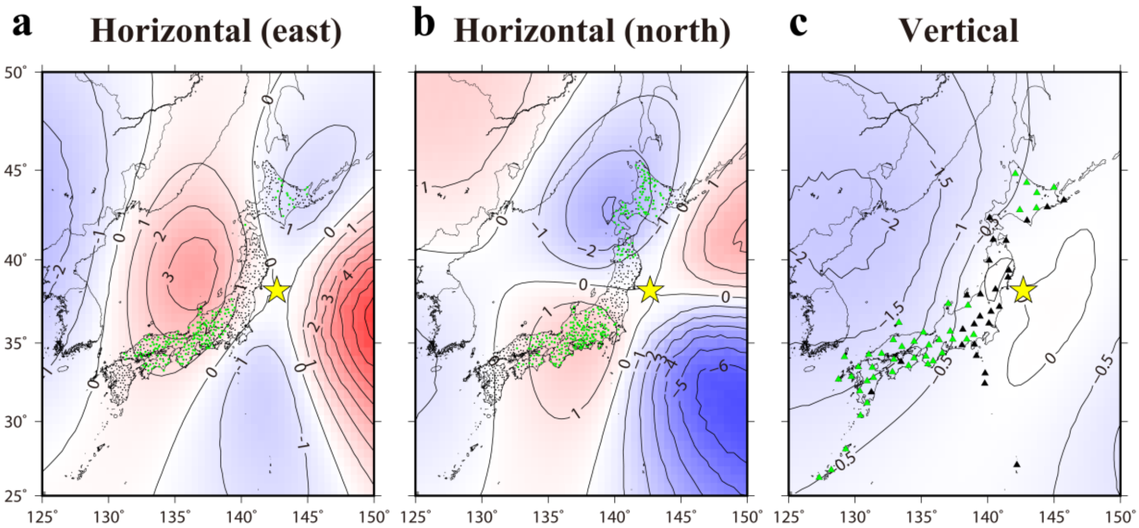

Figure 4.1 Spatial amplitude distribution of the synthesized three-component pre-P gravity signal from the 2011 Tohoku-Oki earthquake at $t = t_\mathrm{P}^\mathrm{theo}$. The simulation method of Zhang et al. (2020) is used, and a GCMT point source is used at the hypocenter. The 2–50 mHz and 2–30 mHz band-pass filter is applied to the horizontal and vertical components, respectively. The contour lines are drawn every 1 nm/s^2 and 0.5 nm/s^2 for the horizontal and vertical components, respectively. The yellow star indicates the epicenter of the event. (a) Horizontal east-west component. The green dots represent the Hi-net stations where the east-west component of the tiltmeter records was used for the stacking, and the black dots represent the others. (b) Horizontal north-south component. The green dots represent the Hi-net stations where the north-south component of the tiltmeter records was used for the stacking, and the black dots represent the others. (c) Vertical up–down component. The green triangles represent the F-net stations where the vertical component of the broadband seismometer records was used for the stacking, and the black triangles represent the others.

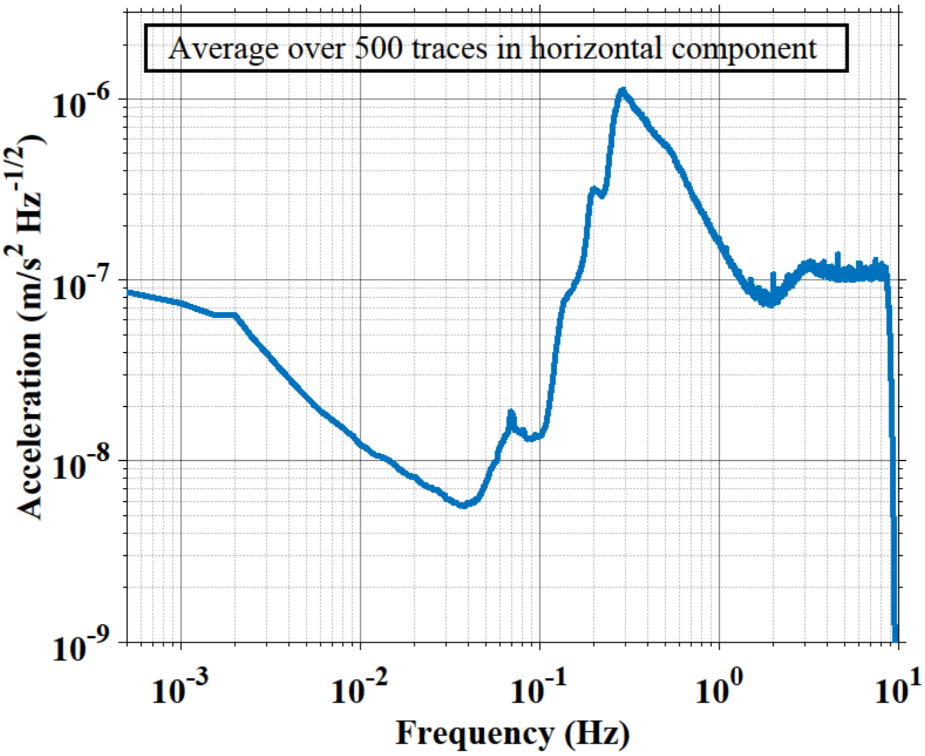

Figure 4.2 Average noise amplitude spectrum of the Hi-net tiltmeter records for 2000 s before the origin time of the 2011 Tohoku-Oki earthquake. From the 1378 records (two-components at 689 stations), the 500 records with a small standard deviation in the 2000 s time window were selected, and their spectra were averaged. The instrument response is included.

4.4 Methods

4.4.1 Waveform simulation

We used the approach developed by Zhang et al. (2020), i.e., Model 3, to synthesize the pre-P gravity signal waveforms (see Section 1.1 for more detail). The pre-P gravity signal measured by ground-based sensors is synthesized as $s_x = \ddot{u}_x - \delta g_x - g\frac{\partial u_z}{\partial x}$, $s_y = \ddot{u}_y - \delta g_y - g\frac{\partial u_z}{\partial y}$, and $s_z = \ddot{u}_z - \delta g_z + u_z\frac{\partial g}{\partial z}$ (Dahlen and Tromp, 1998), but we ignored the tilt term $-g\frac{\partial u_z}{\partial x}, -g\frac{\partial u_z}{\partial y}$ for horizontal components s_x, s_y and free-air term $u_z\frac{dg}{dz}$ for vertical one s_z because of their small contributions to the signal amplitudes (Juhel et al. 2019; Zhang et al. 2020). Here, $x, y,$ and z axes are taken eastward, northward, and upward positive, respectively.

In subsection 4.5.1, a point source is adopted for the waveform simulation from the 2011 Tohoku-Oki earthquake and located at the hypocenter (latitude, longitude, depth) = (38.19°N, 142.68°E, 21 km) determined by Chu et al. (2011). The event origin time t_{eq}, seismic moment M_0, rupture duration T, and source mechanism (strike, dip, rake) are set to 05:46:23 UTC, 5.31×10^{22} Nm, 140 s, and (203°, 10°, 88°), respectively (Global Centroid Moment Tensor: GCMT, Ekström et al. 2012). The moment rate function $\dot{M}(t)$ is described as a squared half-period sinusoidal function:

$$\dot{M}(t) = M_0\frac{2}{T}\sin^2\left(\pi\frac{t}{T}\right) \quad (0 \le t \le T). \tag{4.1}$$

The modified Earth structure model based on AK135 by Wei et al. (2012) was used. The Green functions were calculated up to 0.25 Hz. The synthesized signal waveforms were truncated at the P-wave arrival time t_{P}. Here, t_{P} is the lesser of the visually picked value $t_{\mathrm{P}}^{\mathrm{obs}}$ and $t_{\mathrm{P}}^{\mathrm{theo}}$ (2 s before the theoretical value calculated by the TauP toolkit, Crotwell et al. 1999). In subsection 4.5.2, the dip angle and M_0 are model parameters, and the rupture duration T is assumed to obey the scaling law (Kanamori and Anderson, 1975).

4.4.2 Point source correction

The pre-P gravity signals calculated for the adopted point source tend to be larger than those calculated for a finite fault model with the same total seismic moment (Zhang et al. 2020). Figure 4.3 shows that this overestimation is particularly pronounced in the horizontal component, which will affect the inversion results. To evaluate more acceptable signal amplitudes, in subsection 4.5.2 we employed a constant factor (estimated roughly to be 0.75 from Figure 4.3) and multiplied the synthesized waveforms in the horizontal components by the factor.

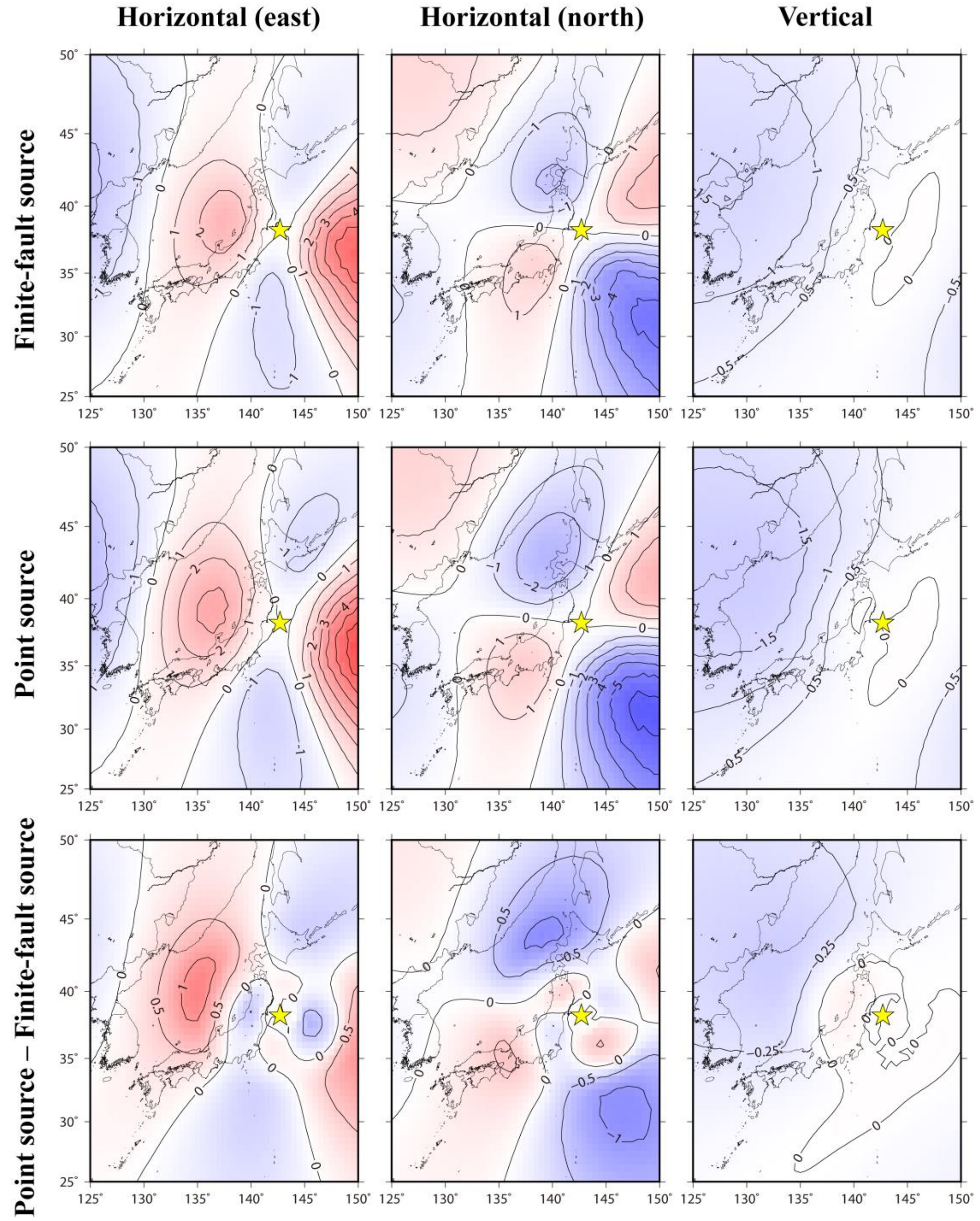
Horizontal (east)
Horizontal (north)
Vertical
Finite-fault source
Point source
Point source – Finite-fault source
50°
45°
40°
35°
30°
25°
125°
130°
135°
140°
145°
150°

Figure 4.3 Comparison of the magnitude maps of the three-component pre-P gravity signal from the 2011 Tohoku-Oki earthquake obtained from the finite-fault and point-source models. The finite fault is adopted from Wei et al. (2012), while the point source is located at the hypocenter (latitude/longitude/depth =38.23°N/142.70°E/21 km) and has the same seismic moment as the entire finite fault model. The horizontal and

vertical synthetics are band-pass filtered between 2–50 mHz and 2–30 mHz, respectively.

4.4.3 Waveform stacking

The amplitude of the pre-P gravity signal is comparable to or smaller than the background noise level (Montagner et al. 2016; Kimura et al. 2019a; Vallée and Juhel 2019), so it is difficult to identify the signal in a single trace. To reduce noise and enhance the signal, we take the waveform stacking approach (Kimura et al. 2019a; Vallée and Juhel 2019). Because the amplitude of the pre-P gravity signal is in many cases expected to monotonically increase in time until the P-wave arrival, the waveforms are aligned and stacked with t_P as

$$\overline{a}(t) = \frac{1}{N}\sum_{i=1}^{N} \mathrm{sgn}\left(s^i\left(t_\mathrm{P}^i\right)\right) a^i\left(t_\mathrm{P}^i + t\right) \quad (t \leq 0), \tag{4.2}$$

where $s^i(t)$, $a^i(t)$, and t_P^i are the synthetic acceleration, observed acceleration, and P-wave arrival time at the i-th sensor, respectively, $\overline{a}(t)$ is the stacked trace, N is the total number of the stacked sensors, and $\mathrm{sgn}(*)$ is the sign function for polarization reversal. By replacing $a^i(t)$ with $s^i(t)$, the synthetic waveforms can also be stacked.

4.4.4 Inversion method

For the waveform inversion, we used the misfit function defined as

$$R(p) = \frac{1}{\alpha}\sum_{i=1}^{N} \frac{1}{{\sigma^i}^2} \int_{t_1^i}^{t_2^i} \left|a^i(t) - s^i(t;p)\right|^2 dt, \tag{4.3}$$

where p is the variable parameters to be estimated, σ^i is the standard deviation of $a^i(t)$ before t_{eq} (here we took the time window $\left[t_{\mathrm{eq}} - 10\ \mathrm{min}, t_{\mathrm{eq}}\right]$), and $s^i(t;p)$ is $s^i(t)$ calculated using parameter values of p. For the same reason that the stacking was done aligned with t_{P}, we set the time window to be fitted as $t_2^i = t_{\mathrm{P}}^i$ and $t_1^i = t_{\mathrm{P}}^i - \frac{1}{4}\left(t_{\mathrm{P}}^i - t_{\mathrm{eq}}\right)$. We took the normalization constant as $\alpha = \sum_{i=1}^{N} \int_{t_1^i}^{t_2^i} dt$ so that $R(p)$ becomes 1 if the noise level is time invariant and the signal is completely removed from the observed data with parameter values of p.

4.5 Results

4.5.1 Detection of the horizontal component of the pre-P gravity signal

The horizontal component of the pre-P gravity signal from the 2011 Tohoku-Oki earthquake is expected to have an amplitude of approximately 1–2 nm/s^2 over the Japanese land area in the range of 0.002–0.05 Hz (Figure 4.1a, b). Based on this synthetic amplitude, the tiltmeter data were stacked (equation 4.2). From the 1378 records (two components at 689 stations), 429 records with the ratio of the synthetic amplitude to the noise level greater than 0.7 were selected and stacked. Noisy records whose maximum amplitude in the 30 minutes before t_{eq} was greater than 10 nm/s^2 were excluded. The locations of the selected stations are shown in Figure 4.1a, b.

As a result of the stacking, a clear signal above the noise level was seen before the P-wave arrival (Figure 4.4a). The signal amplitude was 0.64 nm/s^2, which was 9.5 times higher than the reduced noise level of 0.067 nm/s^2. The positive change of the stacked trace indicates that the polarity of the detected pre-P signal is the same as the prediction of the reference model, i.e., Model 3.

In addition, the radiation pattern in the north-south component was confirmed: the north-south component records were stacked in the positive and negative synthetic value regions, respectively, and in both cases, signals with the same sign as synthesized were found to exceed the noise level (Figure 4.5). The trace in Figure 4.4a is a weighted average of the trace in Figure 4.5a and the polarity-reversed trace in Figure 4.5b.

However, the amplitude of the detected signal was less than half of that of the stacked synthetic waveforms of 1.65 nm/s^2, and their difference of approximately 1 nm/s^2 was out of the noise level. This result is in contrast to that for the vertical records (Figure 4.4b). Here, from the 70 broadband seismometer records, 43 records with the ratio of the synthetic amplitude shown in Figure 4.1c to the noise level greater than unity were selected and stacked. The stacked synthetic amplitude of 0.75 nm/s^2 was near to the signal amplitude of 0.68 nm/s^2, and the difference was within the range of the noise level of 0.05 nm/s^2.

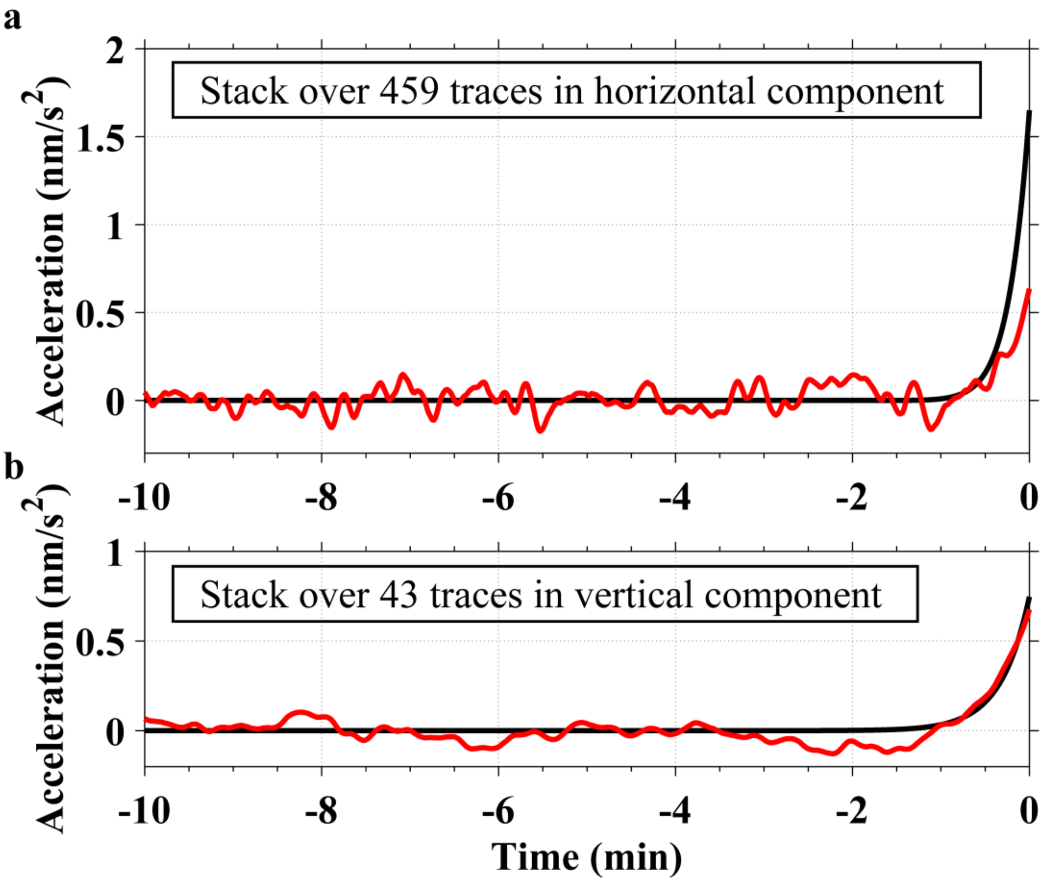

Figure 4.4 Stacked waveforms of observed data (red) and synthetics (black). The time 0 is set to the stacking reference time t_{P}. The synthetics are for the GCMT point source. (a) Horizontal component in the frequency band of 0.002–0.05 Hz. (b) Vertical component in the frequency band of 0.002–0.03 Hz.

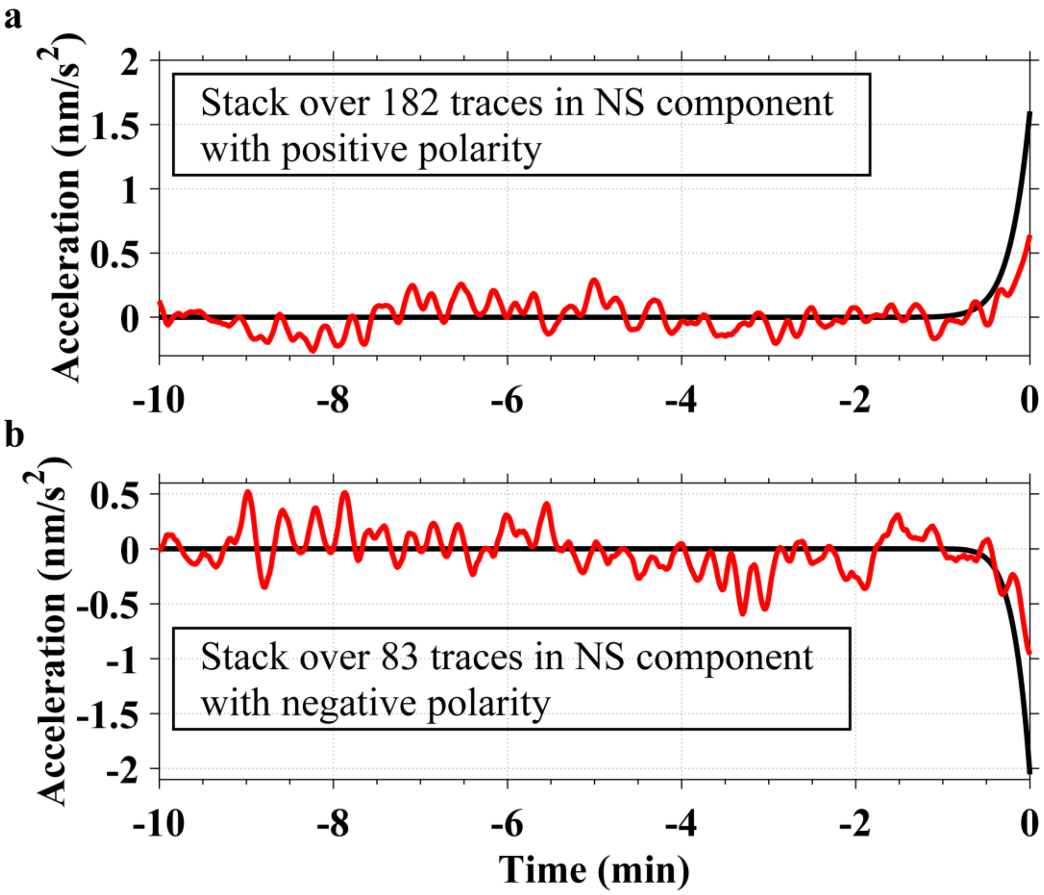

Figure 4.5 Stacked waveforms of the horizontal north-south component data (red) and synthetics (black) in the frequency band of 0.002–0.05 Hz. The time 0 is set to the stacking reference time t_{P}. (a) Only the stations where positive synthetic amplitudes are expected were used (green stations with positive values in Figure 4.1b). (b) Only the stations where negative synthetic amplitudes are expected were used (green stations with negative values in Figure 4.1b).

4.5.2 Waveform inversion

Here, we performed a waveform inversion analysis to resolve the synthesis–observation inconsistency revealed in the previous subsection and to estimate the source parameters that better fit the observations. Figure 4.6 shows the distribution of the misfit function for the dip angles and Mw in the range of 5–25° and 8.4–9.3, respectively. The tendencies are different between the horizontal and vertical components: the misfit function for the horizontal components is sensitive to the dip angle, while that for the vertical component shows a negative correlation between the dip angle and Mw. Sum of the misfit functions for the three components took its minimum at the dip angle of 13° and Mw 8.85 (Figure 4.6c). Then we calculated the estimation errors by the bootstrap method (Rubin, 1981). The mean value and 90% confidence interval of the dip angle and Mw to minimize the misfit function were 13.2° and [11.5°, 15.3°], and 8.85 and [8.75, 8.92], respectively. Here, 689 stations were randomly selected from the 689 Hi-net tiltmeter stations, and 70 stations were selected from the 70 F-net broadband seismometer stations, both allowing duplicates. The calculation of the misfit functions was repeated 500 times. Figure 4.7 shows the resultant stacking traces of observations and model predictions for the improved parameters (dip angle 13°, Mw 8.85). The synthetic and observed waveforms showed a quantitative agreement with each other within the uncertainty of background noise.

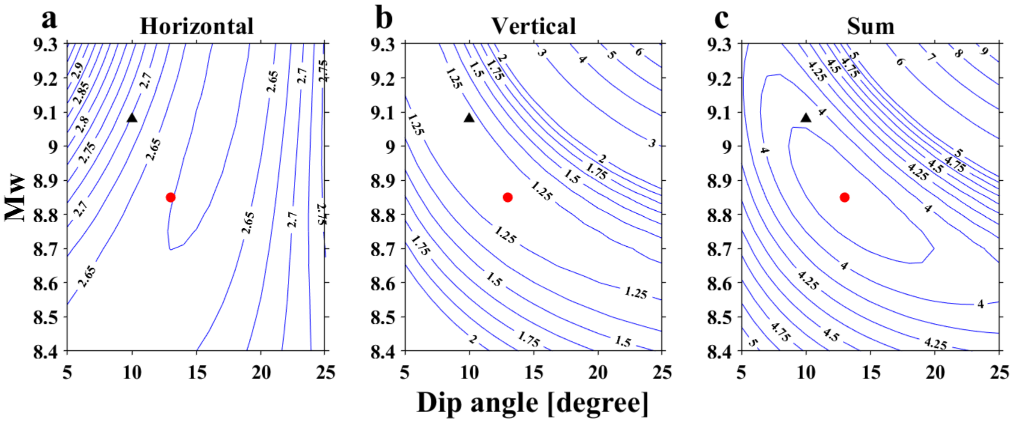

Figure 4.6 Distribution of the misfit function between the synthetics and observed data. The red dot and black triangle indicate the point (dip angle, Mw) = (13°, 8.85) and the GCMT solution (10°, 9.08), respectively. (a) The misfit function for the horizontal records, i.e., the sum of the misfit function for the east-west component tiltmeter records and that for the north-south component. (b) The misfit function for the vertical broadband seismometer records. (c) The misfit function for the three-component data, i.e., sum of (a) and (b).

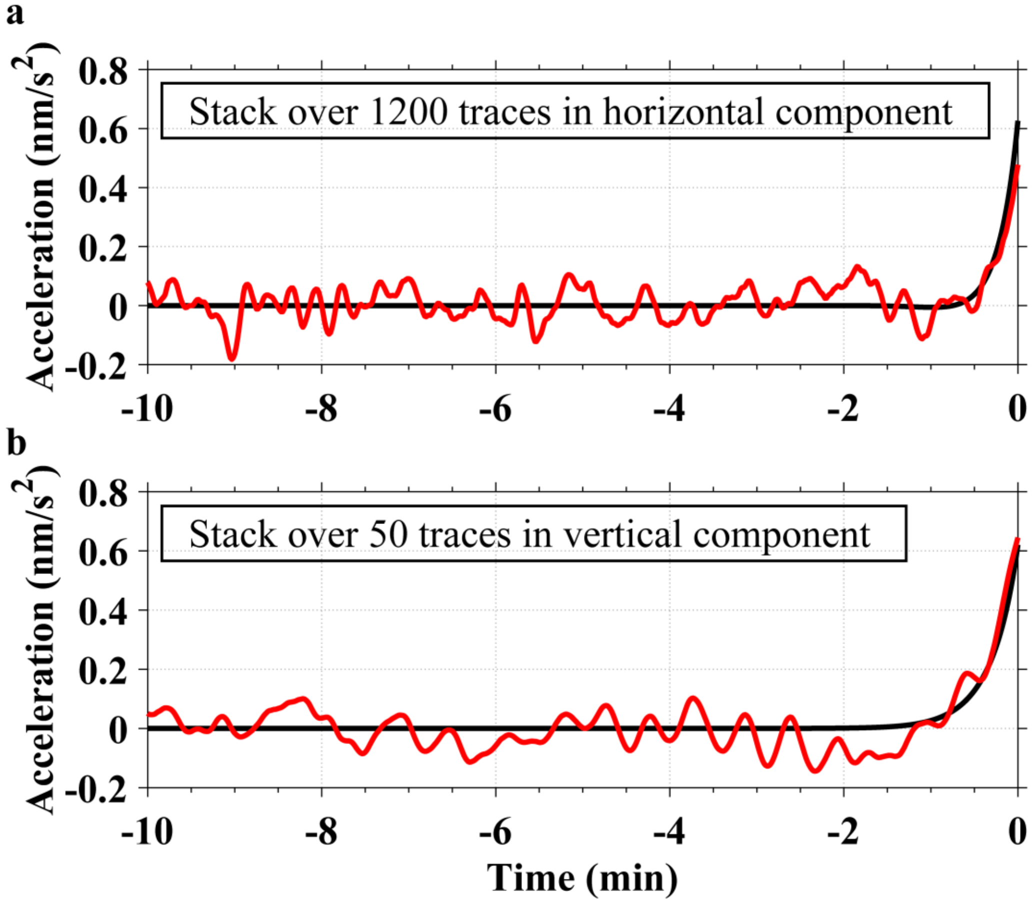

Figure 4.7 Stacked waveforms of observed data (red) and synthetics (black). The time 0 is set to the stacking reference time t_P. The synthetics are for the GCMT point source, but the dip angle and Mw are set to 13° and Mw 8.85, respectively. (a) Horizontal component in the frequency band of 0.002–0.05 Hz. The amplitude of the stacked synthetic waveforms includes the point source correction. (b) Vertical component in the frequency band of 0.002–0.03 Hz.

4.6 Discussion

4.6.1 Why the dip angle can be determined from the pre-P gravity signal

It is well known that the long-period seismic waves have poor sensitivity to the seismic moment M_0 and dip angle δ and cannot well constrain them for large shallow dip-slip events (Kanamori and Given 1981). This is because all the excitation terms of the normal modes become proportional to $M_0 \sin 2\delta$ to satisfy the traction-free boundary condition at the surface when the source depth becomes zero and cannot divide the term into M_0 and δ (Tsai et al. 2011).

On the other hand, our analysis clearly shows that the horizontal and vertical components of the pre-P gravity signal have different dependencies on δ so that M_0 and δ were well constrained. However, the reason why they have different dependencies is not clear. Because the excitation terms are common among the elastic deformation and gravity change, it seems impossible to avoid the trade-off between M_0 and δ, even if we observe the gravity change. It may be possible to think that the pre-P gravity signal has greater sensitivity to short-wavelength seismic waves because the gravity change is caused by the density perturbation $\delta\rho$ (basically this is the divergence of $\boldsymbol{u}$, which would enhance the contribution of short-wavelength waves). However, this hypothesis does not account for the difference of the dependencies on δ between the horizontal and vertical components.

The estimated dip angle of 13.2° was a relatively large value, which may reflect the characteristics of the fault rupture of the earthquake that short-period and short-wavelength seismic waves were radiated from the deeper region of the fault. This is consistent with the results of seismic inversion analyses (e.g., Ide et al. 2011; Lay et al. 2011). Alternatively, it may also be related to the temporal properties of the pre-P gravity signal. Considering that this signal rapidly increases its amplitude just before the arrival of the P-wave, it is thought that this signal does not tell us the complete average of the moment release, but rather emphasizes the rupture in the region closer to the observation station. This is because we can analyze only the signal before the arrival of any P-wave, which readily masks this tiny signal. In other words, even if a large slip occurs in a region farther than the hypocenter from the observation station, the signal from the large slip will still have only a small amplitude when the P-wave from the hypocenter reaches the observation station, and therefore its contribution to the overall signal amplitude will be small. In the case of the 2011 Tohoku-Oki event, observations of the pre-P gravity signal on the land of Japan are thought to be heavily influenced by the rupture of west-side and deeper regions of the fault, while that of east-side and shallower regions would have only a limited effect.

The estimated moment magnitude Mw was slightly smaller than the values that have been estimated seismologically (9.0–9.1). Given that the fault rupture is not yet finished by the P-wave arrival time in most of the Japanese data used, this suggests that the total released moment of the earthquake is greater than expected from the beginning phase of the rupture that was captured by the pre-P gravity signal in the data used.

In this study, we used the point source approximation to estimate the basic features of the fault rupture. Future inversion analyses, including the finiteness of the fault, will further clarify the spatio-temporal characteristics of the source process.

4.6.2 Proposal of pre-P gravity seismology with the use of signals combined with theoretical models

Since Harms et al. (2015) presented the first quantitative model, the interest in pre-P gravity signals has increased in terms of both theoretical modeling and observation. However, most observational studies are limited to the detection of the presence of signals. In this study, we showed that the pre-P gravity signal can be used in a quantitative and useful way using the information about the three-component signal waveforms. This result means that it is possible to perform a quantitative analysis about the earthquake occurrence by combining the new observation window of the pre-P gravity signal with its quantitative model.

As reviewed in Section 1.1, theoretical models have been developed so far and become able to synthesize the signals for a realistic Earth structure considering both pre-P gravity change and pre-P ground acceleration and solving the fully coupled elasto-gravity equations. A possible challenge for future observational research is the observation of pre-P gravity potential. The gravity potential is expected to be a new observable that can be measured by the optical lattice clock (Ushijima et al. 2015). Figure 4.8 shows the waveform and amplitude distribution map of the pre-P gravity potential from the 2011 event. The expected potential change is in the order of 10^{-3} m^2/s^2, which is equivalent to the height difference of 0.1 mm on the surface of the Earth and frequency difference of 10^{-20} between two clocks. This change is 10^{-2} times smaller than the current accuracy of the instrument, i.e., 10^{-18} (Takamoto et al. 2020).

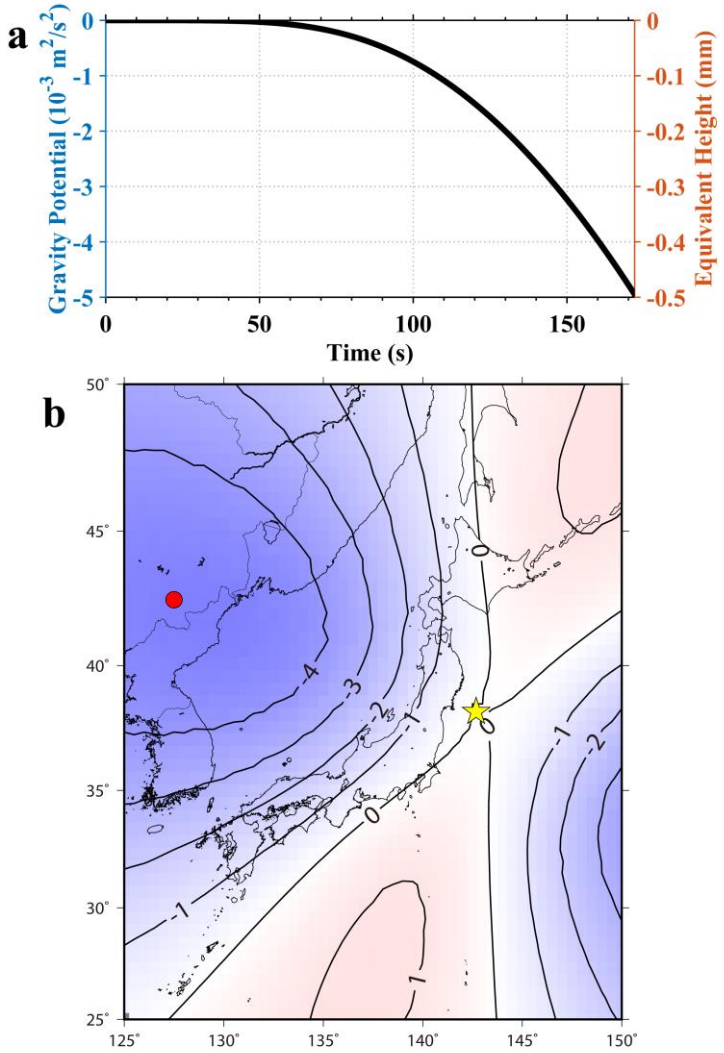

Figure 4.8 Synthesized pre-P gravity potential from the 2011 Tohoku-Oki earthquake. (a) A representative potential waveform at a hypothetical observation station (latitude = 42.5°N, longitude = 127.5°E). The simulation method of Zhang et al. (2020) is used. The synthetics are for the GCMT point source, but the dip angle and Mw are set to 13.2° and Mw 8.85, respectively. The 150-mHz six-pole low-pass causal Butterworth filter is applied. (b) Spatial amplitude distribution of the pre-P gravity potential. The contour lines are drawn every 10^{-3} m^2/s^2. The yellow star and red circle indicate the epicenter of the event and hypothetical observation station, respectively.

4.7 Conclusions

By using the synthetic waveforms calculated by the method of Zhang et al. (2020) as a reference, we detected the horizontal components of the pre-P gravity signal from the 2011 Tohoku-Oki earthquake in tiltmeter array data with the signal-to-noise ratio of 9.5. The discrepancy in amplitude between the signal and stacked synthetic waveforms was resolved by changing the dip angle and Mw of the source, and the waveform inversion for the three-component records constrained these parameters in the range of 11.5°–15.3° and 8.75–8.92, respectively.

Our detection and quantification of the pre-P gravity signal combined with the simulation results of Zhang et al. (2020) show that this signal opens a new observation window for the earthquake source independently from seismic observation. For a future challenge of new observation study, we synthesized the pre-P gravity potential, which may be able to be measured by future optical lattice clock.

5. General conclusions

In Chapter 2 and 3, we prepared for quantitative treatment of pre-P gravity signal waveforms and comparison between observation and theoretical modeling through the definite signal detection and the validation of the signal processing method. In Chapter 2, we searched for pre-P gravity signals from the 2011 Mw 9.1 Tohoku-Oki earthquake in seismic network data. Though nearly all the single-channel waveforms did not show any signals beyond the noise level, the stacked trace of F-net broadband records showed a clear signal in the vertical component. The identified signal level was 0.25 nm/s^2, and the detection was verified with a statistical significance of 7σ. In Chapter 3, we verified the signal processing procedure employed by Vallée et al. (2017) as an appropriate method to search for pre-P gravity signals. We found that the procedure was practically valid owing to the characteristic phase-delay time of the band-pass filter, which could eliminate the ringing artifacts due to the acausal deconvolution.

Chapter 4 is the most important part in this thesis. We used the synthetic waveforms calculated for a realistic Earth model (Zhang et al. 2020) and conducted a waveform inversion analysis to estimate the source parameters of the 2011 event. The inversion resulted in the successful constraint on the dip angle, which had been difficult to determine from long-period seismic data.

From this finding, we showed that the observation of the pre-P gravity signal can provide a new insight into earthquakes and complement the long-period seismic observation. We can propose that the usage of the three-component signal waveforms was essential for providing the new constraint on the source parameters.

Appendix A. Data processing and station selection criteria of Vallee et al. (2017) and characteristics of the waveforms presented in the study

Vallée et al. (2017) retrieved all the regional broadband vertical seismic records at distances up to 3000 km from the 2011 Tohoku-Oki earthquake hypocenter from the Incorporated Research Institutions for Seismology (IRIS) data center and from F-net. The number of stations was approximately 200 in this region, many of which were deployed in Japan and northeast China. They conducted signal processing (Proc. V) as follows: they (i) terminated each station time series at the P-wave arrival time; (ii) removed the mean value; (iii) deconvolved the sensor response and converted it into a band-limited accelerogram using the Seismic Analysis Code (SAC, Goldstein and Snoke 2005) command “transfer”; and then (iv) applied a band-pass filter (0.002-Hz two-pole high-pass and 0.03-Hz six-pole low-pass causal Butterworth filters). During Proc. V, no tapering was applied to the records.

Among all the processed records, they selected nine records based on a noise criterion that the waveform amplitude never exceeded ±0.8 nm/s^2 during the 30-min window before the earthquake origin time. They additionally selected two F-net stations (Shari, Fukue) to improve the azimuthal and distance coverage. The hypocentral distances of the selected 11 stations ranged from 427 to 3044 km.

Nine waveforms out of the 11, three in the Japanese islands and six in the Asian continent, shared a downward trend beyond the seismic noise before the P-wave arrivals. The amplitudes immediately prior to the P-wave arrivals were approximately 1 nm/s^2

for the hypocentral distance 1000–2000 km (Figure 1 of Vallée et al. 2017), in which Vallée et al. considered the observability of the signals reaches a maximum.

Appendix B. Data processing of the study in Chapter 2 and the difference from Vallée et al.'s procedures

The data processing in Chapter 2 for vertical broadband data (Proc. K) is as follows: we (i) extracted the 60-min time series data starting at 46 min before the origin time; (ii) calibrated the raw digital count data into velocity by dividing by the sensor sensitivity coefficient; (iii) converted it from velocity to acceleration through the finite difference of digital velocity data; (iv) multiplied a cosine taper at the first and last 10% sections of the time series; and then (v) applied the same band-pass filter employed in Proc. V. The 60-min time series are sufficiently long to avoid the taper to decrease the signal of interest.

Proc. K does not involve the recovery of the instrumental response and therefore is perfectly causal. Though we used data containing the following large amplitude of the P-waves, non-causal artifacts never originated from the section. In contrast, as mentioned in Appendix A, Vallée et al. (2017) terminated the waveforms at the P-wave arrival time and deconvolved the sensor response. Removal of the instrumental response from the terminal portion of time series data works as an acausal filter for the waveform, which can generate artifacts just before P-wave arrival.

Note that most of the available data were clipped after the P-wave arrivals. That is why both Vallée et al. (2017) and we did not deconvolve the sensor response from the time series including the P-wave section.

Appendix C. Station selection criterion and polarity reversal correction for stacking of F-net and Hi-net data in Chapter 2

For the stacking of F-net data, we selected 27 stations where the noise level A_{N} was less than one-twentieth of the reference value A_{S}. Here, A_{S} is the amplitude of the synthetic waveforms predicted by Harms et al. (2015) and applied the same filter as for the observed waveforms. As an example, the filtering decreases the amplitude of the pre-P gravity change at Kamioka (Figure 1.1a) from −23 nm/s^2 to −5 nm/s^2 (Kimura 2018). Our selection criterion based on the model of Harms et al. (2015) eventually corresponded to the station selection with very low noise level and a hypocentral distance longer than 500 km.

For these 27 records, we applied a polarity reversal correction, i.e., the data was multiplied by -1 at stations where the predicted gravity change $(\delta \boldsymbol{g}^{\mathrm{H}})_z$ is positive, and vice versa, based on the model by Harms et al. (2015) (Figure 1.1b). The predicted polarities at the 27 stations were the same (Table 2.2); we just added them to obtain the stacked waveform.

For the stacking of Hi-net data, the trace selection criterion and a polarity reversal correction were based on Harms et al. (2015) as well. Because of the noisy data, traces were chosen based on the criterion of the $A_{\mathrm{S}}/A_{\mathrm{N}}$ ratio being greater than unity. Note that the model of Harms et al. (2015) can provide a pre-P gravity change for all three vector components.

Appendix D. Expression for theoretical gravito-gradiograms

Here, we show the theoretical gravito-gradiogram, the waveform of a gravity gradient, in an explicit form. Our formula can be used to synthesize template waveforms for the detection of pre-P gravity perturbations through the measurement of a gravity gradient or strain acceleration using state-of-the-art devices such as TOBA. Our expression is an extension of Harms et al. (2015) as it can deal with the general seismic source represented by a moment tensor.

We assume the same simplifications of Harms et al. (2015). The derivation starts from the equivalence between two potentials as follows (Harms et al. 2015):

$$\delta\psi(x,t) = -4\pi G\rho_0\phi(x,t), \tag{A1}$$

where x the receiver position, t the time, G the gravitational constant, ρ_0 the density of the medium, $\delta\psi$ the gravity potential perturbation, and ϕ the compressional seismic potential. From Equation A1, the gravity perturbation vector $\delta\boldsymbol{g}(x,t)$ is represented as follows:

$$\delta\boldsymbol{g}(x,t) = -\nabla\delta\psi(x,t) = 4\pi G\rho_0\nabla\phi(x,t) = 4\pi G\rho_0\boldsymbol{u}^{\phi}(x,t), \tag{A2}$$

where $\boldsymbol{u}^{\phi}$ is the scalar potential component of the seismic displacement $\boldsymbol{u}$ $\left(\boldsymbol{u}^{\phi} = \nabla\phi\right)$. Employing the well-known solution of the seismic displacement from a general seismic source represented by a moment tensor (Aki and Richards 2002), we obtained the analytic expression for the components of the pre-P gravity change $\delta\boldsymbol{g}(x,t)$ as follows:

$$\delta g_n = -\left(15\gamma_n\gamma_p\gamma_q - 3\gamma_n\delta_{pq} - 3\gamma_p\delta_{qn} - 3\gamma_q\delta_{np}\right)\frac{G}{r^4}\int_0^{r/\alpha}\tau M_{pq}(t-\tau)d\tau$$
$$+\left(6\gamma_n\gamma_p\gamma_q - \gamma_n\delta_{pq} - \gamma_p\delta_{qn} - \gamma_q\delta_{np}\right)\frac{G}{\alpha^2 r^2}M_{pq}\left(t-\frac{r}{\alpha}\right) \tag{A3}$$
$$+\gamma_n\gamma_p\gamma_q\frac{G}{\alpha^3 r}\dot{M}_{pq}\left(t-\frac{r}{\alpha}\right),$$

where γ_i the directional cosine, δ_{ij} the Kronecker delta, r the distance between the source and receiver, α the P-wave velocity, and $M_{pq}(t)$ the moment function. This expression uses orthonormal bases and is familiar to seismologists. The first term on the right-hand side shows the pre-P term. It coincides with that of Harms et al. (2015) for a shear dislocation (a double couple) source.

In contrast to the pre-P gravity change, the measurement of the corresponding gravity-gradient (or strain acceleration) is not affected by the ground acceleration motion. It is expressed as the spatial derivative of Equation A3 as follows:

$$\ddot{h}_{nm} := \frac{\partial \delta g_n}{\partial x_m} = 4\pi G\rho_0\frac{\partial u_n^{\phi}}{\partial x_m}$$
$$= R_5\frac{G}{r^5}\int_0^{\frac{r}{\alpha}}\tau M_{pq}(t-\tau)d\tau + R_3\frac{G}{\alpha^2 r^3}M_{pq}\left(t-\frac{r}{\alpha}\right) \tag{A4}$$
$$+R_2\frac{G}{\alpha^3 r^2}\dot{M}_{pq}\left(t-\frac{r}{\alpha}\right) + R_1\frac{G}{\alpha^4 r}\ddot{M}_{pq}\left(t-\frac{r}{\alpha}\right),$$

where $\ddot{h}_{nm}$ denotes the *nm*-th component of the gravity gradient tensor and

$$R_5 = 105\gamma_n\gamma_p\gamma_q\gamma_m - 15\left(\delta_{mn}\gamma_p\gamma_q + \delta_{mp}\gamma_q\gamma_n + \delta_{mq}\gamma_n\gamma_p + \delta_{pq}\gamma_n\gamma_m + \delta_{qn}\gamma_p\gamma_m + \delta_{np}\gamma_q\gamma_m\right)$$
$$+3\left(\delta_{pq}\delta_{mn} + \delta_{qn}\delta_{pm} + \delta_{np}\delta_{qm}\right),$$
$$R_3 = -45\gamma_n\gamma_p\gamma_q\gamma_m + 6\left(\delta_{mn}\gamma_p\gamma_q + \delta_{mp}\gamma_q\gamma_n + \delta_{mq}\gamma_n\gamma_p + \delta_{pq}\gamma_n\gamma_m + \delta_{qn}\gamma_p\gamma_m + \delta_{np}\gamma_q\gamma_m\right)$$
$$-\left(\delta_{pq}\delta_{mn} + \delta_{qn}\delta_{pm} + \delta_{np}\delta_{qm}\right),$$
$$R_2 = -10\gamma_n\gamma_p\gamma_q\gamma_m + \left(\delta_{mn}\gamma_p\gamma_q + \delta_{mp}\gamma_q\gamma_n + \delta_{mq}\gamma_n\gamma_p + \delta_{pq}\gamma_n\gamma_m + \delta_{qn}\gamma_p\gamma_m + \delta_{np}\gamma_q\gamma_m\right),$$
$$R_1 = -\gamma_n\gamma_p\gamma_q\gamma_m.$$

This tensor is symmetric and has six different components. Equation A4 has four terms on the right-hand side, and the first term is the pre-P term. Each term consists of a (i) radiation pattern, (ii) distance-dependent term, and (iii) time-dependent term. Once we specify the moment tensor, theoretical waveforms for any receiver position can be efficiently calculated using the formula. The full expression of $\frac{\partial u_n}{\partial x_m}$ is presented in Kimura and Kame (2019). The expression of theoretical gravito-gradiograms from a single-force source is presented in Kimura (2018).

Acknowledgements

First of all, I am deeply grateful to my advisor, Associate Professor Nobuki Kame. He has provided various support and encouragement on my research and research life. My thesis would never have been completed without him.

I would like to thank the dissertation committee (Associate Professor Yosuke Aoki, Professor Akito Araya, Associate Professor Yoshiyuki Tanaka, Associate Professor Kiwamu Nishida, and Professor Masato Furuya) for reviewing my thesis.

I am also grateful to my co-workers, Associate Professor Shingo Watada, Assistant Professor Makiko Ohtani, Professor Akito Araya, Associate Professor Yuichi Imanishi, Associate Professor Masaki Ando, Doctor Takashi Kunugi, and Doctor Rongjiang Wang for constructive discussions.

This research was supported by JSPS (KAKENHI JP15K13559, JP16K05532, JP18J21734, JP19K04009), and MEXT via the Program for Leading Graduate Schools, the Earthquake and Volcano Hazards Observation and Research Program, and Quantum Leap Flagship Program (MEXT Q-LEAP, JPMXS0118070351). The software packages Seismic Analysis Code (http://ds.iris.edu/ds/nodes/dmc/software/downloads/sac/) and Genetic Mapping Tools (https://www.generic-mapping-tools.org/download/) were used for data processing and figure plotting.

Finally, I express my great appreciation to my family for their understanding, support, and kind cooperation.

Data availability

The Kamioka and Matsushiro SG data used in our study are available on request from the authors of Kimura et al. (2019a). The F-net data are available at NIED F-net server http://www.fnet.bosai.go.jp. The Hi-net tiltmeter data used in our study can be obtained from NIED Japan by sending a request to hinet-admin@bosai.go.jp. The code QSSPPEGS as a stand-alone FORTRAN code can be downloaded from ftp://ftp.gfz-potsdam.de/pub/home/turk/wang/.

References

Abbott B P et al. (2016) Observation of Gravitational Waves from a Binary Black Hole Merger. Phys Rev Lett 116(6):61102. doi:10.1103/PhysRevLett.116.061102

Aki K, Richards P G (2002) Quantitative Seismology, 2nd edn. University Science Books, Susalito, California.

Ando M, Ishidoshiro K, Yamamoto K, Yagi K, Kokuyama W, Tsubono K, Takamori A (2010) Torsion-Bar Antenna for Low-Frequency Gravitational-Wave Observations. Phys Rev Lett 105(16):161101. doi:10.1103/PhysRevLett.105.161101

Aoi S, Asano Y, Kunugi T, Kimura T, Uehira K, Takahashi N, Ueda H, Shiomi K, Matsumoto T, Fujiwara H (2020) MOWLAS: NIED observation network for earthquake, tsunami and volcano. Earth Planets Space 72:126. doi:10.1186/s40623-020-01250-x

Chu R, Wei S, Helmberger D V, Zhan Z, Zhu L, Kanamori H (2011) Initiation of the great Mw 9.0 Tohoku–Oki earthquake. Earth Planet Science Let 308(3–4):277–283. doi:10.1016/j.epsl.2011.06.031

Crotwell H P, Owens T J, Ritsema J (1999) The TauP Toolkit: Flexible seismic travel-time and ray-path utilities. Seismol Res Lett 70(2):154–160. doi:10.1785/gssrl.70.2.154

Dahlen F A, Tromp J (1998) Theoretical Global Seismology. Princeton University Press.

Ekström G, Nettles M, Dziewoński A (2012) The global CMT project 2004–2010: centroid-moment tensors for 13,017 earthquakes. Phys Earth planet Inter 200:1–9.

Goldstein P, Snoke A (2005) SAC availablility for the IRIS Community, Incorporated Institutions for Seismology Data Management Center Electronic Newsletter.

Harms J (2016) Transient gravity perturbations from a double-couple in a homogeneous half-space. Geophys J Int 205(2):1153–1164. doi:10.1093/gji/ggw076

Harms J, Ampuero J P, Barsuglia M, Chassande-Mottin E, Montagner J-P, Somala S N, Whiting B F (2015) Transient gravity perturbations induced by earthquake rupture. Geophys J Int 201(3):1416–1425. doi:10.1093/gji/ggv090

Havskov J, Alguacil G (2016) Instrumentation in earthquake seismology 2nd edn. Springer, Dordrecht. doi:10.1007/978-3-319-21314-9

Hayes T J, Valluri S R, Mansinha L (2004) Gravitational effects from earthquakes. Can J Phys 82(12):1027–1040. doi:10.1139/p04-068

Heaton T H (2017) Correspondence: Response of a gravimeter to an instantaneous step in gravity. Nat Commun 8:66. doi:10.1038/s41467-017-01348-z

Ide S, Baltay A, Beroza G C (2011) Shallow dynamic overshoot and energetic deep rupture in the 2011 Mw 9.0 Tohoku-Oki earthquake. Science 332(6036):1426–1429. doi:10.1126/science.1207020

Imanishi Y (2001) Development of a High-Rate and High-Resolution Data Acquisition System Based on a Real-Time Operating System. J Geod Soc Japan 47(1):52–57. doi:10.11366/sokuchi1954.47.52

Imanishi Y (2005) On the possible cause of long period instrumental noise (parasitic mode) of a superconducting gravimeter. J Geod 78:683–690. doi:10.1007/s00190-005-0434-5

Imanishi Y (2009) High-frequency parasitic modes of superconducting gravimeters. J Geod 83:455–467. doi:10.1007/s00190-008-0253-6

Imanishi Y, Sato T, Higashi T, Sun W, Okubo S (2004) A network of superconducting gravimeters detects submicrogal coseismic gravity changes. Science 306(5695): 476–478. doi:10.1126/science.1101875

Juhel K, Ampuero J P, Barsuglia M, Bernard P, Chassande-Mottin E, Fiorucci D, Harms J, Montagner J-P, Vallée M, Whiting B F (2018) Earthquake early warning using future generation gravity strainmeters. J Geophys Res Solid Earth 123(12):10889–10902. doi:10.1029/2018JB016698

Juhel K, Montagner J-P, Vallée M, Ampuero J P, Barsuglia M, Bernard P, Clévédé E, Harms J, Whiting B F (2019) Normal mode simulation of prompt elastogravity signals induced by an earthquake rupture. Geophys J Int 216(2):935–947. doi:10.1093/gji/ggy436

Kame N, Kimura M (2019) The fundamental nature of a transient elastic response to prompt gravity perturbations. Geophys J Int 218:1136–1142. doi:10.1093/gji/ggz196

Kanamori H, Anderson D L (1975) Theoretical basis of some empirical relations in seismology. Bull Seismol Soc Am 65(5):1073–1095.

Kanamori H, Given J W (1981) Use of long-period surface waves for rapid determination of earthquake-source parameters. Phys Earth Planet Inter 27:8–31. doi:10.1016/0031-9201(81)90083-2

Kimura M (2018) No identification of predicted earthquake-induced prompt gravity signals in data recorded by gravimeters, seismometers, and tiltmeters and its interpretation based on the principle of gravimetry. Master thesis, the University of Tokyo, Japan. https://repository.dl.itc.u-tokyo.ac.jp/?action=pages_view_main&active_action=repository_view_main_item

_detail&item_id=51237&item_no=1&page_id=28&block_id=31

Kimura M, Kame N (2019) Representation Theorem and Green's Function (3) — Strain, Stress, and Density Perturbation Fields due to a Point Source Using 2nd Derivative of Green's Function in an Unbounded Homogeneous Isotropic Elastic Medium — (in japanese). Zisin 2 71:153–160. doi:10.4294/zisin.2017-20

Kimura M, Kame N, Watada S, Ohtani M, Araya A, Imanishi Y, Ando M, Kunugi T (2019a) Earthquake-induced prompt gravity signals identifed in dense array data in Japan. Earth Planets Space 71:27. doi:10.1186/s40623-019-1006-x

Kimura M, Kame N, Watada S, Ohtani M, Araya A, Imanishi Y, Ando M, Kunugi T (2019b) Reply to comment by Vallée et al. on "Earthquake-induced prompt gravity signals identifed in dense array data in Japan". Earth Planets Space 71:120. doi:10.1186/s40623-019-1099-2

Lay T, Ammon C J, Kanamori H, Kim M J, Xue L (2011) Outer trench-slope faulting and the 2011 Mw 9.0 off the Pacific coast of Tohoku Earthquake. Earth Planets Space 63:37. doi:10.5047/eps.2011.05.006

Mansinha L, Hayes T (2001) A search for gravitational disturbance from earthquakes. J Geod Soc Japan 47(1):359–363. doi:10.11366/sokuchi1954.47.359

Matsuo K, Heki K (2011) Coseismic gravity changes of the 2011 Tohoku-Oki earthquake from satellite gravimetry. Geophys Res Lett 38:7. doi:10.1029/2011GL049018

Montagner J-P, Juhel K, Barsuglia M, Ampuero J P, Chassande-Mottin E, Harms J, Whiting B, Bernard P, Clévédé E, Lognonné P (2016) Prompt gravity signal induced by the 2011 Tohoku-Oki earthquake. Nat. Commun 7:13349. doi:10.1038/ncomms13349

Müller G (1977) Earth-flattening approximation for body waves derived from geometric ray theory improvements, corrections and range of applicability. J Geophys 42:429–436.

Müller G (1985) The reflectivity method: A tutorial. J Geophys 58:153–174.

Obara K, Kasahara K, Hori S, Okada Y (2005) A densely distributed high-sensitivity seismograph network in Japan: Hi-net by National Research Institute for Earth Science and Disaster Prevention. Rev Sci Instrum 76:021301. doi:10.1063/1.1854197

Press W H, Teukolsky S A, Vetterling W T, Flannery B P (1992) Numerical recipes in C: the art of scientific computing 2nd edn. Cambridge Univ. Press, Cambridge, U.K

Rubin D B (1981) The Bayesian Bootstrap. Ann Stat 9(1):130–134.

Shimoda T, Juhel K, Ampuero J P, Montagner J-P, Barsuglia M (2020) Early earthquake detection capabilities of different types of future-generation gravity gradiometers. Geophys J Int 224(1):533–542. doi:10.1093/gji/ggaa486

Shiomi K (2012) New measurements of sensor orientation at NIED Hi-net stations. Rep NIED 80:1–20. doi:10.24732/nied.00001219 (in Japanese with English abstract)

Shiomi K, Obara K, Aoi S, Kasahara K (2003) Estimation on the azimuth of the Hi-net and KiK-net borehole seismometers. Zisin2 56:99–110. doi:10.4294/zisin1948.56.1_99 (in Japanese)

Shoda A, Ando M, Ishidoshiro K, Okada K, Kokuyama W, Aso Y, Tsubono K (2014) Search for a stochastic gravitational-wave background using a pair of torsion-bar antennas. Phys Rev D 89(2):27101. doi:10.1103/PhysRevD.89.027101

Stein S, Wysession M (2003) An introduction to seismology, earthquakes, and earth structure. Blackwell Publication, Malden, MA

Takamoto M, Ushijima I, Ohmae N, Yahagi T, Kokado K, Shinkai H, Katori H (2020) Test of general relativity by a pair of transportable optical lattice clocks. Nat Photonics 14:411–415. doi:10.1038/s41566-020-0619-8

Tonegawa T, Hirahara K, Shibutani T, Shiomi K (2006) Upper mantle imaging beneath the Japan Islands by Hi-net tiltmeter recordings. Earth Planets Space 58(8):1007–1012. doi:10.1186/BF03352605

Tsai V C, Hayes G P, Duputel Z (2011) Constraints on the long‐period moment‐dip tradeoff for the Tohoku earthquake. Geophys Res Lett 38(7):L00G17. doi:10.1029/2011GL049129

Ushijima I, Takamoto M, Das M, Ohkubo T, Katori H (2015) Cryogenic optical lattice clocks. Nat Photon 9:185–189. doi:10.1038/nphoton.2015.5

Vallée M, Ampuero J P, Juhel K, Bernard P, Montagner J-P, Barsuglia M (2017) Observations and modeling of the elastogravity signals preceding direct seismic waves. Science 358:1164–1168. doi:10.1126/science.aao0746

Vallée M, Juhel K (2019) Multiple observations of the prompt elastogravity signals heralding direct seismic waves. J Geophys Res Solid Earth 124 (3):2970–2989. doi:10.1029/2018JB017130

Wang L, Shum C K, Jekeli C (2012) Gravitational gradient changes following the 2004 December 26 Sumatra–Andaman Earthquake inferred from GRACE. Geophys J Int 191(3): 1109–1118. doi:10.1111/j.1365-246X.2012.05674.x

Wang L, Shum C K, Simons F J, Tassara A, Erkan K, Jekeli C, Braun A, Kuo C, Lee H, Yuan D (2012) Coseismic slip of the 2010 Mw 8.8 Great Maule, Chile, earthquake quantified by the inversion of GRACE observations. Earth planet Sci Lett 335: 167–179. doi:10.1016/j.epsl.2012.04.044

Wei S, Graves R, Helmberger D, Avouac J-P, Jiang J (2012) Sources of shaking and flooding during the Tohoku-Oki earthquake: a mixture of rupture styles. Earth Planet Sci Lett 333–334:91–100. doi:10.1016/j.epsl.2012.04.006

Zhang S, Wang R, Dahm T, Zhou S, Heimann S (2020) Prompt elasto-gravity signals (PEGS) and their potential use in modern seismology. Earth planet Sci Lett 536:116150. doi:10.1016/j.epsl.2020.116150

Supplement

- Template waveforms of three-component pre-P gravity signal and gravity potential for
  - strike slip events (strike = 0°, dip = 90°, rake = 0°, depth = 20 km, Mw = 9 or 8) and
  - dip slip events (strike = 180°, dip = 15° or 30°, rake = 90°, depth = 20 km, Mw = 9 or 8)

  calculated by the simulation method of Zhang et al. (2020). The moment rate function and rupture duration were determined in the same way as in Chapter 4. Observation stations locate at θ = 0°, 15°, 30°, 45°, 60°, 75°, 90°, 105°, 120°, 135°, 150°, 165°, or 180° and Δ = 1°, 3°, 10°, or 30°. Here, θ is the azimuth measured from east to north, and Δ is the angular distance. The 0.15-Hz 6-pole low-pass causal Butterworth filter was applied to the waveforms.

- Results of the preliminary analysis to search for pre-P elastic strain in the data recorded by the 100-m-long laser strainmeter at Kamioka (Araya et al. 2007).
  - Background noise spectra of the linear ($u_{x,x}$) and shear ($\left(u_{y,y} - u_{x,x}\right)/2$) strains at the Kamioka strainmeter. The time window is 1 h between 04:40 and 05:40 UTC before the 2011 Tohoku-Oki event. Here, x and y axes are taken eastward and northward, respectively.
  - Comparison of the recorded strains and synthetic ones calculated by the simulation method of Zhang et al. (2020) before the P-wave arrival from the

2011 Tohoku-Oki earthquake. The 0.01-Hz 2-pole high-pass and 0.05-Hz 6-pole low-pass causal Butterworth filters were applied to both waveforms.

Vertical Acceleration a_z - dg_z (Strike Slip Mw 9)

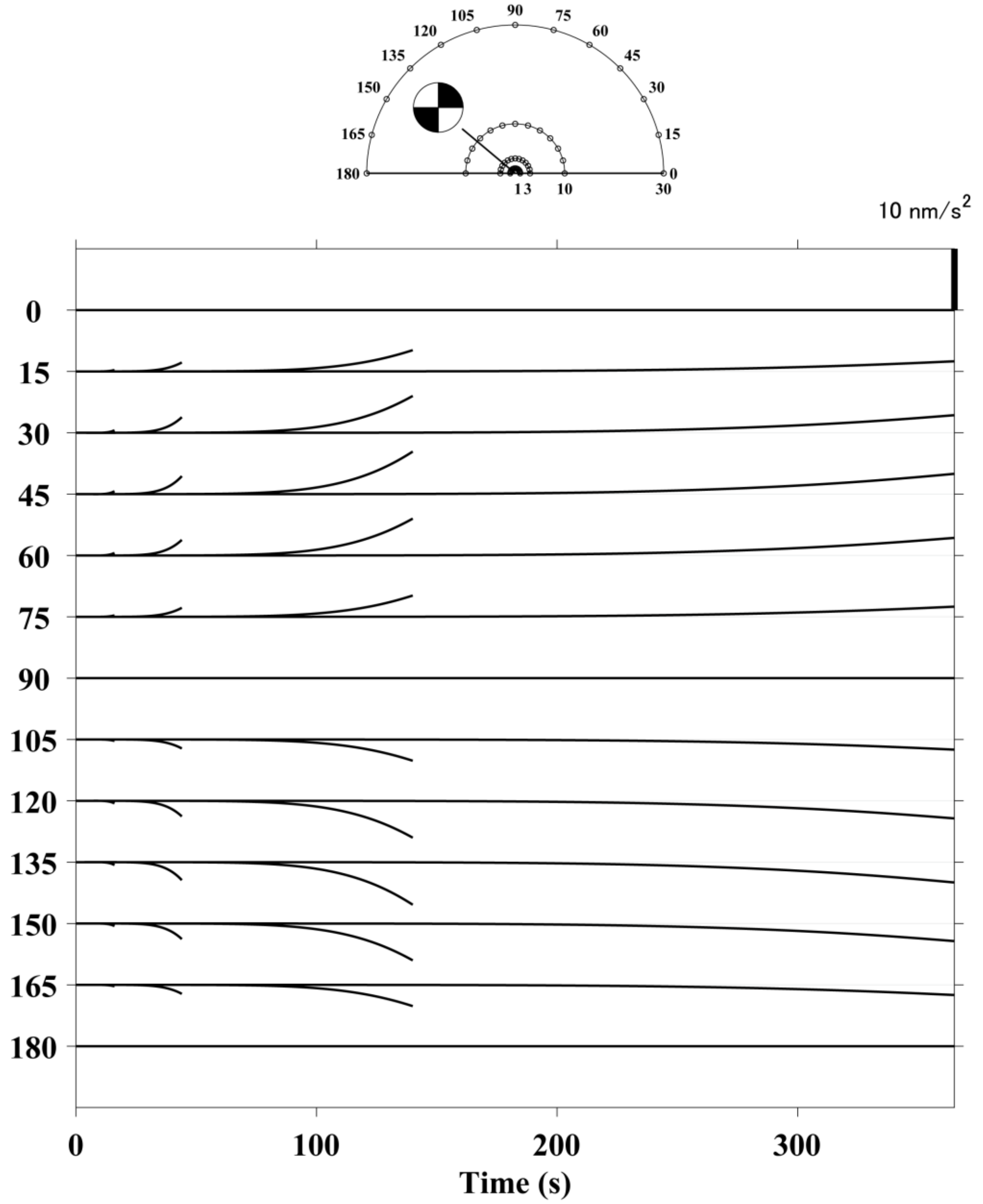

Radial Acceleration a_r - dg_r (Strike Slip Mw 9)

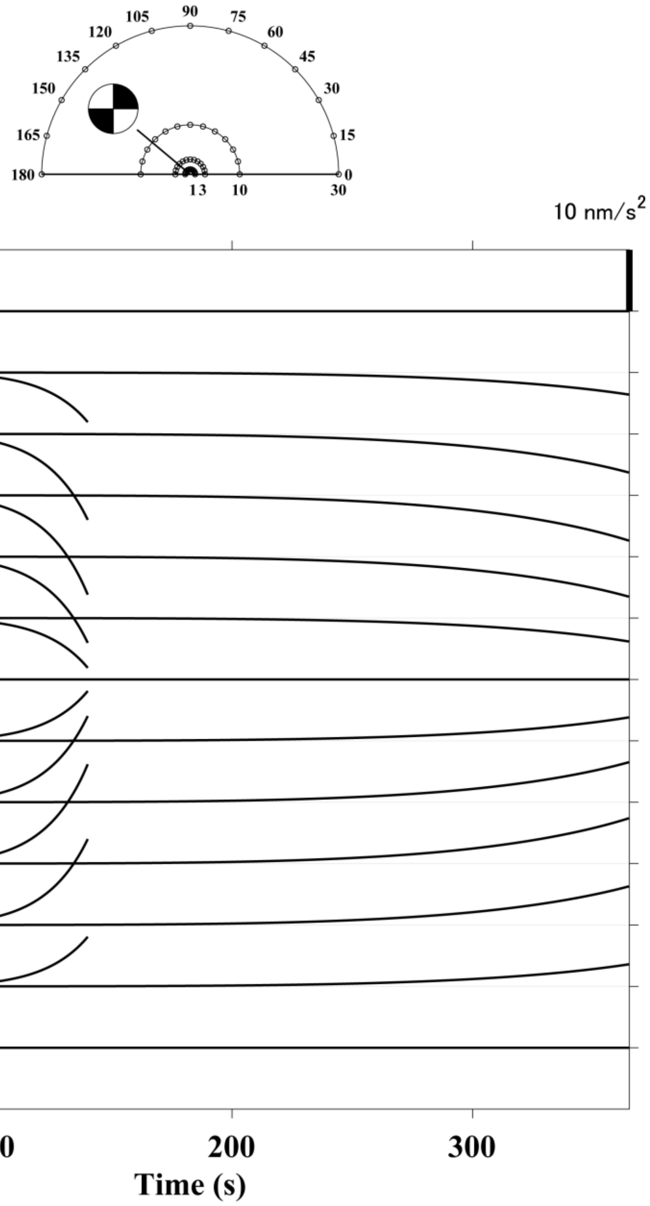

Transverse Acceleration a_t - dg_t (Strike Slip Mw 9)

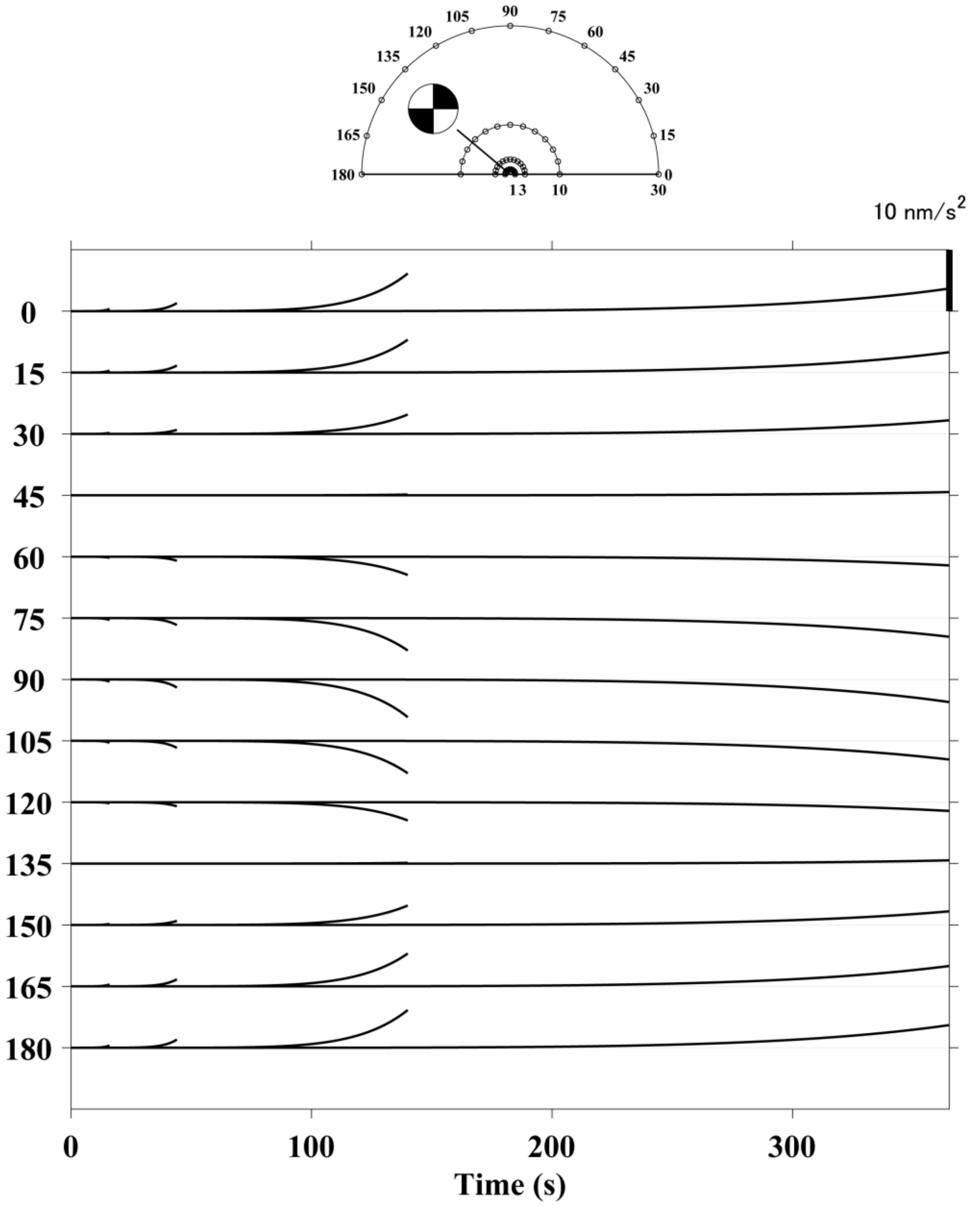

Gravity Potential dψ (Strike Slip Mw 9)

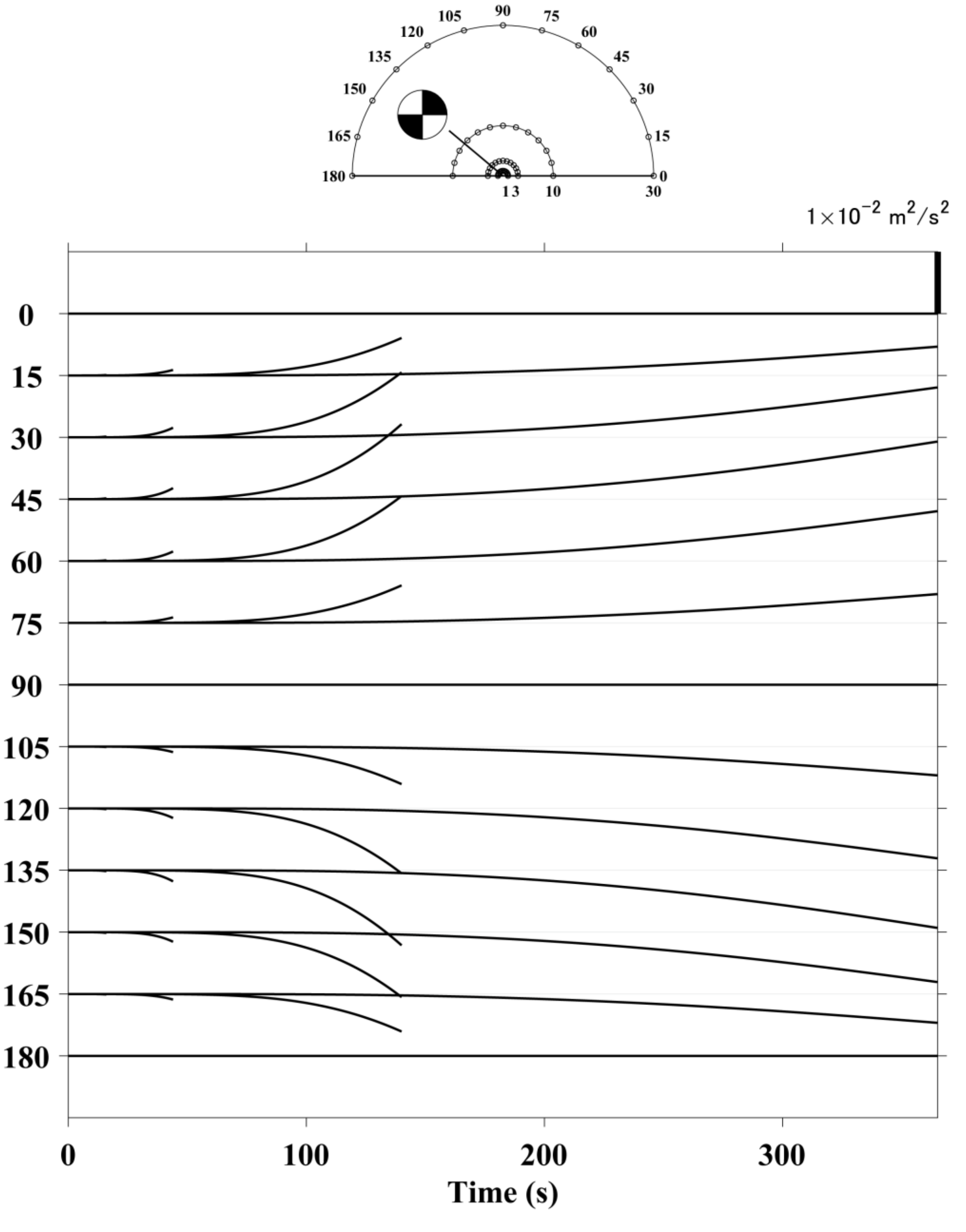

Vertical Acceleration a_z - dg_z (Strike Slip Mw 8)

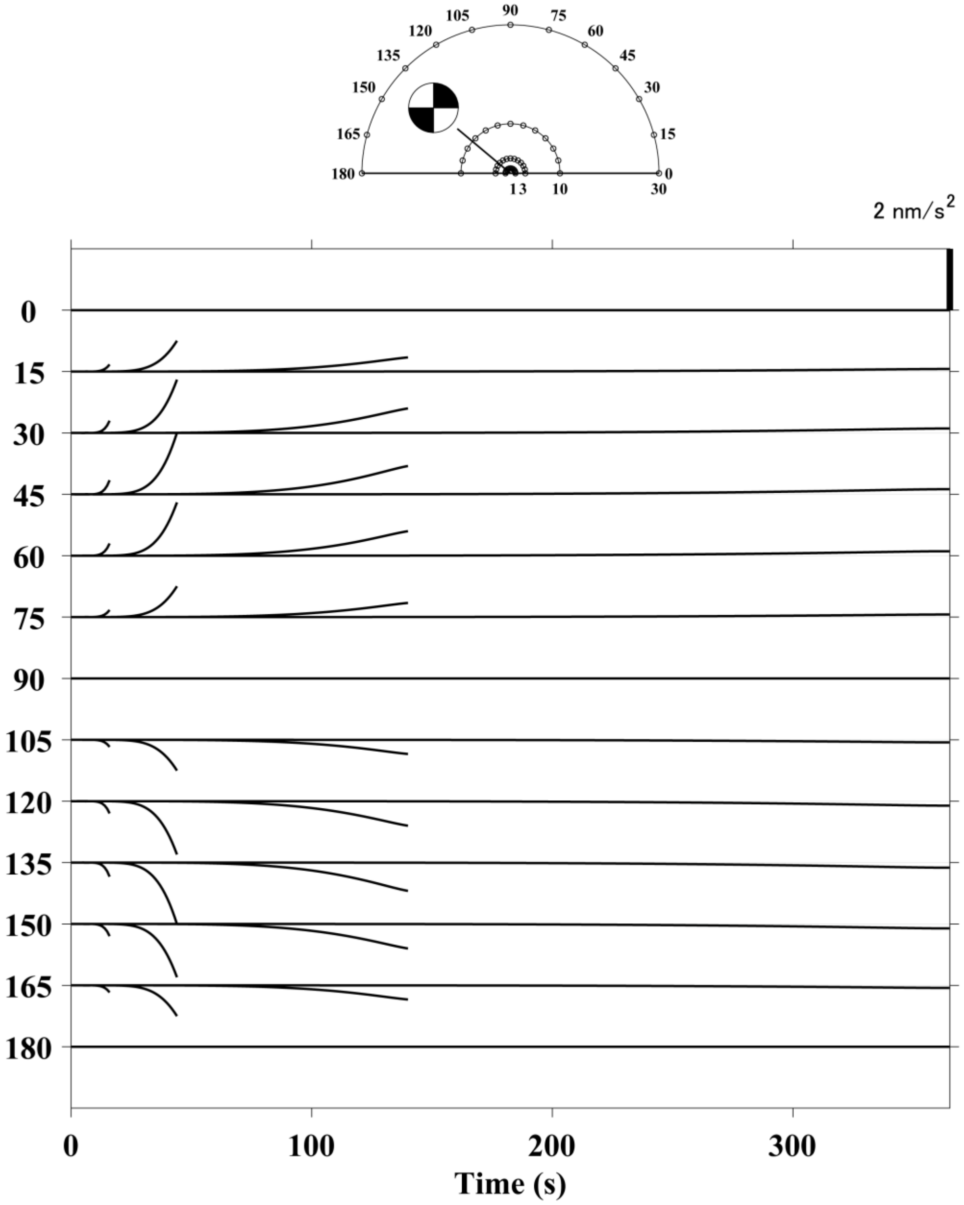

Radial Acceleration a_r - dg_r (Strike Slip Mw 8)

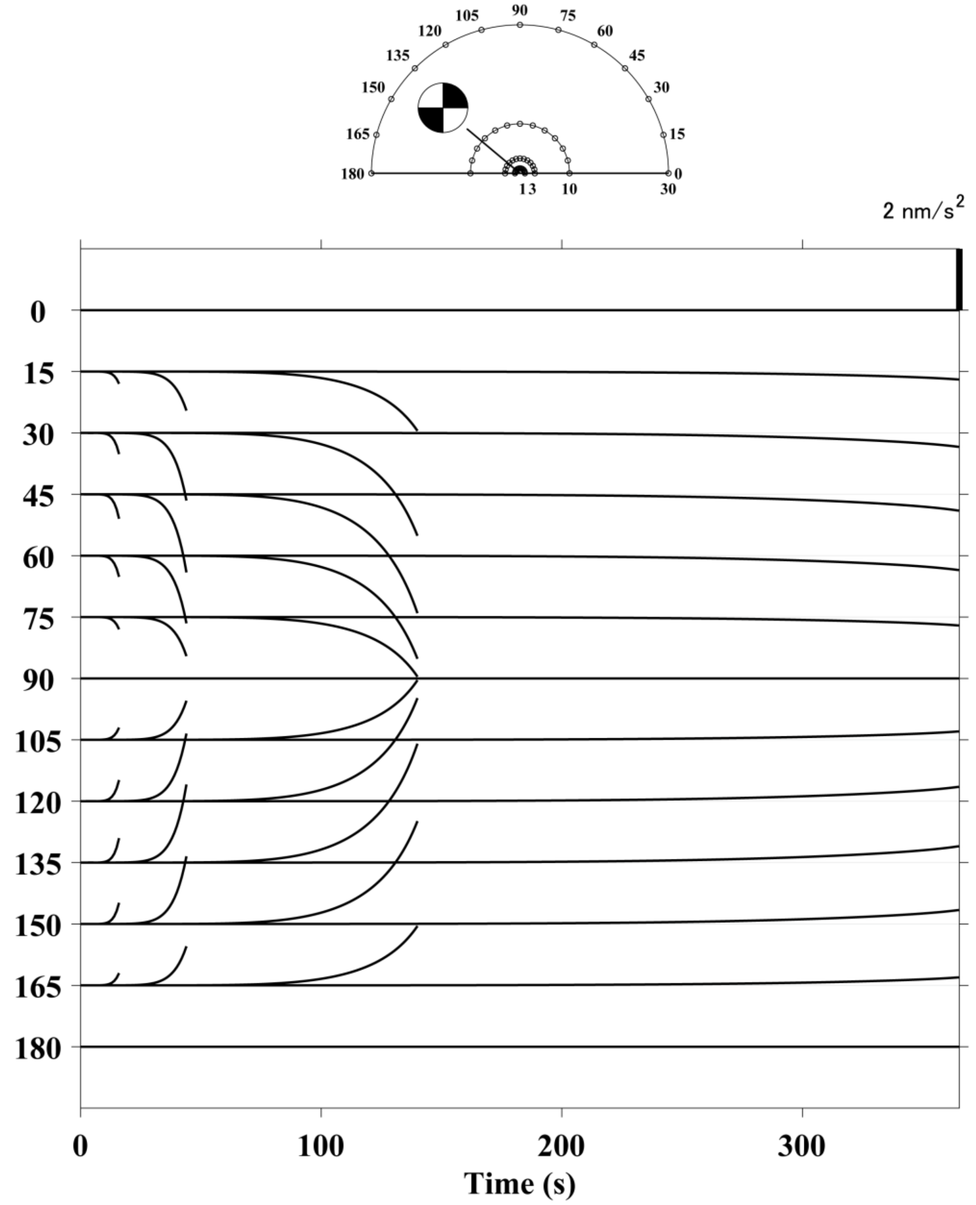

Transverse Acceleration a_t - dg_t (Strike Slip Mw 8)

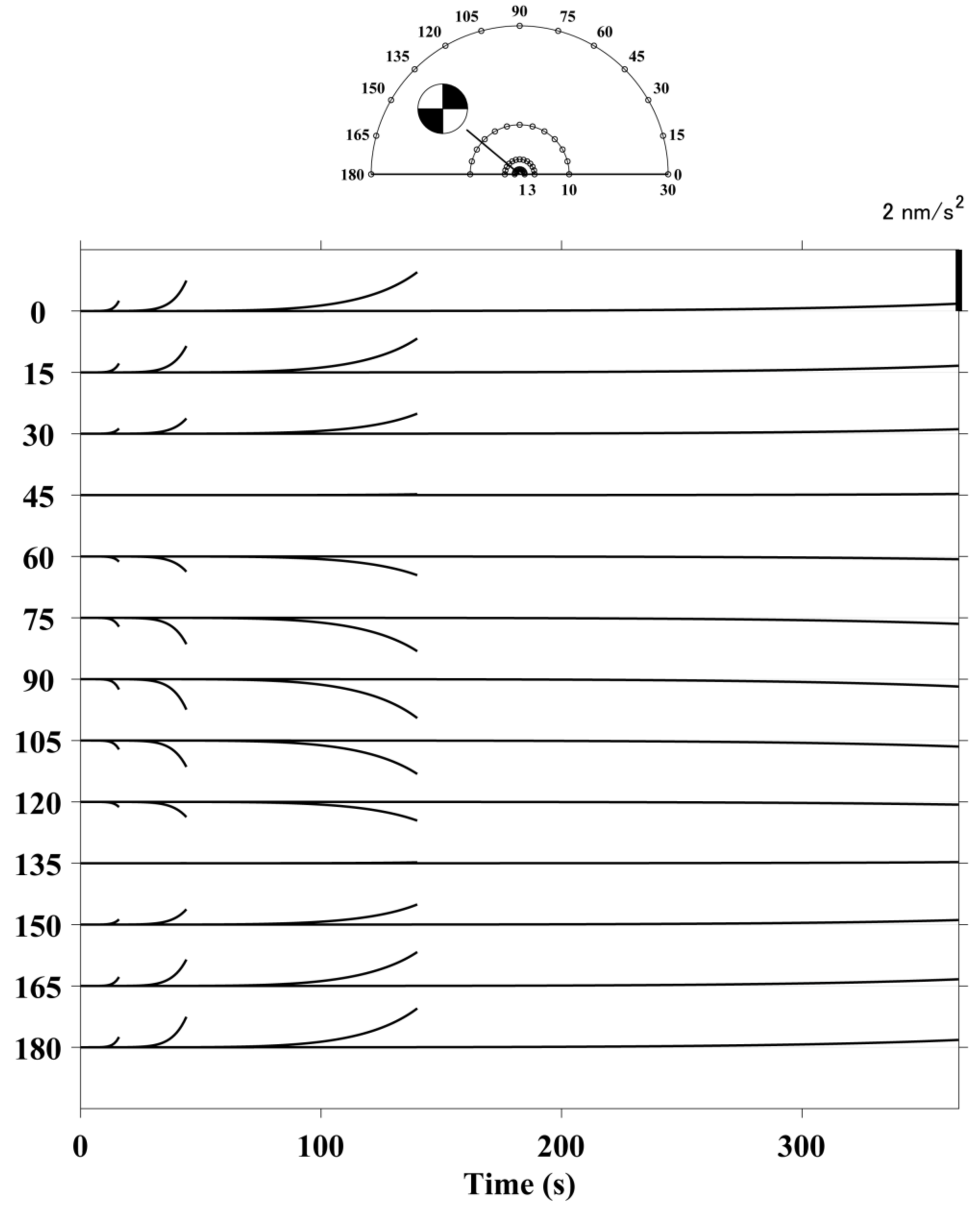

Gravity Potential dψ (Strike Slip Mw 8)

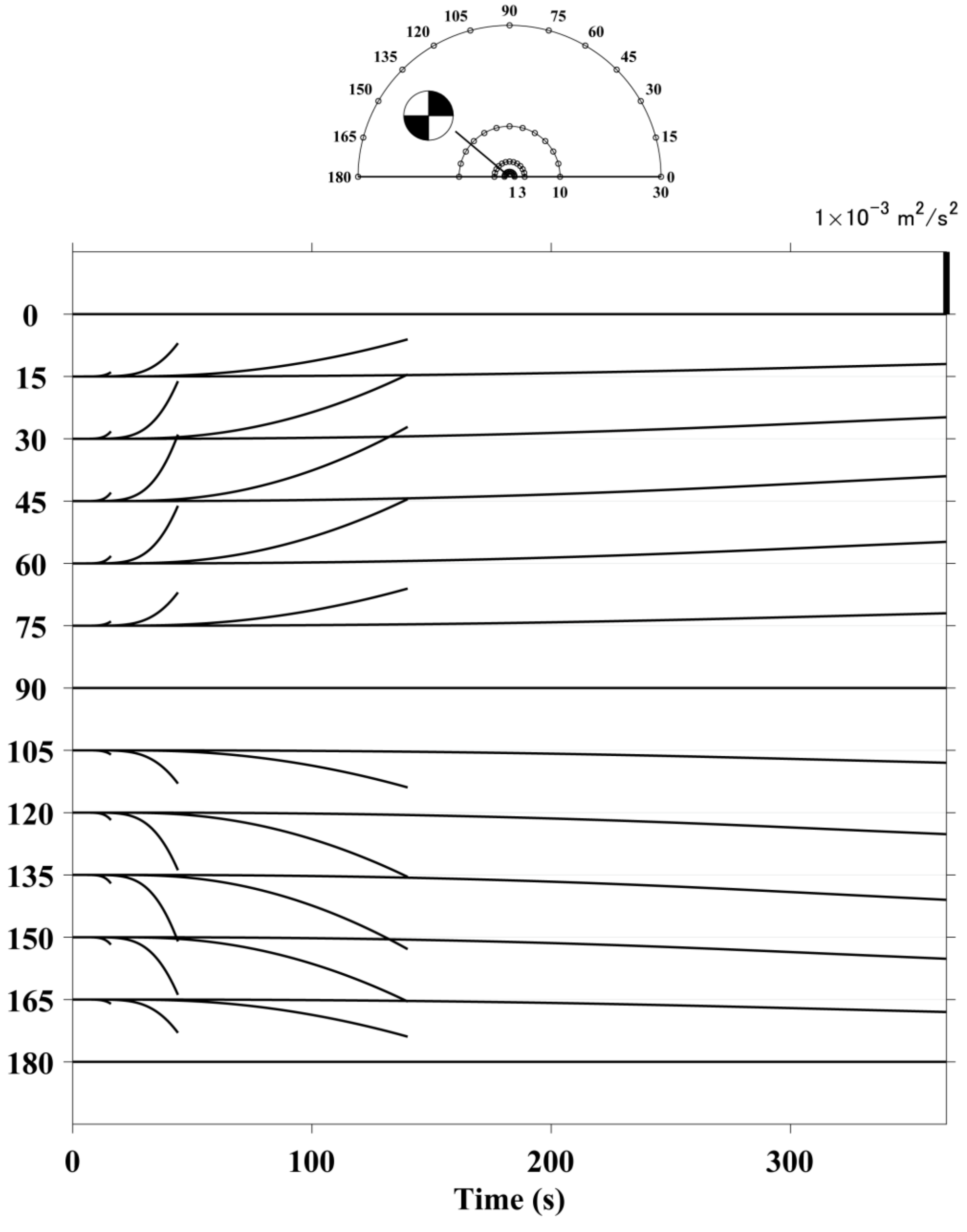

Vertical Acceleration a_z - dg_z (Dip Slip Mw 9)

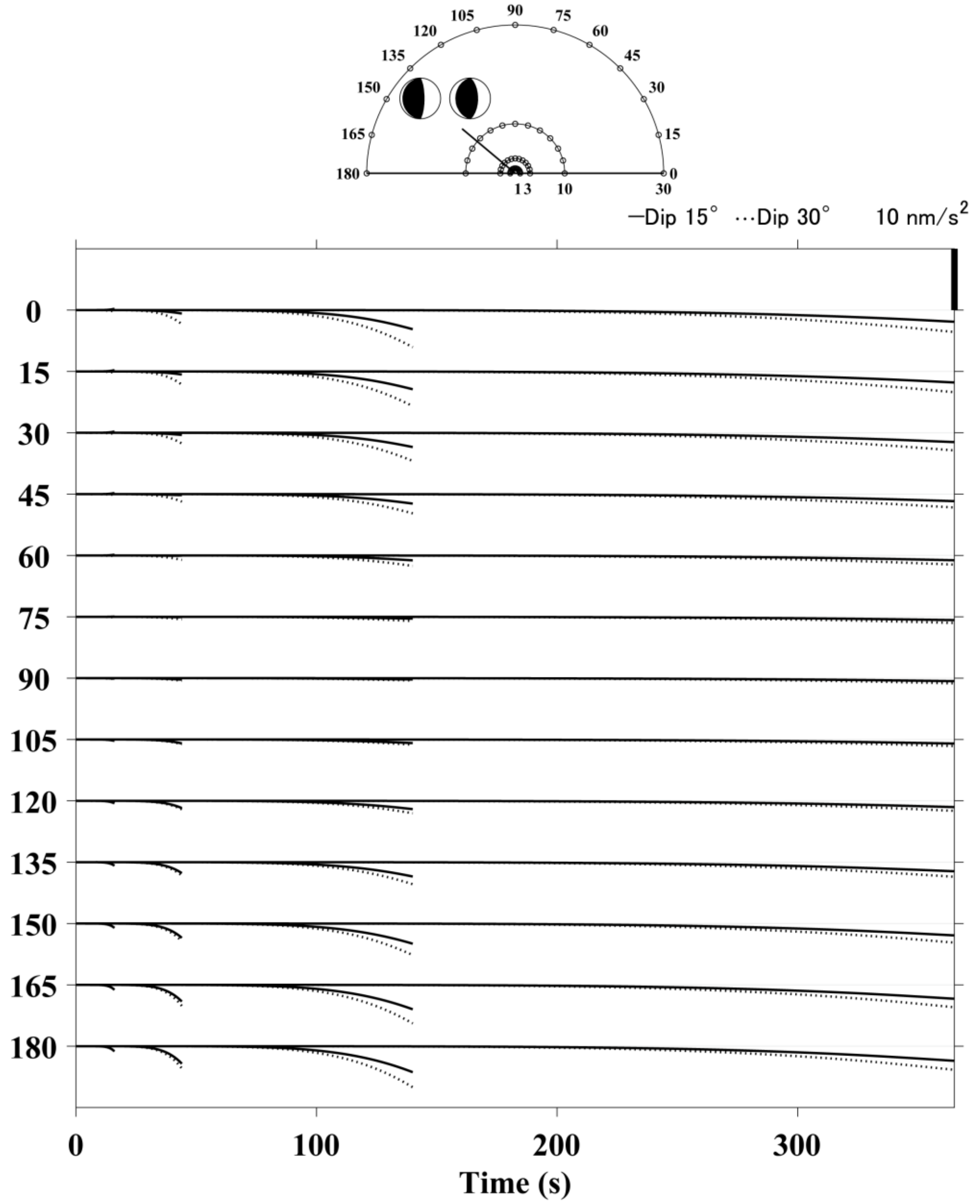

Radial Acceleration a_r - dg_r (Dip Slip Mw 9)

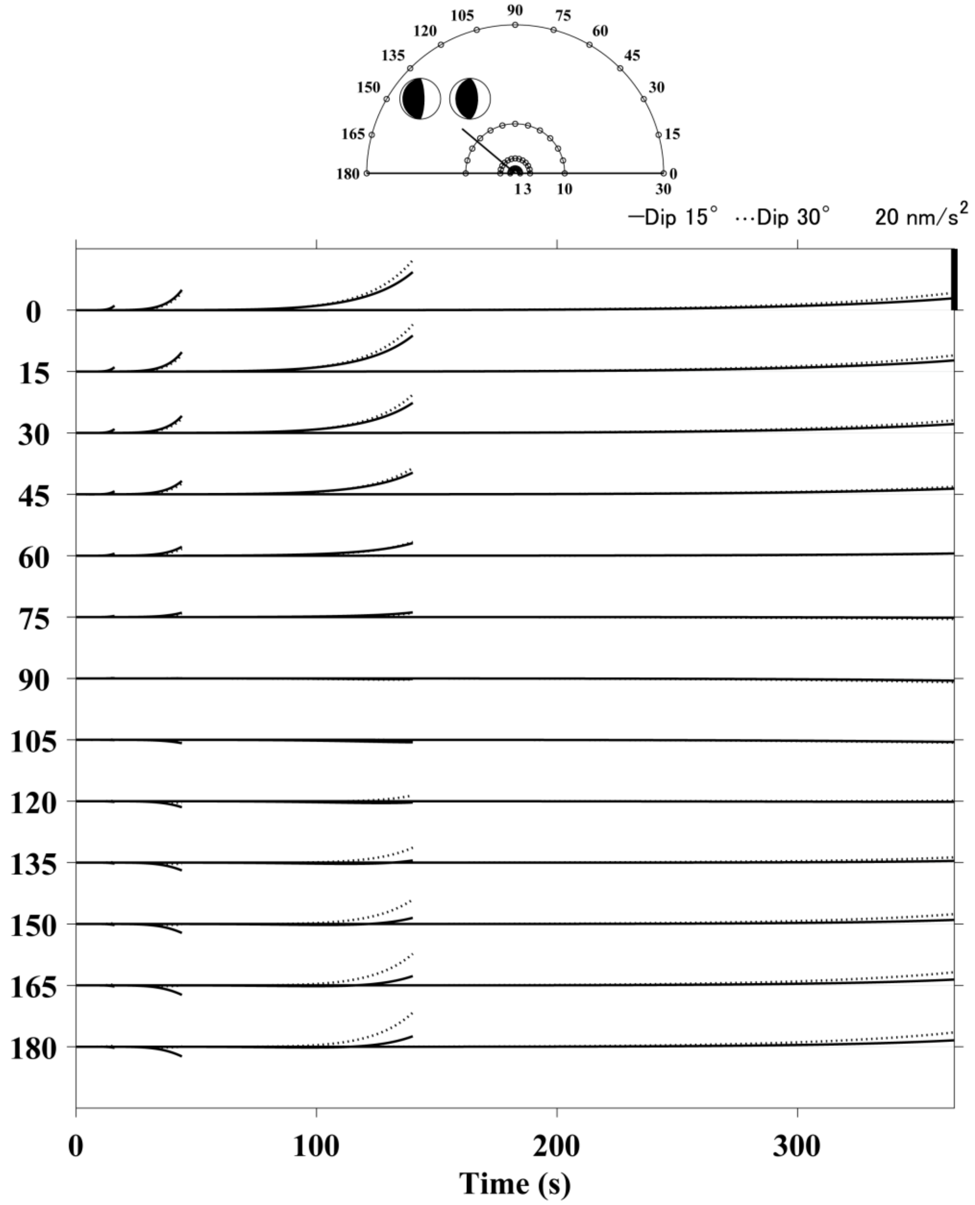

Transverse Acceleration a_t - dg_t (Dip Slip Mw 9)

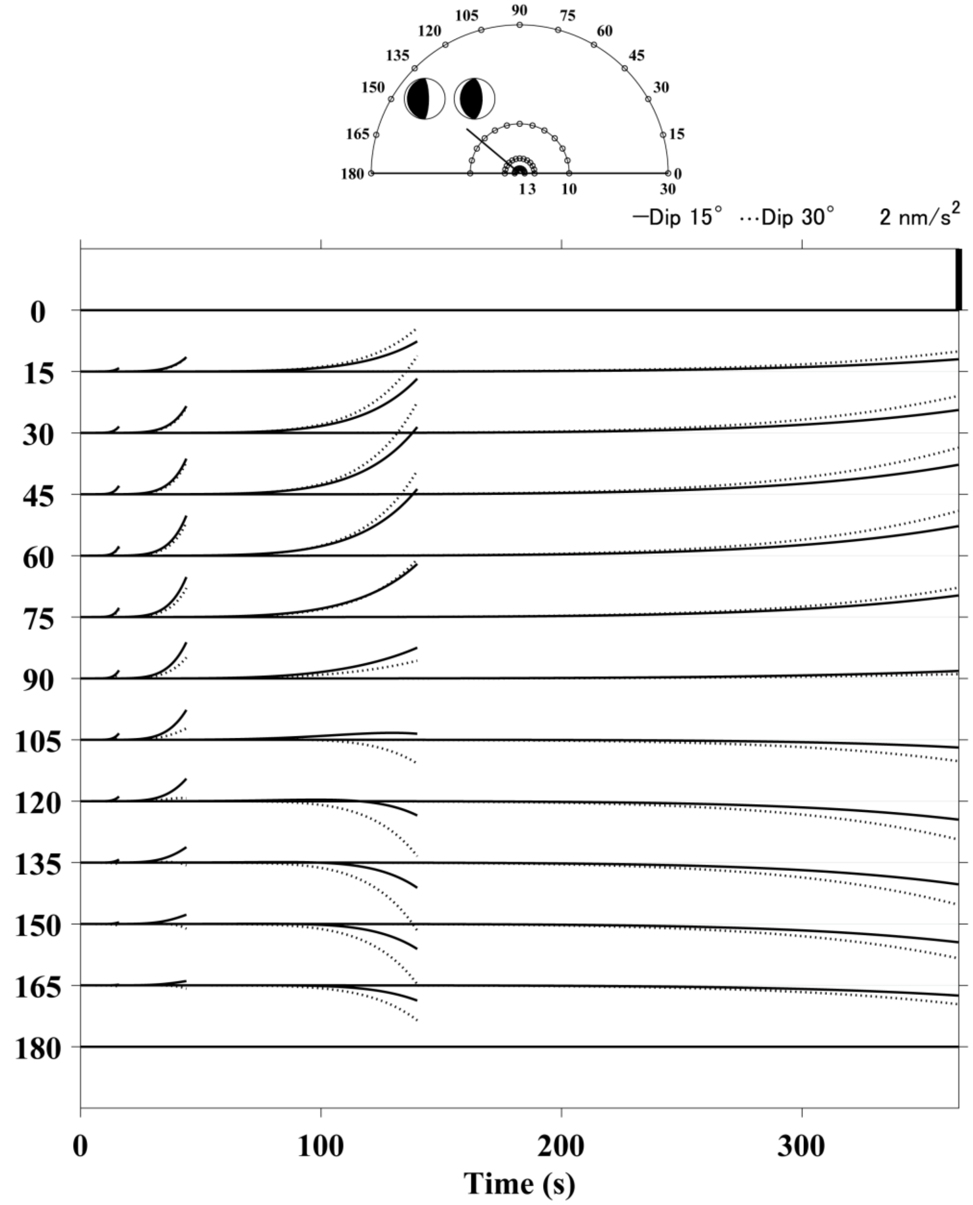

Gravity Potential dψ (Dip Slip Mw 9)

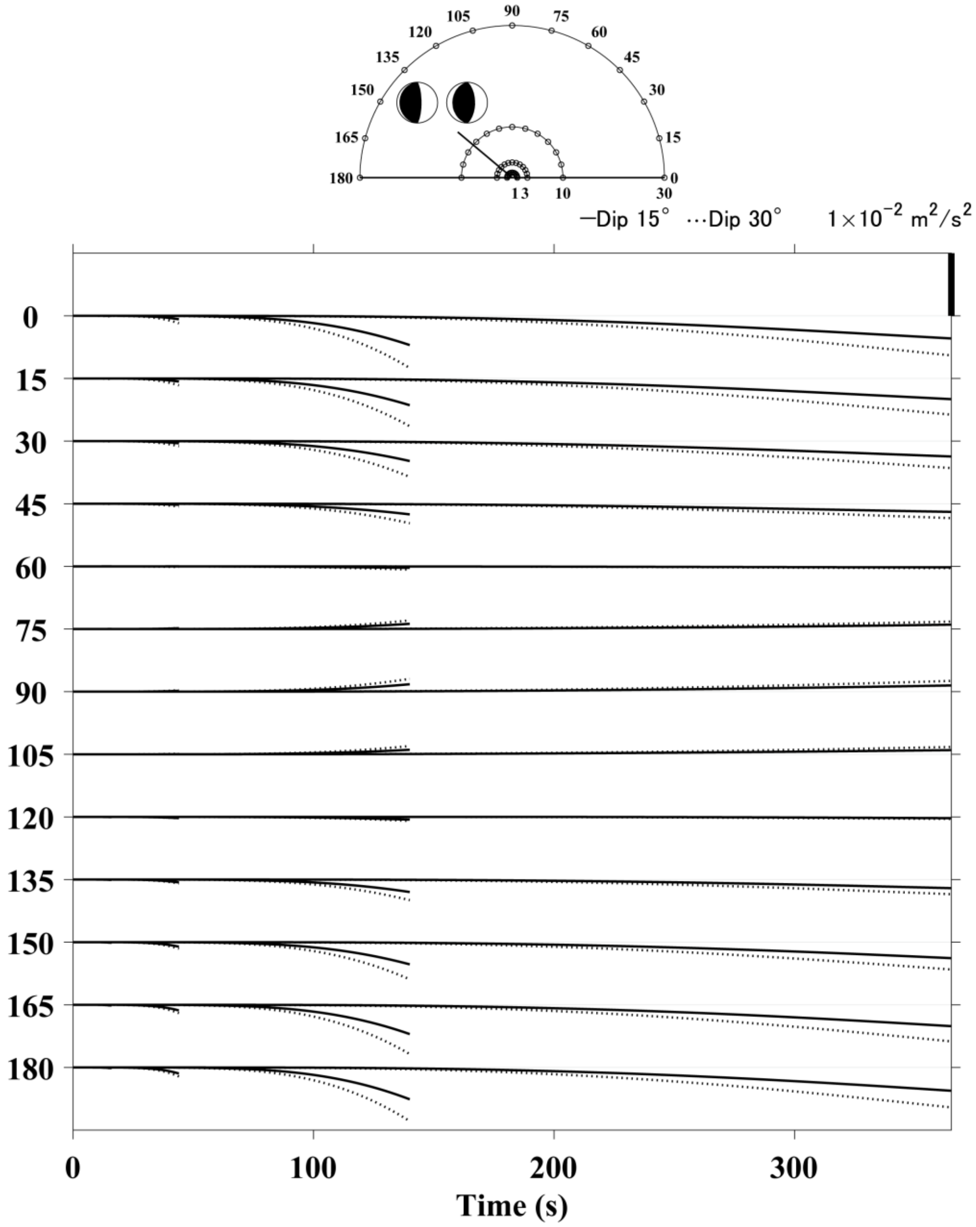

Vertical Acceleration a_z - dg_z (Dip Slip Mw 8)

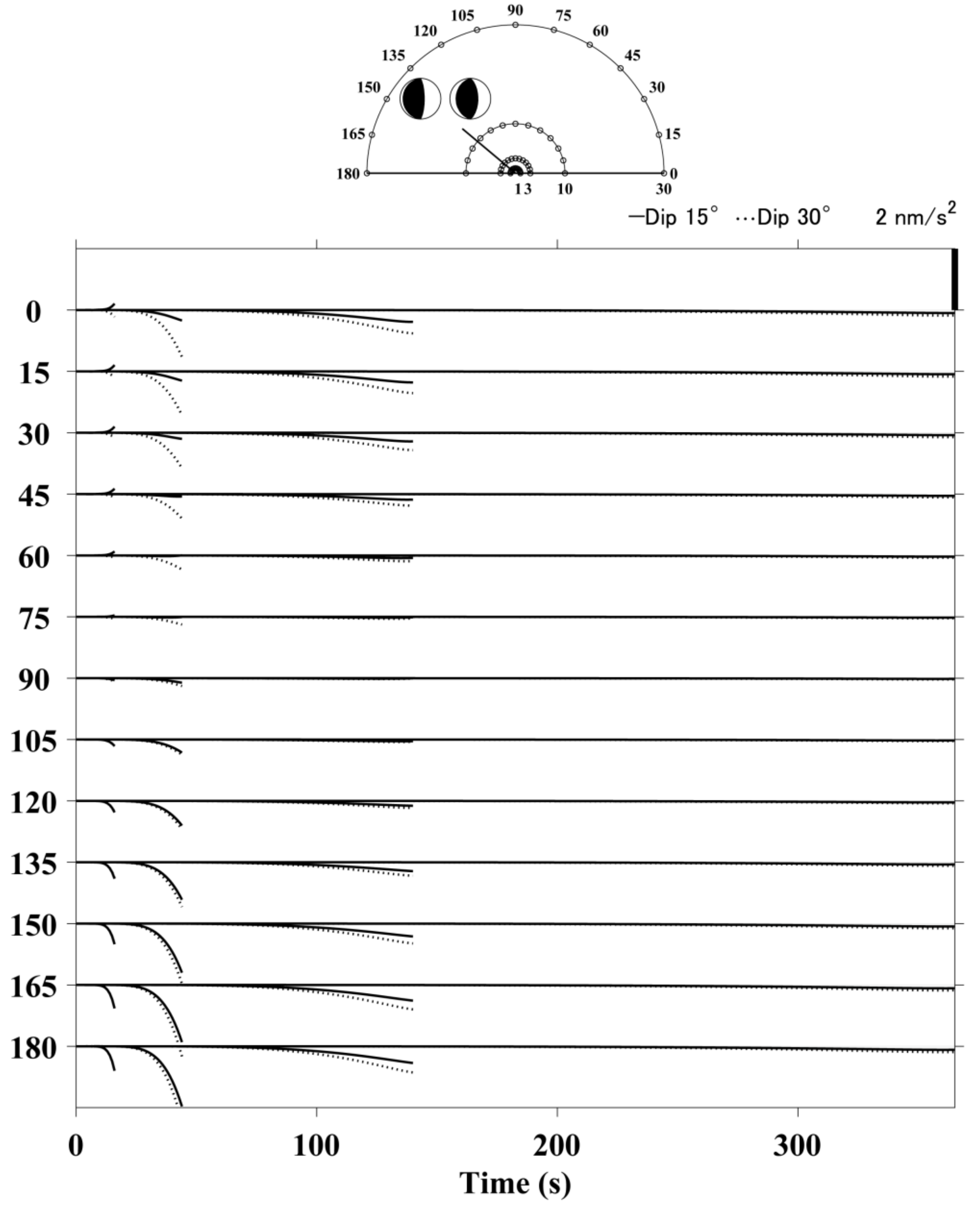

Radial Acceleration a_r - dg_r (Dip Slip Mw 8)

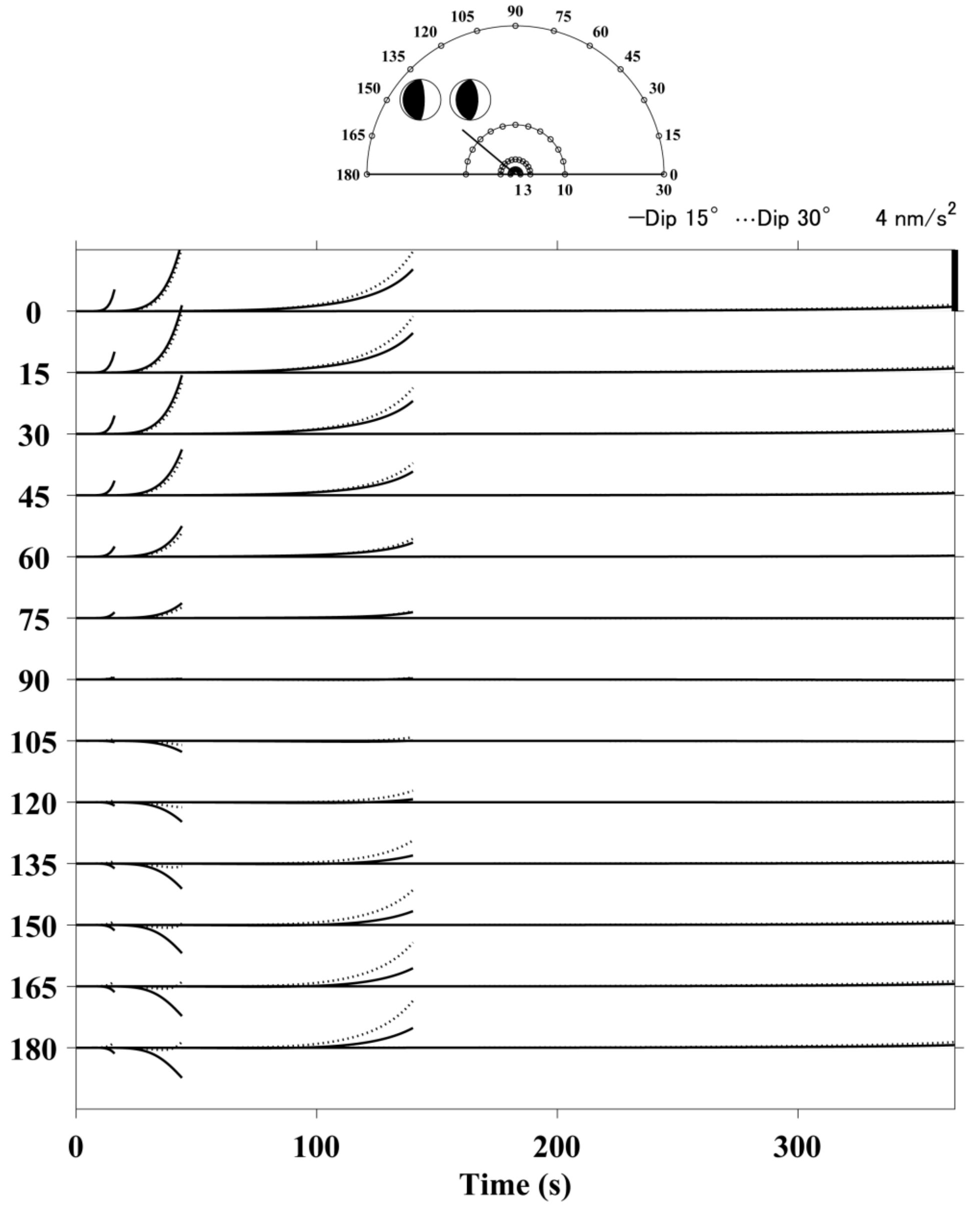

Transverse Acceleration a_t - dg_t (Dip Slip Mw 8)

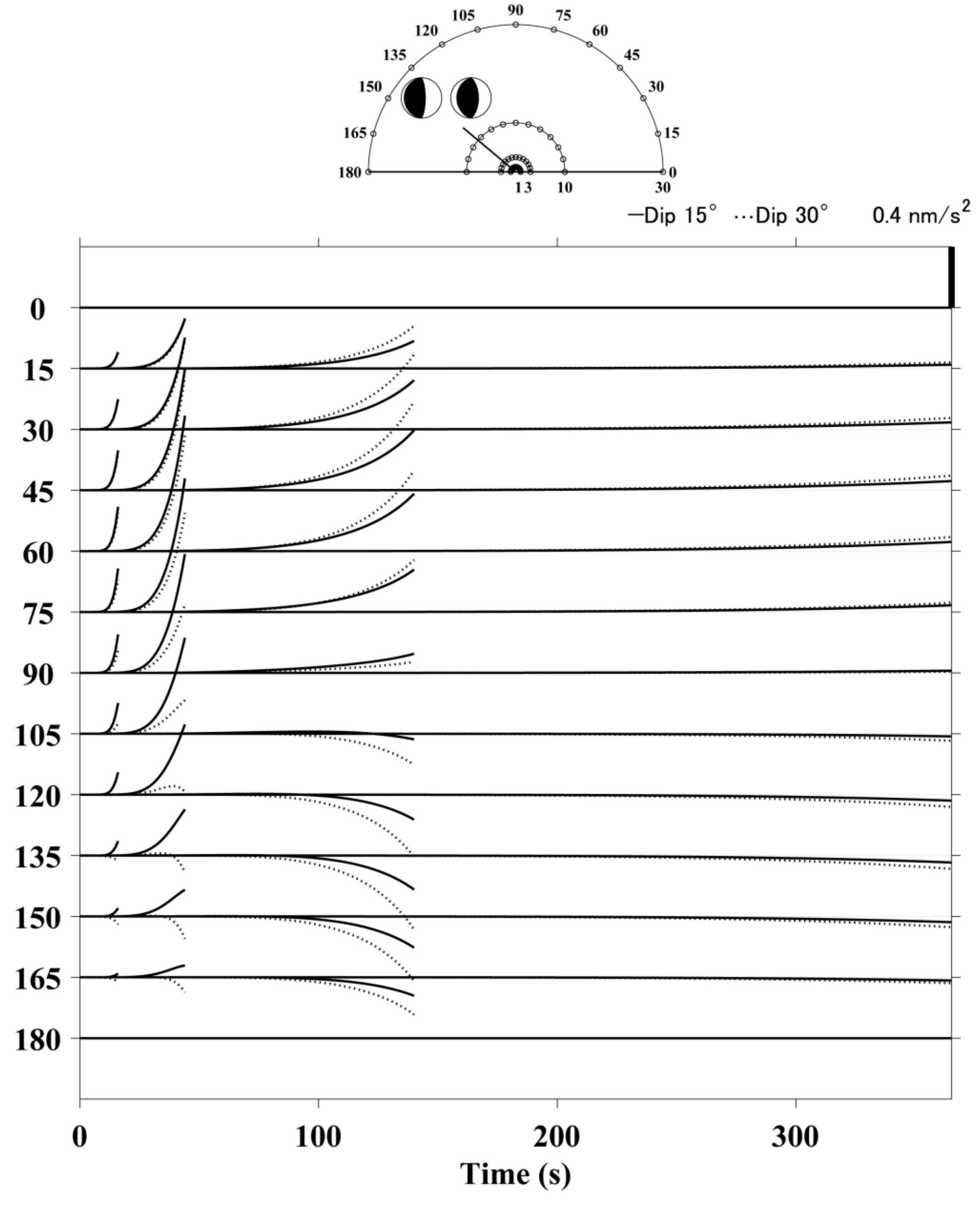

Gravity Potential dψ (Dip Slip Mw 8)

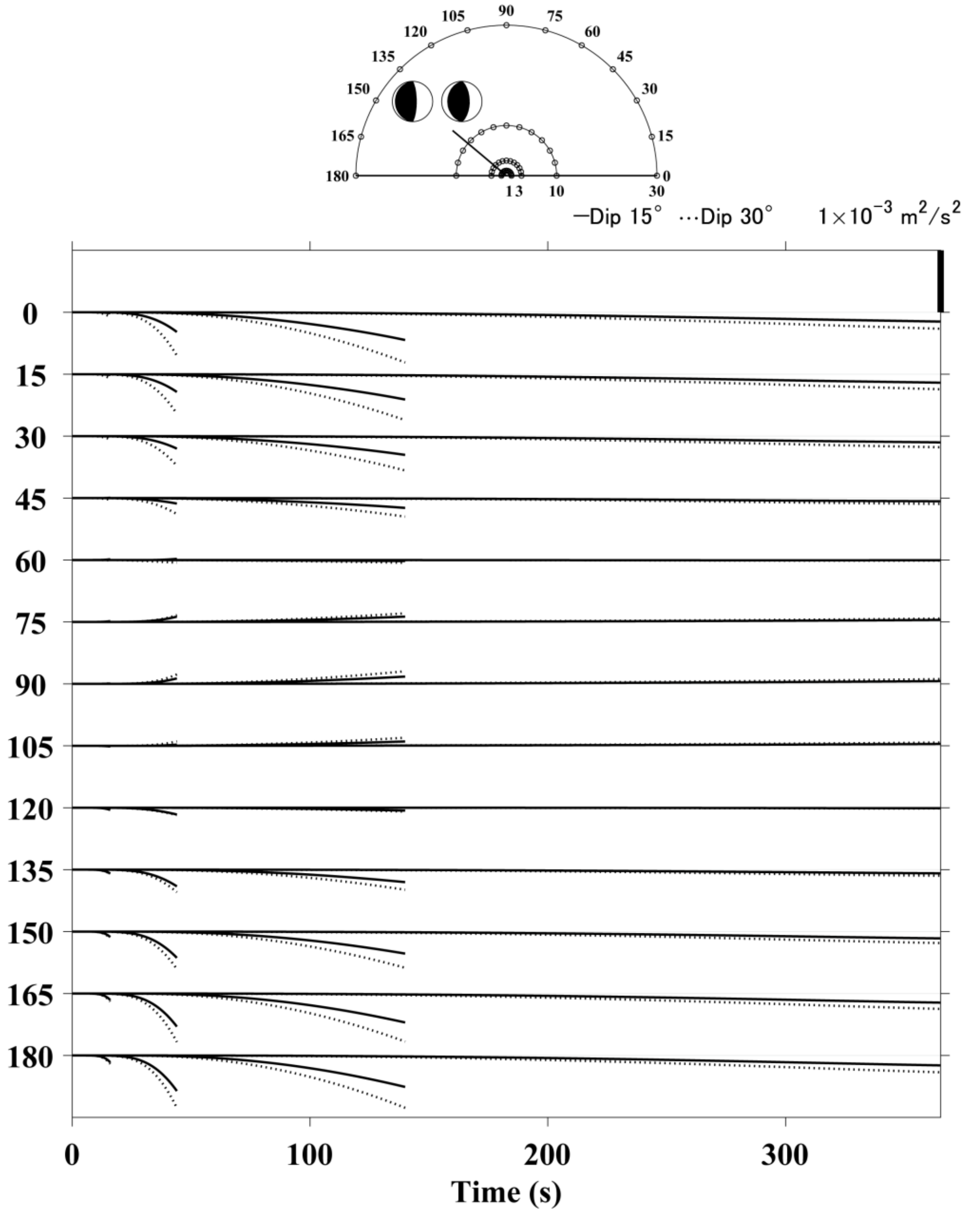

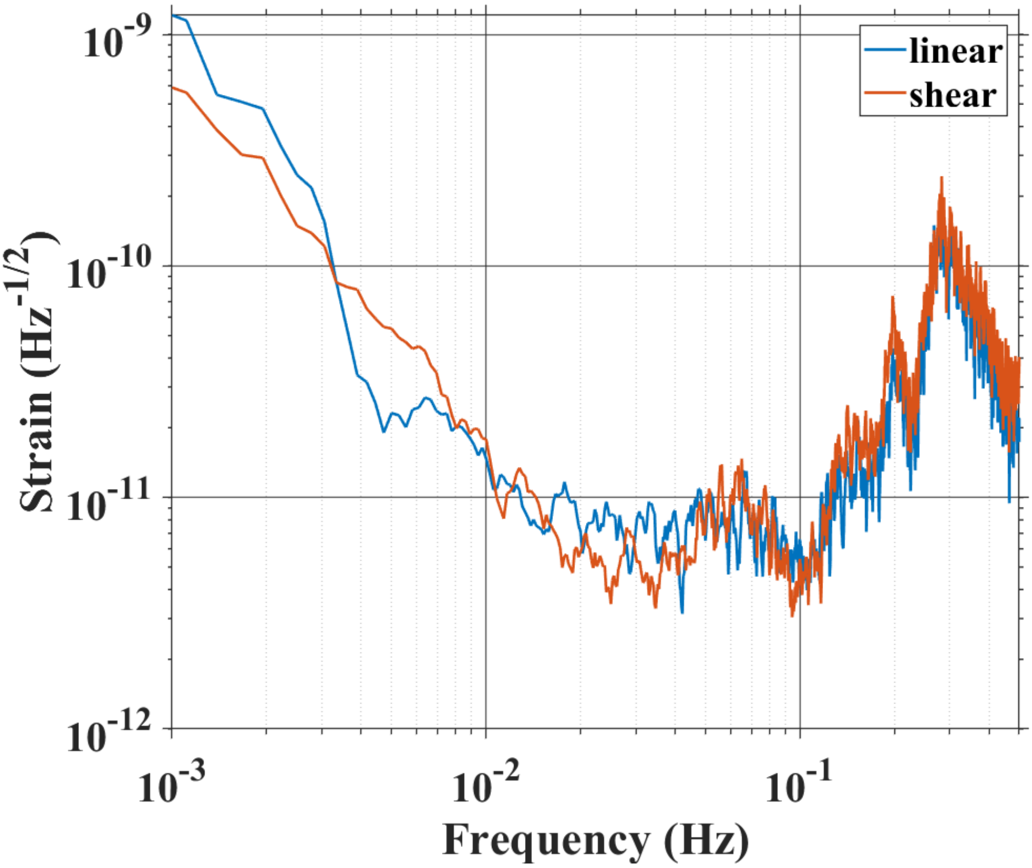
linear
shear
Strain ($Hz^{-1/2}$)
10^{-9}
10^{-10}
10^{-11}
10^{-12}
10^{-3}
10^{-2}
10^{-1}
Frequency (Hz)

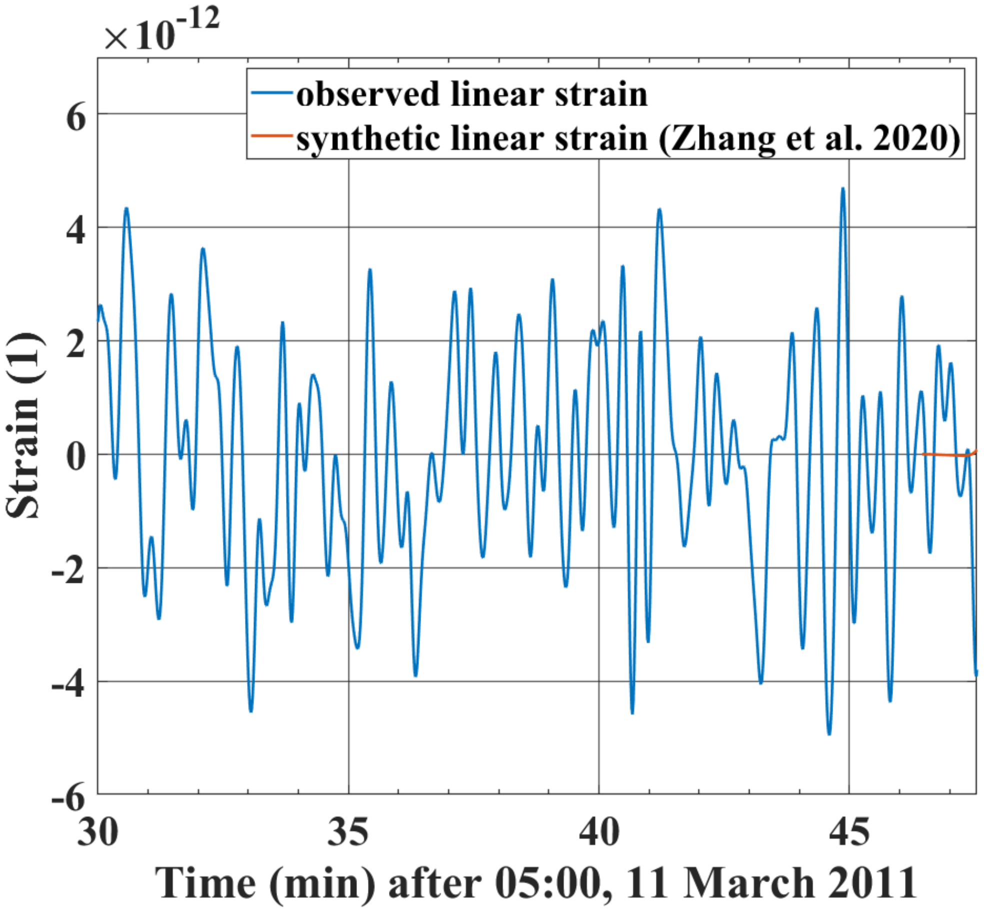
×10^-12
observed linear strain
synthetic linear strain (Zhang et al. 2020)
Strain (1)
6
4
2
0
-2
-4
-6
30
35
40
45
Time (min) after 05:00, 11 March 2011

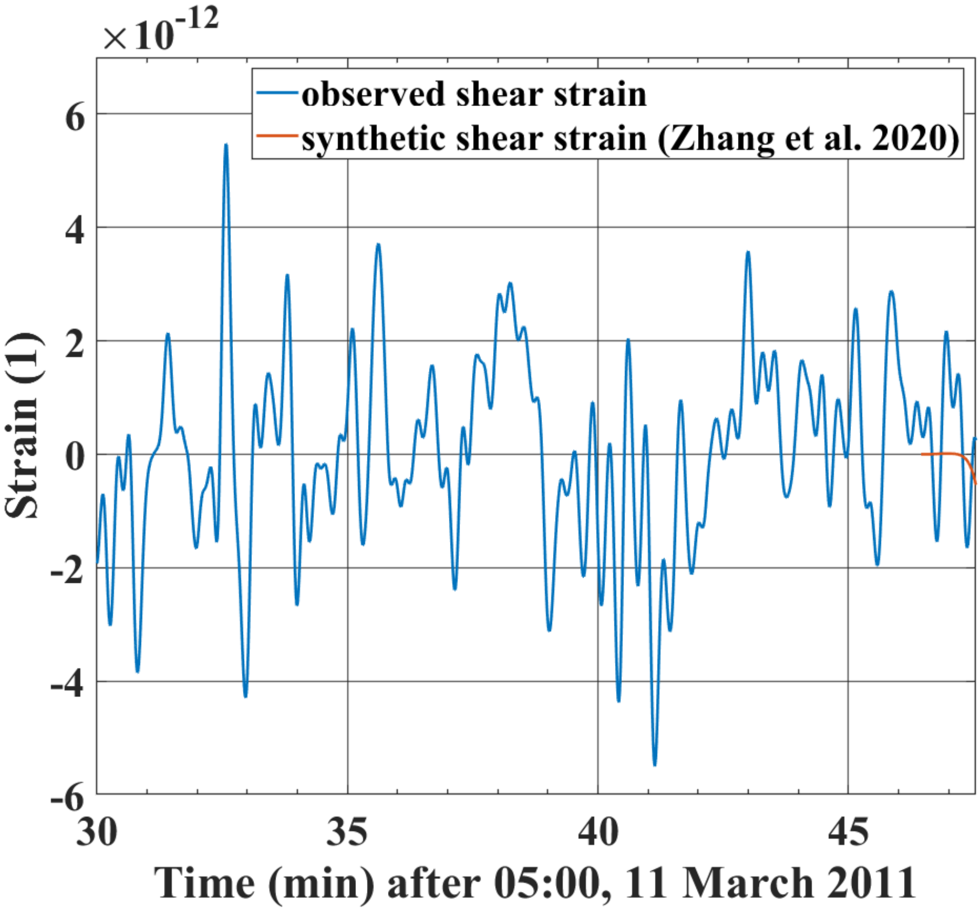
×10^-12
observed shear strain
synthetic shear strain (Zhang et al. 2020)
Strain (1)
6
4
2
0
-2
-4
-6
30
35
40
45
Time (min) after 05:00, 11 March 2011